Dissertation
submitted to the
Combined Faculties for the Natural Sciences and for Mathematics
of the Ruperto–Carola University of Heidelberg, Germany
for the degree of
Doctor of Natural Sciences

Put forward by

Diplom–Physiker	**Malte Christian Frese**
Born in	**Hamburg, Germany**

Oral examination: 20th of July 2011

Potentials and Risks of Advanced Radiobiological Treatment Planning for Proton and Carbon Ion Therapy

Referees: **Prof. Dr. Uwe Oelfke**
Prof. Dr. Wolfgang Schlegel

Zusammenfassung
Chancen und Risiken der fortschrittlichen radiobiologischen Bestrahlungsplanung in der Protonen– und Kohlenstofftherapie

Die technischen Möglichkeiten der Strahlentherapie mit Teilchen sind nach mehr als fünfzig Jahren Erfahrung sehr weit fortgeschritten. Für die Strahlenbiologie gilt dies nur eingeschränkt. Dosisverschreibung und die Berechnung des biologischen Effekts sind immernoch mit großen Fehlern behaftet. Das Ziel dieser Arbeit ist es, die Möglichkeiten aber auch die Grenzen und Risiken der Teilchentherapie besser zu verstehen. Im ersten Teil der Arbeit wurde eine existierende biologische Bestrahlungsplanung für Kohlenstoffionen und Protonen untersucht und erweitert. Dabei verglichen wir die Anwendungen von simultanen und sequentiellen Kohlenstoffboostbestrahlungen, den Einfluss von konstanter und variabler relativer biologischer Wirksamkeit in der Protonentherapie und die Robustheit von "Worst Case" optimierten und konventionellen Bestrahlungsplänen. Der zweite Teil der Arbeit widmet sich der der Verbesserung radiobiologischer Modelle. Hierzu entwickelten wir ein analytisches Modell, um den linearen Energietransfer von Kohlenstofffragmenten zu berechnen, stellten eine Methode vor, die den Einfluss von Sauerstoff auf das Zellüberleben in die Bestrahlungsplanung einbindet, und erweiterten das mechanistische "Repair–Misrepair–Fixation" Modell, um den biologischen Effekt von realistischen Protonen- und Kohlenstoffionenstrahlen besser vorhersagen zu können. Abschließend stellen wir fest, dass entscheidende Fortschritte in der Strahlenbiologie weitere langfristige und systematische Studien voraussetzen. Kurzfristig sollte der Schwerpunkt daher auf den Einsatz ausgeklügelter Optimierungsroutinen gelegt werden.

Abstract
Potentials and Risks of Advanced Radiobiological Treatment Planning for Proton and Carbon Ion Therapy

After fifty years of particle therapy the technical capabilities are far advanced. Nevertheless, radiation biology is still poorly understood. Dose prescription and biological effect calculation are subject to large errors. It is the aim of this work to give a better understanding of the benefits but also the limitations and risks of particle therapy. In the first part of this thesis we studied and extended an existing biological treatment planning method for protons and carbon ions. We compared the simultaneous and sequential application of carbon ion boosts, the influence of constant and variable relative biological effectiveness models in proton therapy, and the robustness of worst case and conventionally optimized treatment plans. The second part of this thesis focuses on improving radiobiological models. We developed an analytical model to calculate the linear energy transfer of carbon ion fragments, presented a method to incorporate oxygen effects into treatment planning, and extended the mechanistic repair–misrepair–fixation model to predict the biological effect of real proton and carbon ion treatment plans. In conclusion, we believe that significant advances in radiation biology will require more long term experience from systematic studies where human influence on plan quality is minimized. Prompt improvements could be achieved by drastically extending the use of advanced optimization algorithms.

Contents

Chapter 1

Introduction

In 1979 Chen *et al.* introduced the first computer aided treatment planning system (TPS) for heavy ion therapy. The authors motivate the TPS by stating that (Chen *et al.* 1979)

> "In order to test the value of this new modality, the technical problems of dose delivery must be adequately understood and solved."

At that time patients had already been treated at Berkeley for more than two decades with helium and for nearly five years with heavier ions*. More than thirty years later, in March 2010, a total of nearly 80,000 patients had been treated with a broad variety of particles. Have the technical problems been understood and solved? We can certainly say that most if not all of the technical problems have been understood. Solutions have been developed and are still frequently revised and improved. The correct translation of the Hounsfield units into water equivalent ranges, for example, is a key point of the article by Chen *et al.* (1979). The very same issue is still investigated frequently today (Schaffner and Pedroni 1998, Jäkel 2006, Lühr *et al.* 2011, to name just a few). Which leaves no doubt that the nature of the problem is understood. And where problems cannot be resolved completely, novel optimization strategies have been designed that optimize an ideal situation while at the same time minimize the impact of known uncertainties. If you compare the sophistication of today's treatment facilities and fast inverse TPS with their predecessors at Berkeley it is justified to assume, that the technical problems of dose delivery are well understood. Now we just need to know how much dose we want delivered.

The designers of this first particle therapy TPS already knew that dose by itself is an insufficient measure to quantify whatever happens in the irradiated tissue. Consequently, hardcopies of the treatment plans that their TPS created did not display the dose but the biological effect. What the biological effect is and how it is calculated is not explained in

*For an overview of particle treatment centers see the PTCOG website.

the paper and the sole listed reference was not available to us. But whatever is proposed in the cited abstract, a glance through the last three decades of publications on the radiation biology of particles shows that it was not a satisfying solution. A vast number of approaches has been published in the meantime e.g. the repair–misrepair model (Tobias 1985), the lethal–potentially lethal model (Curtis 1986), the local effect model (Scholz *et al.* 1997), the repair–misrepair–fixation model (Carlson *et al.* 2008), and the microdosimetric kinetic model (Sato *et al.* 2009). Not only the number of different approaches is a strong indication for the complexity of the problem but also the vast amount of revisions that exist for some models. In several recent publications the reader might get the impression that he himself is not the only one who cannot keep up with all the modifications. Though most of the technical aspects of particle therapy may have been mastered in the last fifty years, it is safe to say that we still do not exactly know what we are heading for.

The aim of this thesis is to give some directions to a well founded dose prescription. The first part of this thesis is dedicated to a better understanding of selected aspects of existing radiobiological models and optimization algorithms. At the core of the biological optimization that is used throughout this thesis is an objective function minimizing the biological effect. It has a fourth order dependence on the particle fluence that may compromise its convexity. If or under which circumstances the objective function is convex is studied in section 3.1. When optimizing multiple radiation modalities in the same treatment plan the optimizer has to be initialized with carefully selected starting weights. Two ways to determine these are presented in section 3.2. The following chapter is devoted to an application of existing methods in the clinic. In section 4.1 we compare a constant and a variable proton relative biological effectiveness (RBE) approach for the treatment planning of realistic patient cases to gain insight in the risks and potentials of delivering inhomogeneous proton target doses. The following section (4.2) proposes a novel approach of combining photon and carbon ion irradiation by using a simultaneous instead of a sequential carbon ion boost. Chapter 4 is closed by a section on worst case optimization for the biological effect. Assuming that our current models predict the biological effect sufficiently accurate we can overcome the limits of accurate dose delivery by intelligent optimization algorithms. The optimized biological effect distributions are tested in regard to their invariance towards range calculation errors or misaligned patients and compared to the conventional margin concept. One of the major issues of current radiobiological considerations is the lack of beam quality measures. In chapter 5 we introduce an analytical model to calculate the LET of primary ions and their fragments. Two potential approaches to improve particle radiobiology are presented in chapter 6. In section 6.1 we propose an optimization method that exploits the benefits of carbon ion irradiation for hypoxic tumors. This is followed by

a section on the repair–misrepair–fixation model (RMF). The RMF is a recently developed mechanistic radiobiology model which we extended from monoenergetic to realistic particle beams. Finally, the results of this thesis are summarized in chapter 7 where we also hope to be able to give some additional directions on the way to an improved understanding and use of particle radiation biology.

This thesis covers a broad spectrum of topics with a similar wide range of basic methods. There is still a significant overlap among many sections. The core of these methods is introduced in chapter 2 which provides the reader with the specific physical, radiobiological, and treatment planning methodology required for an understanding of this thesis. Chapter 2 does not give a general introduction into radiotherapy. It is assumed that the reader is familiar with its basic terminology and ideas. Throughout this work we will follow the recommendations of the ICRU for prescribing proton doses (ICRU 2007) employing the terms absorbed dose (unit Gy) for the physical dose and RBE–weighted absorbed dose (RWD, unit Gy (RBE)) for the product of absorbed dose and RBE.

Chapter 2

Radiation Therapy with Protons and Carbon Ions

2.1 Energy loss of charged particles in matter

An ion – be it a proton or a heavier nucleus – that travels through matter continuously looses energy in electromagnetic Coulomb interactions with electrons and in hadronic interactions with target nuclei. The respective cross sections depend strongly on the kinetic energy of the projectile. Therapeutic ions loose most of their energy in electromagnetic interactions and only this share of the total energy loss will be considered in this section. The most common hadronic interaction is the fragmentation of the projectile in which most of its kinetic energy is transferred to the new fragments. The local energy deposition of a fragmentation event is small compared to that of the electromagnetic interactions and can be neglected. The fragments themselves cannot be ignored. They travel much further in matter than the primary ions and deposit dose in regions that no primary ion reaches.
The energy loss is often measured in stopping powers S. It is defined as the change of kinetic energy E with the depth z

$$S(z) = -\frac{\partial E(z)}{\partial z} \tag{2.1}$$

The electromagnetic stopping power of ions can be calculated using the Bethe formula (Bethe 1930, Johns and Cunningham 1983)

$$S(E) = 0.307 \frac{Z_\mathrm{T}}{A_\mathrm{T}} \frac{Z^2}{\beta^2} \left[\frac{1}{2} \ln \frac{2 m_\mathrm{e} c^2 \gamma^2 \beta^2 T_\mathrm{max}}{I^2} - \beta^2 \right] \left[\frac{\mathrm{MeV\ cm^2}}{\mathrm{g}} \right] \tag{2.2}$$

where some smaller corrections have been ignored. The kinetic energy of the projectile (charge Z, mass number A, mass m) is reflected in the velocity

$$\beta = v/c = \sqrt{1 - (1 + E/mc^2)^{-2}} \tag{2.3}$$

and $\gamma = 1/\sqrt{1-\beta^2}$. It can maximally transfer the energy $T_{\max}$ to an electron (mass m_e). The target is characterized by the charge Z_T, mass number A_T and ionization potential I. The continuous slowing–down–approximation (CSDA) defines the range R of an ion as the distance after which it has on average lost all of its energy

$$R\,(E) = \int_0^E \mathrm{d}E' \frac{1}{S\,(E')}. \tag{2.4}$$

An analytical integration of (2.2) is not feasible. Instead a simple power law for the range R_p of protons has been proposed by Wilson (1946)

$$R_\mathrm{p} = k_\mathrm{p} \cdot E^p. \tag{2.5}$$

Bortfeld (1997) obtained the parameters $k_\mathrm{p} = 0.0022\ \mathrm{MeV}^{-p}$ and $p = 1.77$ as a best fit of equation (2.5) to data published in ICRU report 49 (ICRU 1993). This power law can be extended to heavier ions (charge Z, mass number A) using the relation between range and stopping power that is defined by the CDSA range.

$$R_\mathrm{hi} = \frac{A}{Z^2} k_\mathrm{p} \left(\frac{E}{A}\right)^p = k_\mathrm{hi} E^p \tag{2.6}$$

Here, we defined $k_\mathrm{hi} = A^{1-p}/Z^2 \cdot k_\mathrm{p}$ and made use of the functional relationship of stopping power, charge, mass number and kinetic energy

$$S\,(E) \propto \frac{Z^2}{\beta\,(E/A)} \tag{2.7}$$

that can be inferred from equation (2.2). The range of particles of the same energy per nucleon (E/A) differs by a factor equal to the ratio of A to Z^2. A proton ($A = 1$, $Z = 1$) has therefore three times the range of a carbon ion ($A = 12$, $Z = 6$) given that E/A is the same. Most fragments are light remnants of the primary ions (Schardt *et al.* 1996), hence the longer range.

The dose D at point $\boldsymbol{x}$ in a material of density ρ is defined as the energy absorbed per unit

mass

$$D(\boldsymbol{x}) = \frac{1}{\rho} \int_{-\infty}^{R_0} \mathrm{d}z \; S(z) \, \varphi_z(\boldsymbol{x}) \tag{2.8}$$

where the depth spectrum at $\boldsymbol{x}$ is ϕ_z and R_0 is the ion's residual range. The width of the depth spectrum depends on the accelerator's energy spectrum and on the straggling width of the ions. The latter is proportional to $\sim Z^{-0.25} A^{-0.87}$ (Bethe and Ashkin 1953). At any point $\boldsymbol{x}$ the ion beam has an energy spectrum which can be directly translated into a spectrum of ranges or depths. In a depth spectrum the ion's energy is replaced by the depth in which a monoenergetic particle would have the same energy. Equation (2.8) can be used to calculate the depth–dose curve of ions with the well-known Bragg peak at the end of their range. The width of the Bragg peak and the peak–to–entrance ratio are strongly influenced by the straggling width, hence the sharper Bragg peak for carbon ions than for protons. The fluence at point $\boldsymbol{x}$ is given by

$$\Phi(\boldsymbol{x}) = \int_{-\infty}^{R_0} \mathrm{d}z \; \varphi_z(\boldsymbol{x}) \,. \tag{2.9}$$

The lateral penumbra of an ion beam depends largely on multiple Coulomb scattering (Gottschalk *et al.* 1993). The width of the Gaussian distribution of scattering angles is proportional to $Z/\beta pc$ (Highland 1975). Hence, proton dose falls off with a similar slope as therapeutic photon beams while carbon ions are so heavy that lateral scattering can be ignored (Krämer *et al.* 2000).

Stopping power has so far only be defined for monoenergetic particles. In reality, many particles with different stopping powers interfere at a point $\boldsymbol{x}$ irradiated with one or many ion beams. If the average stopping power is calculated as a fluence–weighted average it is referred to as track–averaged linear energy transfer $\mathrm{LET_t}$

$$LET_\mathrm{t}(\boldsymbol{x}) = \frac{\int_{-\infty}^{R_0} \mathrm{d}z \; S(z) \, \phi_z(\boldsymbol{x})}{\int_{-\infty}^{R_0} \mathrm{d}z \; \phi_z(\boldsymbol{x})} \tag{2.10}$$

In a radiobiological context it is often necessary to weigh the stopping power with the dose instead.

$$LET_\mathrm{d}(\boldsymbol{x}) = \frac{\int_{-\infty}^{R_0} \mathrm{d}z \; S^2(z) \, \phi_z(\boldsymbol{x})}{\int_{-\infty}^{R_0} \mathrm{d}z \; S(z) \, \phi_z(\boldsymbol{x})} \tag{2.11}$$

The resulting average stopping power is called dose–averaged linear energy transfer $\mathrm{LET_d}$.

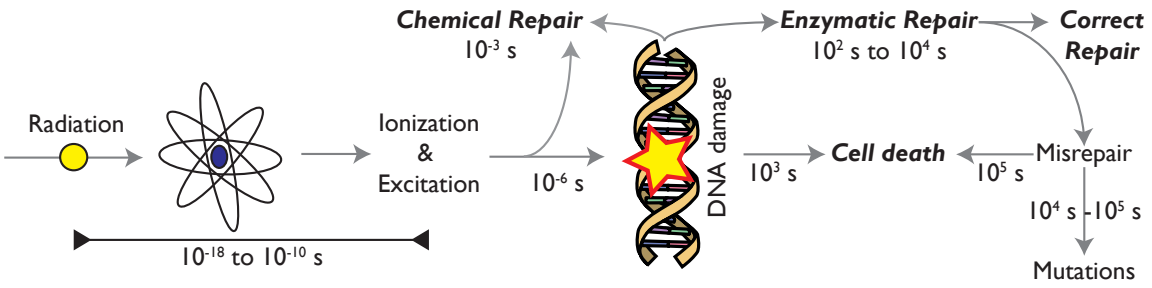

Figure 2.1: *From the physical interaction of radiation with a target atom to biological manifestation of the damage. Adapted from a figure courtesy of Robert D. Stewart. The symbolic DNA double strand was extracted from Wikimedia.*

2.2 Radiobiology of charged particles

Secondary electrons, also called δ–rays, created in Coulomb interactions of primary ions with target atoms are the primary source of radiobiological damage. Figure 2.1 outlines how the physical interaction of radiation with a target atom is translated into biological damage. The primary radiation itself but mostly secondary electrons can excite or ionize atoms in the DNA. In consequence, chemical bonds break up and bases are damaged or strands break. Some of the broken bonds will be chemically repaired or fixed by oxygen radicals. A fixed breakage is lethal as it cannot be repaired by cellular mechanisms anymore. This illustrates the important role of cellular oxygen pressure in radiation therapy. The remainder of damages will undergo enzymatic repair. Those cells that were not or cannot be successfully repaired (misrepaired cells) either die or form mutated cells. In healthy tissue both dead and mutated cells may lead to clinical responses like inflammation or cancer. This is of course only simplified picture of radiation biology but it contains the foundations of the radiobiological considerations presented in this work. For the design of radiobiological models three observations are especially important:

(i) The initial DNA damage is a function of the radiation quality not the cell type.

(ii) Oxygen effects are independent of the cell type.

(iii) Enzymatic repair processes are cell but not radiation specific.

In the light of these observations it is questionable if the term relative biological effectiveness is appropriate. The difference between radiations is the physical damage, not in the biology that reacts on the damage. It is the physical effectiveness that matters.
In this section four radiobiological models are presented out of which the linear–quadratic (LQ) model (Kellerer and Rossi 1978) is probably the most prominent. In the LQ–model cell survival is a function of two parameters and the dose. The other three models are all used to calculate these parameters. We will present a linear scaling model (LSM) for protons (Wilkens and Oelfke 2004), the local effect model (LEM) developed for particle therapy (Scholz *et al.* 1997), and the repair–misrepair–fixation model (RMF) for photons, electrons, and ions (Carlson *et al.* 2008). Each of these models incorporates the separation of physics and biology to a different degree.

2.2.1 The linear–quadratic model

The LQ–model relates the absorbed dose D to the biological effect $\mathcal{E}$ through two cell and radiation quality specific parameters α and β using

$$\mathcal{E}(D) = \alpha D + G\beta D^2 \tag{2.12}$$

where G is the time dependent Lea–Catcheside dose protraction factor (Sachs *et al.* 1997). We will assume that the single radiation dose is delivered in such a short time that $G = 1$. For each combination of radiation quality and tissue an individual set of parameters has to be determined. The LQ–model itself does not provide any means to readjust parameters from one situation to another. Hence, they have to be determined experimentally or from distinctive models such as those presented in the following sections. We have purposely used the undefined term radiation quality. Which properties of the radiation α and β relate to eventually depends on the respective model.
The synergistic effects of multiple radiations can be determined through dose–averaged parameters α_D and $\sqrt{\beta_\mathrm{D}}$ (Zaider and Rossi 1980). For N contributing radiations the average parameters are given by (Wilkens and Oelfke 2006)

$$\alpha = \frac{1}{D}\sum_{i=1}^{N}\alpha_i D_i \qquad \text{and} \qquad \sqrt{\beta} = \frac{1}{D}\sum_{i=1}^{N}\sqrt{\beta_i} D_i \tag{2.13}$$

where D is the sum of the doses D_i deposited by the respective radiation i. For continuous distributions the sum in equation (2.13) can be transformed to an integral. RBE is defined as the ratio of a reference radiation dose D_x to a test radiation dose D that produce the

same biological effect. In the framework of the LQ–model the RBE can be expressed as a function of the respective parameters and D

$$RBE_{\mathrm{LQ}}\left(\alpha_{\mathrm{x}}, \beta_{\mathrm{x}}, \alpha, \beta, D\right) = \frac{\sqrt{\alpha_{\mathrm{x}}^2 + 4\beta_{\mathrm{x}} D\left(\alpha + \beta D\right)} - \alpha_{\mathrm{x}}}{2\beta_{\mathrm{x}} D}. \tag{2.14}$$

In the limit of very small and very large doses the RBE is proportional to $\alpha/\alpha_{\mathrm{x}}$ and $\sqrt{\beta/\beta_{\mathrm{x}}}$, respectively.

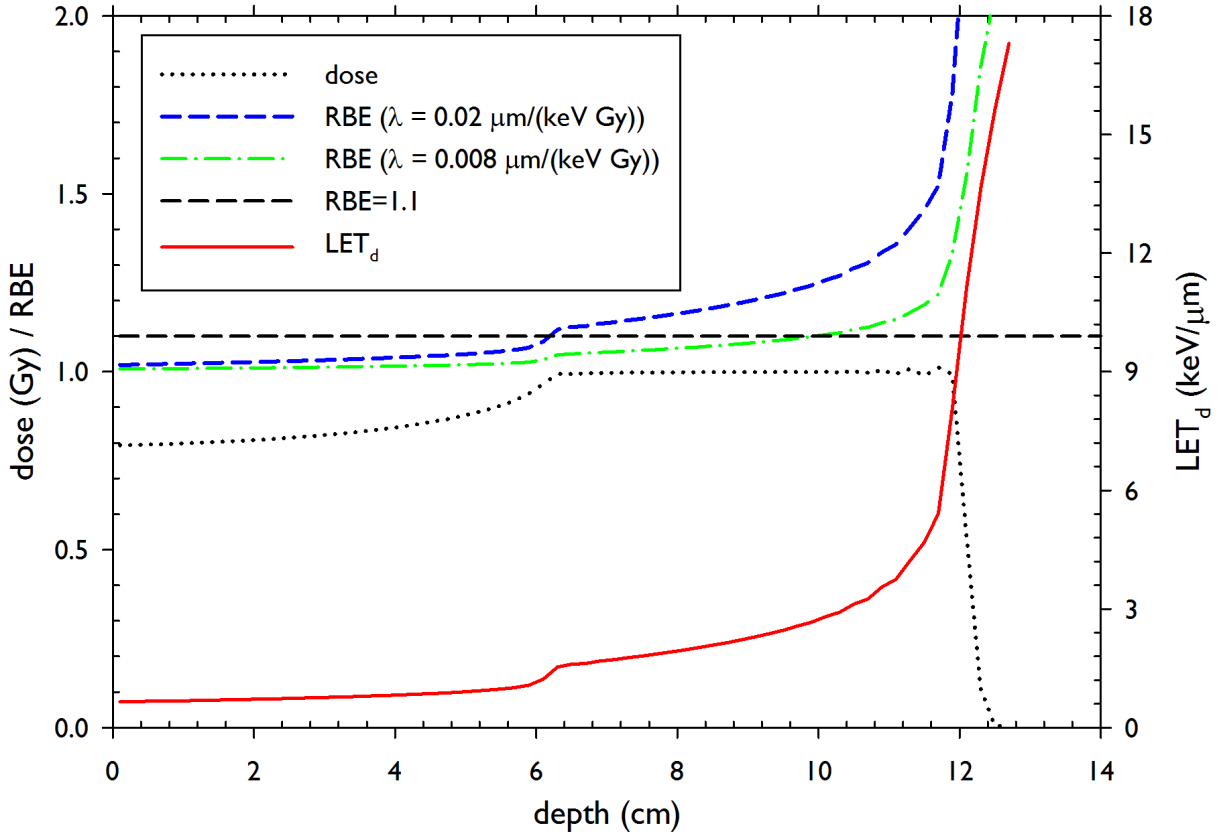

Figure 2.2: *The influence of the parameter λ of the LSM on the proton RBE. A value obtained from in vitro experiments with V79 cells ($\lambda = 0.02\ \mu\mathrm{m}/(\mathrm{keV}\cdot\mathrm{Gy})$) is compared with a second value ($\lambda_{1.1} = 0.008\ \mu\mathrm{m}/(\mathrm{keV}\cdot\mathrm{Gy})$) reflecting the clinical experienced average proton RBE of 1.1. The clinically employed proton RBE of 1.1 is also shown. Reference photon parameters are $\alpha_{\mathrm{x}} = 0.112\ \mathrm{Gy}^{-1}$ and $\beta_{\mathrm{x}} = 0.0298\ \mathrm{Gy}^{-2}$.*

2.2.2 The linear scaling model for protons

Wilkens and Oelfke (2004) introduced a phenomenological model to determine LQ–model parameters for protons. They assumed a linear dependence of α_{p} on the LET

$$\alpha_{\mathrm{p}} = \alpha_0 + \lambda \cdot LET_{\mathrm{d}} \tag{2.15}$$

and kept the second parameter β_{p} constant and equal to the reference parameter β_{x}. From equation (2.13) follows that for non–monoenergetic particles the dose–averaged LET has to be used. The parameter α_0 was originally set equal to the reference radiation parameter α_{x}. In a recent publication (Frese *et al.* 2011a) we introduced a refined definition to accommodate clinical experience that the RBE of a proton beam is approximately unity in the entrance region (Paganetti *et al.* 2002). Now α_0 is calibrated to reflect this observation for an entrance LET of ~ 0.5 keV/μm:

$$\alpha_0 = \alpha_{\mathrm{x}} - \lambda \cdot 0.5 \text{ keV}/\mu\text{m} \tag{2.16}$$

The entrance LET was averaged from three initial beam energies (160 MeV, 200 MeV, 250 MeV) that are frequently used in therapeutic setting (compare table 2.1). If the RBE is expressed in terms of the LSM model we yield

$$RBE_{\mathrm{LSM}}\left(\alpha_{\mathrm{x}}, \beta_{\mathrm{x}}, \lambda, D, LET\right) = -\frac{1}{2D}\frac{\alpha_{\mathrm{x}}}{\beta_{\mathrm{x}}} + \left[\frac{1}{4D^2}\left(\frac{\alpha_{\mathrm{x}}}{\beta_{\mathrm{x}}}\right)^2 + \frac{1 + \frac{\lambda}{\alpha_{\mathrm{x}}}\left(LET - 0.5 \text{ keV}/\mu\text{m}\right)}{D}\frac{\alpha_{\mathrm{x}}}{\beta_{\mathrm{x}}} + 1\right]^{1/2}. \tag{2.17}$$

The linear parameter λ can be obtained in two different ways. Wilkens and Oelfke (2004) estimated λ by fitting equation (2.15) to α values previously published by other authors. For V79 cells they yielded $\lambda = 0.02$ μm keV^{-1} Gy^{-1} with low LET reference parameters $\alpha_{\mathrm{x}} = 0.112$ Gy^{-1} and $\beta_{\mathrm{x}} = 0.0298$ Gy^{-2} . These α values emanate from *in vitro* experiments and predict a mean RBE significantly greater than 1.1 which is observed *in vivo* (Paganetti *et al.* 2002). The mean and maximum RBE across a 1 Gy spread–out Bragg peak (SOBP, cf. figure 2.2) calculated with the *in vitro* λ are ~ 1.24 and 1.74, respectively.
For clinical applications we therefore developed a method to ensure that the mean RBE in the target is 1.1 (Frese *et al.* 2011a). A first treatment plan is optimized with a constant RBE of 1.1. The mean LET$_{\mathrm{d}}$ $\overline{L}$ and dose $\overline{D}$ of the target volume are extracted and λ is

adjusted using

$$\lambda_{1.1} = \frac{\alpha_\mathrm{x}\,(RBE - 1) + \beta_\mathrm{x}\overline{D}\,(RBE^2 - 1)}{\overline{L} - 0.5\ \mathrm{keV}/\mu\mathrm{m}} \tag{2.18}$$

where $RBE = 1.1$. Equation (2.18) was obtained by solving equation (2.17) for λ. An example of an RBE obtained with this method is also visualized in figure 2.2. Across the SOBP $\overline{D} = 0.999$ Gy and $\overline{LET} = 2.71$ keV/μm which yields $\lambda_{1.1} = 0.0080\ \mu\mathrm{m\,keV^{-1}\,Gy^{-1}}$. The mean and maximum RBE are 1.1 and 1.33, respectively.

2.2.3 The local effect model

The local effect model (LEM) is a track–structure model developed at Gesellschaft für Schwerionenforschung (GSI, Darmstadt, Germany) to determine RBE–weighted doses for their heavy ion therapy project (Scholz *et al.* 1997, Krämer and Scholz 2000). Since its first presentation it has been repeatedly modified for various reasons (Krämer and Scholz 2006, Elsässer and Scholz 2007, Elsässer *et al.* 2010) but to the author's knowledge none of these modifications has found its application for clinical treatment planning. At the Heidelberg Ion–Beam Therapy Center (HIT, Heidelberg, Germany) the successor of the prototype treatment facility at GSI the first LEM version is still in use. The biological input for carbon ions in our in–house treatment planning system *KonRad* is also based on this implementation (Wilkens and Oelfke 2006, Frese 2007). We will therefore limit ourselves to a brief presentation of this version.
Like the first amorphous track–structure model developed by Butts and Katz (1967) the LEM is based on the assumption that for equal doses the biological effect of δ-electrons of ion tracks and of γ–rays is the same. The LEM uses a parameterized dose–response curve derived from experimental photon data.

$$\mathcal{E} = \begin{cases} \alpha_\mathrm{x} D + \beta_\mathrm{x} D^2 & \text{for } D \le D_\mathrm{t} \\ \alpha_\mathrm{x} D + \beta_\mathrm{x} D_\mathrm{t}\,(2D - D_\mathrm{t}) & \text{for } D > D_\mathrm{t} \end{cases} \tag{2.19}$$

The parameter D_t marks the transition from a quadratic to a linear dose dependence of the biological effect. The dose around a particle track is assumed to be radially distributed with a constant dose inside a radius of 10 nm. It is locally scored in a disc shaped target structure of similar size as a cell nucleus for which the deactivation probability is determined. This leaves the model with four input parameters: the disc size, the transition dose, and the two reference LQ parameters. Paganetti and Goitein (2001) found a strong

dependence of the predicted dose–response on D_{t}, which cannot be obtained properly from photon measurements as it is in the order of 15 to 30 Gy for many cell lines. Irradiating a cell dish with such doses will hardly leave any cell alive.

2.2.4 The repair–misrepair–fixation model

The repair–misrepair–fixation (RMF) model developed by Carlson *et al.* (2008) is the only mechanistic radiobiological model discussed here. It describes the conversion of intrinsic double strand breaks (DSB) into lethal cell damage by a non–linear differential equation. It extends the previously published repair–misrepair (RMR) model (Tobias 1985) and the lethal–potentially lethal (LPL) model (Curtis 1986) by adding further pathways of DSB processing. The LQ–model is a time–integrated approximate solution to the RMF differential equation. Here, we will give an introduction in the basic assumptions of the RMF model and how it relates to the LQ–model.
The most important physical input parameter for the RMF model is the initial DSB yield. From experiments it is known that the induction of DSB increases linearly with the dose up to several 100 Gy (Rothkamm and Löbrich 2003) and their relative number is similar among all eukaryotes (Carlson 2006, and references therein). This makes the DSB yield an ideal measure of radiation damage as it depends only on the radiation quality and not on the irradiated cell. The DSB yield can be determined from experiments or track–structure simulations. For all calculations performed in this work we used output from the Monte Carlo damage simulations (MCDS) tool (Semenenko and Stewart 2004, 2006), a fast Monte Carlo algorithm that reproduces the results of detailed track–structure simulations and DNA damage measurements.
The following description of the RMF closely follows the original description of the RMF by Carlson (2006). In figure 2.3 five pathways are shown that potentially convert initial DSB into lethal cell damage. Each of these pathways is reflected in the differential equation of the RMF that describes the rate of change of lethal DNA damages per cell $\mathrm{d}F/\mathrm{d}t$ at time t by

$$\frac{\mathrm{d}F}{\mathrm{d}t} = (1 - f_{\mathrm{R}})\,\Sigma\dot{D}\,(t) + [(1-a)\,\varphi\lambda_{\mathrm{R}} + \lambda_{\mathrm{F}} + \gamma\eta\varepsilon]\,L\,(t) + \gamma\eta L^2\,(t) \tag{2.20}$$

The dose rate $\dot{D}\,(t)$ and the average number of DSB per cell $L\,(t)$ are time dependent functions. The first term $(1 - f_{\mathrm{R}})\,\Sigma\dot{D}\,(t)$ describes the number of intrinsically unrejoinable DSB where f_{R} is the ratio of potentially rejoinable DSB and Σ is the initial number of DSB per Gy and cell or giga base pair (Gbp). The probability λ_{R} that a single DSB

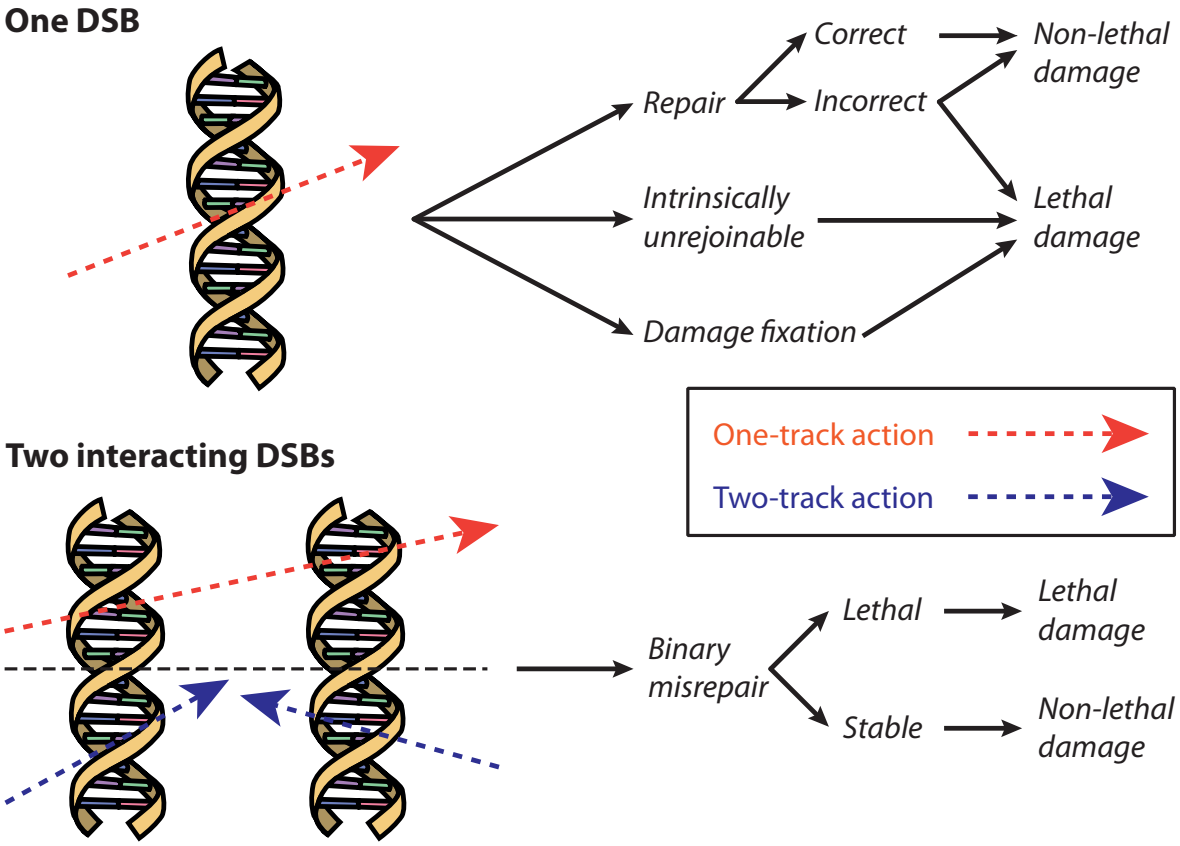

Figure 2.3: *Cellular processing of double strand breaks (DSB) created by one (red arrows) or two (blue arrows) particle tracks. Figure adapted from Carlson (2006), symbolic DNA double helix extracted from Wikimedia.*

undergoes first–order repair that fails (misrepair) is given by $(1-a)\,\varphi\lambda_{\mathrm{R}}L\,(t)$. Out of the misrepaired DSB which occur with the probability $(1-a)$ only φ are lethal. The third lethal pathway $\lambda_{\mathrm{F}}L\,(t)$ is extrinsic damage fixation which occurs with the rate λ_{F}. This leaves those pathways that are created by two interacting DSB. The probability of lethal binary misrepair of two DSB created by the same track is given by $\gamma\eta\varepsilon L\,(t)$ (intra–track misrepair). In each track $\varepsilon = \bar{z}_{\mathrm{f}} f_{\mathrm{R}}\Sigma$ potentially rejoinable DSB are formed out of which η undergo binary misrepair. The probability that the binary misrepair is not stable is given by γ and the frequency–mean specific energy $\bar{z}_{\mathrm{f}}$ (in Gy) for a spherical water target of diameter d is estimated by (ICRU 1983)

$$\bar{z}_{\mathrm{f}} = 0.204\frac{S}{d^2} \tag{2.21}$$

where S is the stopping power in keV/μm. The last term $\gamma\eta L^2(t)$ of equation (2.20) defines the probability that two DSB created by different tracks are binary misrepaired (inter–track misrepair).
Carlson (2006) shows in detail how in the limit of small doses and dose rates the LQ–model can be derived from the RMF differential equation using perturbation theory. In terms of the RMF model the LQ parameters are given by

$$\alpha = \left[1 - f_{\mathrm{R}}(1-\theta)\right]\Sigma + \kappa\bar{z}_{\mathrm{f}}\left(f_{\mathrm{R}}\Sigma\right)^2 \tag{2.22}$$

$$\beta = \frac{\kappa}{2}\left(f_{\mathrm{R}}\Sigma\right)^2 \tag{2.23}$$

where

$$\theta = \frac{(1-a)\,\phi\lambda_{\mathrm{R}} + \lambda_{\mathrm{F}}}{\lambda_{\mathrm{R}} + \lambda_{\mathrm{F}}} \qquad \text{and} \qquad \kappa = \frac{\eta}{\lambda_{\mathrm{R}} + \lambda_{\mathrm{F}}}(\gamma - \theta) \tag{2.24}$$

are the fraction of initial DSB that undergo either lethal first order misrepair and damage fixation (θ) or pairwise damage interaction (κ). Hence, in the RMF model α and β can be interpreted as the respective contribution of one–track and two–track events to the biological effect. For the sake of completeness we would like to note that the Lea–Catcheside dose protraction factor G can also be derived from the RMF model and is given by

$$G(\lambda, T) = \frac{2}{(\lambda T)^2}\left(\mathrm{e}^{-\lambda T} + \lambda T - 1\right) \tag{2.25}$$

where $\lambda = \lambda_{\mathrm{R}} + \lambda_{\mathrm{F}}$. Testing of the prediction capabilities showed that it best matches measured data if it is assumed that all DSB are potentially repairable i.e. $f_{\mathrm{R}} = 1$ (Carlson *et al.* 2008). This reduces equations (2.22) and (2.23) to

$$\alpha = \theta\Sigma + \kappa\bar{z}_{\mathrm{f}}\Sigma^2 \text{ and} \tag{2.26}$$

$$\beta = \frac{\kappa}{2}\Sigma^2. \tag{2.27}$$

The latter assumption has also been applied to predict α and β in figure 2.4. For V79 cells irradiated by three ion species (He–3, C–12 and N–20) parameters were calculated for a wide range of LET values. For comparison data points measured by Furusawa *et al.* (2000) are shown. It appears that the RMF can predict LQ parameters up to an LET of 100 keV/μm to 150 keV/μm. The downward trends observed for higher LET is not reproduced. As we did not know the energy spectrum of the experimental particle beams we assumed that they are monoenergetic. For monoenergetic particles dose– and track–

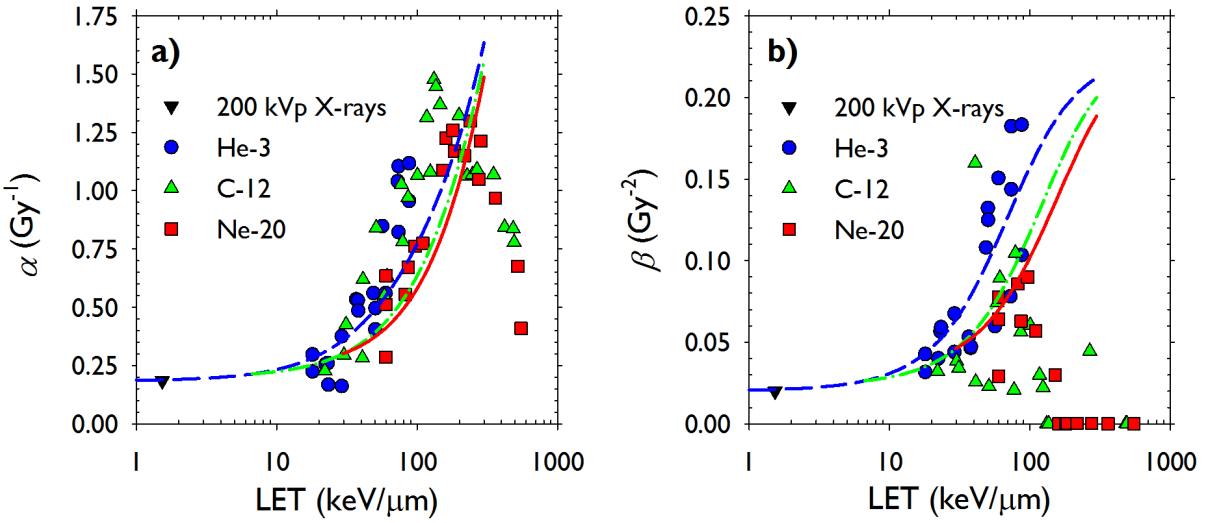

Figure 2.4: *Prediction of LQ parameters for three different ions and a wide range of LET values by the RMF model based on a single low LET reference point. The data points shown were extracted from Furusawa et al. (2000).*

averaged LET are equal.

So far the derivation of the RMF and the LQ–model as its time integrated solution have been presented. For a recently submitted manuscript (Frese *et al.* 2011b) several equations were derived to predict the biological effect for different radiation modalities. Given a set of LQ parameters α_x, β_x for a low LET reference radiation equations (2.26) and (2.27) can be rearranged to yield θ and κ

$$\theta = \frac{\alpha_x - 2\beta_x \bar{z}_{f,x}}{\Sigma_x}, \tag{2.28}$$

$$\kappa = \frac{2\beta_x}{\Sigma_x^2} \tag{2.29}$$

where Σ_x and $\bar{z}_{f,x}$ are the DSB yield and frequency–mean specific energy of the reference radiation, respectively. The latter equations can in turn be inserted into equations (2.26) and (2.27) to express α and β for a test radiation in terms of the reference radiation parameters and radiation quality

$$\alpha = \frac{\Sigma}{\Sigma_x}\left[\alpha_x + 2\frac{\beta_x}{\Sigma_x}\left(\Sigma\bar{z}_f - \Sigma_x \bar{z}_{f,x}\right)\right], \tag{2.30}$$

$$\beta = \left(\frac{\Sigma}{\Sigma_x}\right)^2 \beta_x. \tag{2.31}$$

The last equation illustrates how α and β scale with the DSB yield. In a last step we would now like to calculate the RBE in the RMF model.

$$RBE_{\mathrm{RMF}}\left((\alpha/\beta)_{\mathrm{x}}, \bar{z}_{\mathrm{f,x}}, \Sigma_{\mathrm{x}}, \bar{z}_{\mathrm{f}}, \Sigma, D\right) = \frac{1}{2D} \cdot \left[\sqrt{\left[\left(\frac{\alpha}{\beta}\right)_{\mathrm{X}} + 2D\frac{\Sigma}{\Sigma_{\mathrm{x}}}\right]^2 + \frac{8D}{\Sigma_{\mathrm{x}}^2}\left(\bar{z}_{\mathrm{f}}\Sigma^2 - \bar{z}_{\mathrm{f,x}}\Sigma_{\mathrm{x}}\Sigma\right)} - \left(\frac{\alpha}{\beta}\right)_{\mathrm{x}}\right] \quad (2.32)$$

When predicting RBE with the RMF the only tissue specific parameter is the ratio of α_{x} and β_{x}. The individual parameter values are not reflected. All other parameters are to the most degree physical parameters and independent of the cell type. In appendix A it is demonstrated that equation (2.32) fulfills the low and high dose limits.

2.3 Treatment planning for charged particles

The treatment planning system *KonRad* (Nill *et al.* 2004, Nill 2002) is the basic tool for all treatment planning performed in this work. From its first days *KonRad* was designed as a multi–modality treatment planning system using the same framework to optimize treatment plans for photons, protons, electrons, carbon ions and even mixed radiation modalities. At the core of *KonRad* is a dose influence matrix usually referred to as D_{ij} matrix. It contains the dose D_{ij} that doseburst j deposits in voxel i for a unity fluence. A doseburst is the smallest element of a field whose fluence can be independently varied i.e. the smallest opening of an MLC for photons or a single Bragg peak for particles. The dose D_i in voxel i irradiated by N_{DB} dosebursts is then given by

$$D_i = \sum_{j=1}^{N_{\mathrm{DB}}} D_{ij} w_j \quad (2.33)$$

where w_j is the weight of doseburst j. The D_{ij} matrix allows the separation of dose calculation and optimization which makes *KonRad* very flexible and allows the use of multiple dose engines and optimization algorithms. Originally *KonRad* optimized only the physical dose. It was later extended to optimize the biological effect for protons (Wilkens and Oelfke 2004) and carbon ions (Wilkens and Oelfke 2006).
We will give here a brief introduction into the basic concepts of *KonRad*. First, we will present the dose delivery techniques used in this work followed by a section explaining how dose and biological parameters are calculated and stored. Finally, the (biological) optimization concept in *KonRad* will be outlined.

2.3.1 Dose delivery techniques

In analogy to intensity modulated radiotherapy (IMRT) for photons (Bortfeld 2006) particle therapy plans with homogeneous dose or RWD distributions can be delivered with multiple inhomogeneous fields. While the intensity of IMRT fields can only be modulated laterally to the incident beam direction the finite range of particles allows to modulate the intensity in three dimensions. This led to the definition of four different modulation techniques of different complexity (Lomax 1999). Out of the proposed methods 3D IMPT (figure 2.5) is the only method that exploits the full potential of charged particles. A full coverage of the targets with Bragg peaks whose intensity can be individually modulated (Brahme *et al.* 1989) allows very accurate dose shaping and the highest potential for treatment planning. It is 3D IMPT that is employed in modern particle therapy centers with magnetic beam scanning systems (Lomax *et al.* 1996, Schulz-Ertner *et al.* 2004, Combs *et al.* 2010) and it will also be employed throughout this thesis for all treatment plans. The reader should bear in mind that the high degree of freedom in 3D IMPT comes at the cost of very inhomogeneous treatment fields. A small shift of the patient or of the relative position of two or more fields may lead to large changes in the dose distribution.

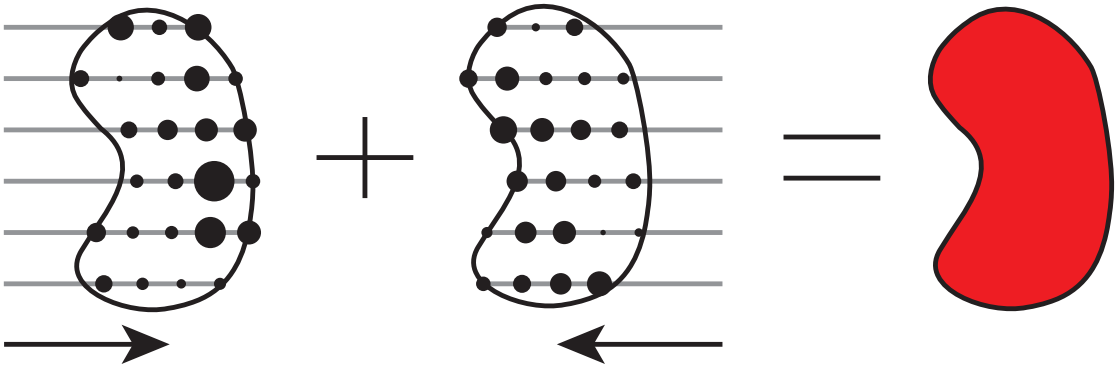

Figure 2.5: *3D IMPT: A target volume is covered with many Bragg peaks (black dots). The intensity of each Bragg peak (represented by its diameter) is varied individually such that the combination of multiple inhomogeneous fields (here two) results in a constant target dose. The gray lines show which spots belong to the same ray i.e. are in the same lateral position to the central field axis.*

Protons as well as carbon ions were used for different parts of this thesis. For each particle type a virtual therapy accelerator was defined. Our virtual proton accelerator has three initial beam energies. The energies and additional beam properties are listed in table 2.1. Depth dose distributions for every energy were calculated using an analytical model (Bortfeld 1997). The initial energy spectrum of the beams is assumed to follow a Gaussian

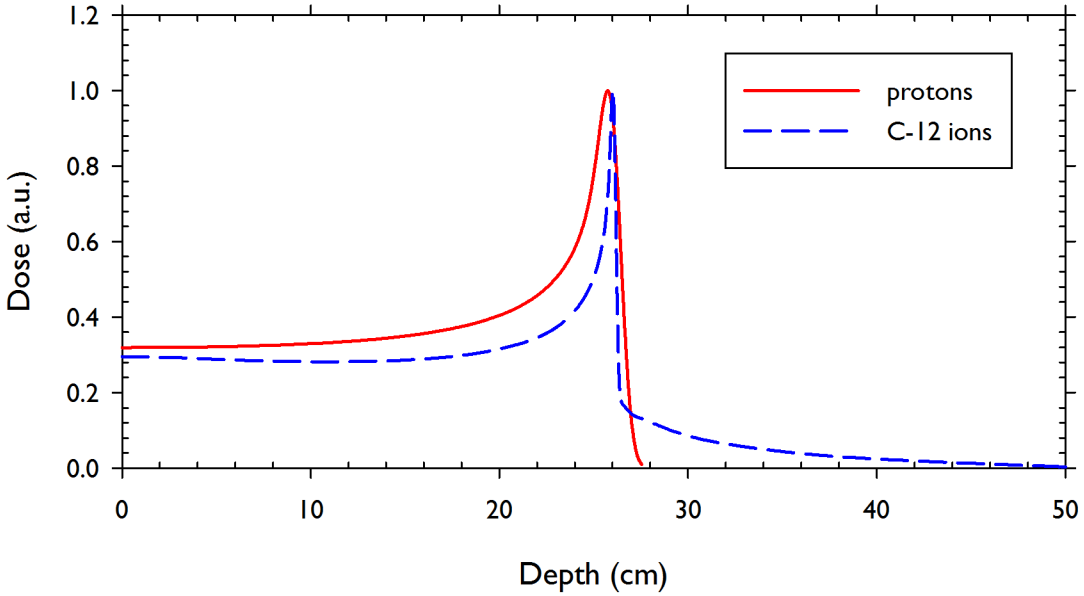

Figure 2.6: *Depth–dose curve of a proton (solid red) and a carbon ion beam (dashed blue) of similar residual range (*26.0 cm*) normalized to the maximum dose. Initial kinetic energies are* 200 MeV *and* 372 MeV/u *for the proton and carbon ion beam, respectively.*

distribution with a width of 0.5 % of the initial energy and the source to isocenter distance is 10 m. Intermediate and generally lower energies can be created using a virtual continuous range shifter whose thickness *KonRad* determines internally such that spots can be place in equidistant positions. The virtual carbon ion accelerator is designed to reproduce the accelerator used at GSI and can choose from 252 initial energies covering an energy spectrum from 88.83 MeV/u to 430.10 MeV/u. This corresponds to water equivalent residual ranges of 2.1 cm to 33.6 cm with an approximate spacing of 1 mm in depth. The longitudinal width of the Bragg peak is widened by a 3 mm ripple filter (Weber and Kraft 1999). The lateral spot size is not fixed but can be varied continuously with the magnetic beam scanning system at GSI (Haberer *et al.* 1993). According to their protocol the full width at half maximum of the initial beam is selected to be three times the lateral spot distance (Krämer *et al.* 2000). An example for a proton and carbon ion depth dose curve as they are used as input for *KonRad* is shown in figure figure 2.6. Carbon ions have a higher peak–to–entrance dose ratio and the dose falls off steeper after the Bragg peak but there is also dose far behind it. This fragmentation tail with more than 10 % of the peak dose is not observed for protons.

Table 2.1: *The three initial beam Energies E_{init}, the respective residual range R_0 in water, the beam width at the entrance of the beam in tissue (σ_{init}) and at the peak (σ_{peak}), and the total stopping power in water (S_{init}) when entering water. Stopping powers were extracted from ICRU (1993) .*

E_{init}	R_0	σ_{init}	σ_{peak}	S_{init}
160 MeV	17.5 cm	2.5 mm	4.4 mm	0.52 keV/μm
200 MeV	26.0 cm	2.5 mm	5.8 mm	0.45 keV/μm
250 MeV	33.3 cm	2.5 mm	8.0 mm	0.39 keV/μm

2.3.2 Calculating the dose and the biological effect

Once the spots have been set the D_{ij} matrix has to be filled i.e. the dose has to be calculated. For protons and carbon ions *KonRad* uses a build in pencil beam algorithm (Nill *et al.* 2004). The lateral width of the proton beam is calculated using multiple Coulomb scattering theory. Carbon ions are so heavy that we assume that the beam does not widen (cf. section 2.1).

In order to calculate RBE–weighted doses the biological models in *KonRad* also need input data. Currently two different models are implemented: one for protons and one for carbon ions. Depending on the employed biological model additional influence matrices have to be filled. The biological model for protons is based on the LSM (section 2.2.2) and requires α_{x}, α_0, β_{x} and LET_{d} as input. The latter is a dose and depth dependent value and is therefore stored in an additional L_{ij} matrix. The LET is calculated with an analytical model (Wilkens and Oelfke 2003) and assumed to be laterally constant for each pencil beam (Wilkens and Oelfke 2004). For carbon ions no biological model is implemented but a flexible biological optimization that requires LQ parameters for a reference radiation and tabulated α depth curves (Wilkens and Oelfke 2006). The latter have been extracted from the GSI treatment planning TRiP (Krämer and Scholz 2000) and are therefore based on the LEM (section 2.2.3). β is assumed to be constant and equal to the reference parameter. Hence, this model requires an α_{ij} matrix. For details on the extraction of α and interpolation of missing values see Frese (2007).

2.3.3 Optimization of the biological effect

Conventional radiotherapy with photons aims to deliver a homogeneous absorbed dose across the tumor which, due to the constant radiation quality of photons, is equal to a homogeneous biological effect. Hence, for particles with variable radiation quality like

protons and carbon ions not the dose has to be optimized but the RWD or directly the biological effect. The latter approach was implemented in *KonRad* by Wilkens and Oelfke (2004, 2006).

The optimization in *KonRad* minimizes an objective function F that is defined as the weighted sum of objective functions for each volume

$$F(\boldsymbol{w}) = \sum_{v \in Targets} \left(p_v^{\mathrm{U}} F_v^{\mathrm{U}}(\boldsymbol{w}) + p_v^{\mathrm{O}} F_v^{\mathrm{O}}(\boldsymbol{w}) \right) + \sum_{v \in OAR} p_v^{\mathrm{O}} F_v^{\mathrm{O}}(\boldsymbol{w}) \tag{2.34}$$

Here, $\boldsymbol{w}$ is the vector of weights defining the fluence of each of the dosebursts. The quadratic objective functions for each target and each organ at risk (OAR) are weighted with individual penalty factors p_v that can be defined independently for underdosage (superscript U) and overdosage (superscript O). For photons or protons with a generic RBE of 1.1 the physical objective functions for volume v are given by (Oelfke and Bortfeld 2001)

$$F_v^{\mathrm{O}}(\boldsymbol{w}) = \sum_{i \in v} \left| D_i(w) - \bar{D}_v^{\mathrm{O}} \right|_+^2 \tag{2.35}$$

$$F_v^{\mathrm{U}}(\boldsymbol{w}) = \sum_{i \in v} \left| \bar{D}_v^{\mathrm{U}} - D_i(w) \right|_+^2 \tag{2.36}$$

where $\bar{D}_v$ is the respective prescribed absorbed dose for volume v. The dose $D_i(\boldsymbol{w})$ is calculated according to equation (2.33) and the $|x|_+$ operator is defined as

$$|x|_+ \equiv \begin{cases} 0 & \text{for } x \leq 0 \\ x & \text{for } x > 0. \end{cases} \tag{2.37}$$

Objective functions for the biological effect follow the same scheme. The quadratic difference between prescribed effect $\bar{\mathcal{E}}_v$ and actual effect $\mathcal{E}_i(\boldsymbol{w})$ is minimized using

$$F_v^{\mathrm{O}}(\boldsymbol{w}) = \sum_{i \in v} \left| \mathcal{E}_i(\boldsymbol{w}) - \bar{\mathcal{E}}_v^{\mathrm{O}} \right|_+^2 \tag{2.38}$$

$$F_v^{\mathrm{U}}(\boldsymbol{w}) = \sum_{i \in v} \left| \bar{\mathcal{E}}_v^{\mathrm{U}} - \mathcal{E}_i(\boldsymbol{w}) \right|_+^2 \tag{2.39}$$

Each doseburst j that deposits a dose $D_{ij} w_j$ in voxel i has a different radiation quality and therefore its specific LQ parameters α_{ij} and β_{ij}. If more than one doseburst hits a voxel i the synergistic effects of radiation approach (section 2.2.1) has to be applied. Equation (2.13) defines averaging methods for both α and $\sqrt{\beta}$. The total biological effect in voxel i

is given by (Wilkens and Oelfke 2006)

$$\begin{aligned}\mathcal{E}_i(\boldsymbol{w}) &= \alpha_i(\boldsymbol{w})\, D_i(\boldsymbol{w}) + \beta_i(\boldsymbol{w})\, D_i^2(\boldsymbol{w}) \\ &= \frac{1}{D_i}\left(\sum_{j=1}^{N}\alpha_{ij}D_{ij}w_j\right)\left(\sum_{j=1}^{N}D_{ij}w_j\right) + \frac{1}{D_i^2}\left(\sum_{j=1}^{N}\sqrt{\beta_{ij}}D_{ij}w_j\right)^2\left(\sum_{j=1}^{N}D_{ij}w_j\right)^2 \\ &= \sum_{j=1}^{N}\alpha_{ij}D_{ij}w_j + \left(\sum_{j=1}^{N}\sqrt{\beta_{ij}}D_{ij}w_j\right)^2. \end{aligned} \tag{2.40}$$

The biological objective function is therefore proportional to $\boldsymbol{w}^4$. The implications of this proportionality on the convexity of the objective function will be studied in the next chapter.

2.3.4 Treatment plan comparison

The termination criterion of the optimization is the relative change of the objective function value. The absolute value of the objective function by itself is not a very helpful measure to judge on the actual plan quality. It depends largely on the optimization algorithm and the penalty factors. Common means of comparing two treatment plans are visual comparison of dose distributions and the well known dose–volume histograms (DVH). Differences between plans can be quantified by dose–volume statistics. Within this work we employed the following volume specific measures:

- D_{mean} is the mean dose.
- D_p is the dose that p % of the volume receive.
- V_p is the relative volume that receives p % of the prescribed dose. Alternatively, we also use $V_{x\,\text{Gy}}$ or $V_{x\,\text{Gy (RBE)}}$ to measure the relative volume that receives x Gy or Gy (RBE).
- The inhomogeneity coefficients (IC_1 and IC_5) were defined as

$$IC_1 = \frac{D_1 - D_{99}}{D_{\text{mean}}} \qquad \text{and} \qquad IC_5 = \frac{D_5 - D_{95}}{D_{\text{mean}}}. \tag{2.41}$$

Chapter 3

Peculiarities of the (Biological) Objective Function

In this chapter we are going to study technical issues of the biological optimization as it is employed in *KonRad*. The first section will discuss the convexity of the biological objective function. Convexity is a critical criterion as only convex functions have a single well defined minimum that can be reached by gradient based optimization methods. The following section presents two approaches to determine a set of weights to initialize our optimization. This was necessary as it proved to be difficult for the optimizer to find a solution for mixed radiation modality approaches.

3.1 Convexity of the quadratic objective function for the biological effect

A rather technical issue in the design of a TPS is the convergence of the objective function. An objective function is nothing but a mathematical description of the actual problem i.e. it is supposed to characterize the quality of treatment plan. Now we can easily define two different objective functions for the very same task i.e. when optimizing particle treatment plans we can either minimize the difference between prescribed and an actual RWD per fraction (Krämer and Scholz 2000) or the difference between prescribed and actual biological effect per fraction (Wilkens and Oelfke 2006). For a single fraction RWD and biological effect are the same but the complexity of the objective functions is different. In the LQ–model the RBE (cf. equation (2.14)) and hence the RWD is proportional to the square root of a second order polynomial while the biological effect (cf. equation (2.12)) is a second order function of the dose. A common way to minimize the difference between

a prescribed and an actual value are quadratic objective functions (Oelfke and Bortfeld 2001). This increases the complexity of the objective functions even more not to mention their derivatives. Apart from the complexity the objective function's convexity is a crucial criterion for a good objective function. Only convex functions i.e. functions without multiple local minima have a well defined global minimum that can be retrieved using gradient based optimization algorithms (Boyd and Vandenberghe 2004).
The convexity of the quadaratic objective function for the biological objective employed in *KonRad* will be studied in this section. Two different types of objective functions can be distinguished in *KonRad*: those penalizing overdosage and those penalizing underdosage. In my Diploma thesis (Frese 2007) I already showed that objective functions penalizing overdosage are generally convex. Convexity of the underdosage objective functions of a single doseburst is only sustained when the objective function's domain is restricted. In this section we will extend the study of the convexity of the underdosage objective function first to 2 and than on to N doseblursts. Ahead of any specific considerations convexity is briefly defined and a few relevant criteria to determine convexity are introduced.

3.1.1 Defining and determining convexity

A function $f : \Re^n \to \Re$ is convex if for all x, $y \in \Re^n$ and all $\theta \in [0, 1]$ the inequality

$$f\left(\theta x + (1-\theta)\, y\right) \leq \theta f\left(x\right) + (1-\theta)\, f\left(y\right) \tag{3.1}$$

is fulfilled (Boyd and Vandenberghe 2004). A function f is called strictly convex if the inequality holds whenever $x \neq y$ and $\theta \in (0, 1)$. Based on these definitions various theorems have been developed to identify convex functions and operations that preserve convexity. For an overview about these theorems see chapter 3 in Boyd and Vandenberghe (2004). Within this section we are only going to use the second order condition stating that a function f is convex if and only if its Hessian $\nabla^2 f$ is positive semi–definite i.e.

$$\nabla^2 f\left(x\right) \geq 0 \Longleftrightarrow f \text{ is convex} \tag{3.2}$$

for all x. If the Hessian is positive definite f is strictly convex. The inversion of the latter condition is not true (Boyd and Vandenberghe 2004). Once two functions f_1, f_2 have been identified as convex it can be shown that the weighted sum f of these is convex if the weights λ_1, λ_2 are non–negative.

$$f = \lambda_1 f_1 + \lambda_2 f_2 \Longrightarrow f \text{ is convex} \tag{3.3}$$

3.1.2 The underdosage objective function

In this part we will study the characteristics of the underdosage objective function (2.39). Following the theorem that the weighted sum of convex functions with non–negative weights is convex (3.3) we can study the objective function F_i for each voxel independently. We restrict our considerations to those cases in which $\mathcal{E}_i > \bar{\mathcal{E}}_v$ such that $|x|_+ \equiv x$. Hence, the $|\cdot|_+$ operator can be ignored.
Our method of choice to study the convexity of equation (2.39) is the second order criterion (3.2). Therefore the first and second order derivatives of the objective function have to be calculated. The first derivative of F_i^{U} with respect to weight w_k is

$$\frac{\partial F_i^{\mathrm{U}}}{\partial w_k} = 2\left(\bar{\mathcal{E}} - \sum_{j=1}^{N}\alpha_{ij}D_{ij}w_j - \left(\sum_{j=1}^{N}\sqrt{\beta_{ij}}D_{ij}w_j\right)^2\right) \cdot \left(-\alpha_{ik}D_{ik} - 2\left(\sum_{j=1}^{N}\sqrt{\beta_{ij}}D_{ij}w_j\right)\sqrt{\beta_{ik}}D_{ik}\right) \quad (3.4)$$

and the second derivative is

$$\frac{\partial^2 F_i^{\mathrm{U}}}{\partial w_k w_m} = 2D_{ik}D_{im}\sqrt{\beta_{ik}}\sqrt{\beta_{im}}\left[\frac{\alpha_{ik}}{\sqrt{\beta_{ik}}}\frac{\alpha_{im}}{\sqrt{\beta_{im}}} + 2\left(\frac{\alpha_{ik}}{\sqrt{\beta_{ik}}} + \frac{\alpha_{im}}{\sqrt{\beta_{im}}}\right) \cdot \left(\sum_{j=1}^{N}\sqrt{\beta_{ij}}D_{ij}w_j\right) + 6\left(\sum_{j=1}^{N}\sqrt{\beta_{ij}}D_{ij}w_j\right)^2 + 2\sum_{j=1}^{N}\alpha_{ij}D_{ij}w_j - 2\bar{\mathcal{E}}\right]. \quad (3.5)$$

In the last step we assumed that $\beta_{ij} > 0$ which is reasonable for these investigations as $\beta_{ij} = 0$ would reduce our objective function to a convex least–square problem. Using $r_{ik} = D_{ik} \cdot \sqrt{\beta_{ik}}$, $s_{ik} = \frac{\alpha_{ik}}{\sqrt{\beta_{ik}}}$, $\boldsymbol{b}_i\boldsymbol{w} = \sum_{j=1}^{N}\sqrt{\beta_{ij}}D_{ij}w_j$ and

$$c = 6\left(\sum_{j=1}^{N}\sqrt{\beta_{ij}}D_{ij}w_j\right)^2 + 2\sum_{j=1}^{N}\alpha_{ij}D_{ij}w_j - 2\bar{\mathcal{E}} \quad (3.6)$$

the second derivative can be rewritten to

$$\frac{\partial^2 F_i^{\mathrm{U}}}{\partial w_k w_m} = 2r_{ik}r_{im}\left(s_{ik}s_{im} + 2\left(s_{ik} + s_{im}\right)\boldsymbol{b}_i\boldsymbol{w} + c\right). \quad (3.7)$$

3.1.2.1 Convexity in one dimension

The case of a single doseburst has already been presented elsewhere (Frese 2007). We are merely repeating the results here to complete the picture. The one dimensional objective function for underdosage is convex for all absorbed doses $d_{i1}w_1$ if the inequality

$$\alpha_{i1}^2 - 2\bar{\mathcal{E}}^{\mathrm{U}}\beta_{i1} \geq 0 \tag{3.8}$$

is fulfilled. Neither α_{i1} and β_{i1} nor $\bar{\mathcal{E}}^{\mathrm{U}}$ are arbitrary. Biological parameters and treatment constraints are intrinsic variables of the irradiated tissue and the treatment plan. The only variable that can be influenced is the weight w_1 of the doseburst and therefore a lower dose limit

$$d_{i1}w_{1,\min} = \frac{-3\alpha_{i1} + \sqrt{12\beta_{i1}\mathcal{E}_v^{\mathrm{U}} + 3\alpha_{i1}^2}}{6\beta_{i1}} \tag{3.9}$$

has been determined.

3.1.2.2 Convexity in two dimensions

Let us next consider a scenario where two beamlets ($N = 2$) irradiate a single voxel. The Hessian $\mathcal{H}$ of the underdosage objective function is positive semidefinite and therefore the objective function convex if and only if all its eigenvalues λ are greater than or equal to 0. A general expression of the second derivative of equation (2.39) has already been calculated. The eigenvalues can be determined by solving the characteristic polynomial

$$|\mathcal{H} - \lambda\mathbf{1}| = \begin{vmatrix} \frac{\partial^2 F_i^{\mathrm{U}}}{\partial w_1^2} - \lambda & \frac{\partial^2 F_i^{\mathrm{U}}}{\partial w_1 \partial w_2} \\ \frac{\partial^2 F_i^{\mathrm{U}}}{\partial w_2 \partial w_1} & \frac{\partial^2 F_i^{\mathrm{U}}}{\partial w_2^2} - \lambda \end{vmatrix} \tag{3.10}$$

$$= \lambda^2 - \lambda\left(\frac{\partial^2 F_i^{\mathrm{U}}}{\partial w_1^2} + \frac{\partial^2 F_i^{\mathrm{U}}}{\partial w_2^2}\right) + \frac{\partial^2 F_i^{\mathrm{U}}}{\partial w_1^2}\frac{\partial^2 F_i^{\mathrm{U}}}{\partial w_2^2} - \left(\frac{\partial^2 F_i^{\mathrm{U}}}{\partial w_1 \partial w_2}\right)^2 \tag{3.11}$$

$$= \lambda^2 - 2p\lambda + q \tag{3.12}$$

for its roots in λ

$$\lambda_{1,2} = p \pm \sqrt{p^2 - q}. \tag{3.13}$$

We defined the variables p, q as

$$p = r_{i1}^2 \left(s_{i1}^2 + 4s_{i1}\boldsymbol{b}_i\boldsymbol{w} + c\right) + r_{i2}^2 \left(s_{i2}^2 + 4s_{i2}\boldsymbol{b}_i\boldsymbol{w} + c\right) \tag{3.14}$$

$$q = 4r_{i1}^2 r_{i2}^2 \left(s_{i1} - s_{i2}\right)^2 \left(c - 4\left(\boldsymbol{b}_i\boldsymbol{w}\right)^2\right). \tag{3.15}$$

Given that we are only studying combinations of parameters where the underdosage objective function is non–zero the variable

$$q = 4D_{i1}D_{i2}\sqrt{\beta_{i1}}\sqrt{\beta_{i2}}\left(\frac{\alpha_{i1}}{\sqrt{\beta_{i1}}} - \frac{\alpha_{i2}}{\sqrt{\beta_{i2}}}\right)^2 \cdot \left(\left(\sum_{j=1}^{N}\sqrt{\beta_{ij}}D_{ij}w_j\right)^2 + \sum_{j=1}^{N}\alpha_{ij}D_{ij}w_j - \mathcal{E}\right) \tag{3.16}$$

is negative if we assume that $\alpha_{i1}/\sqrt{\beta_{i1}} \neq \alpha_{i2}/\sqrt{\beta_{i2}}$. Therefore the value of the square root in equation (3.13) is always greater than p and whatever value p has one of the two eigenvalues will always be negative. The Hessian is indefinite. In the unlikely case that $\alpha_{i1}/\sqrt{\beta_{i1}} = \alpha_{i2}/\sqrt{\beta_{i2}}$ the eigenvalues are $\lambda_1 = 2p$ and $\lambda_2 = 0$ i.e the Hessian would be positive semidefinite if $p > 0$. Based on these assumptions we can derive criteria similar to those for the one dimensional case that preserve convexity in this special case.

3.1.2.3 Convexity in N dimensions

We cannot directly determine whether the Hessian of the objective function is positive semi–definite and therefore convex. A weaker argument is that a function with positive definite Hessian is strictly convex. Any positive definite matrix can be decomposed into a lower triangular matrix using the Cholesky decomposition (Opfer 2001). The iterative decomposition fails if the matrix is not positive–definite.
Every symmetric positive definite matrix $A \in \mathbb{R}^N \times \mathbb{R}^N$ can be decomposed into a lower triangular matrix G with

$$A = GG^T. \tag{3.17}$$

and only positive elements on the diagonal. The elements A_{ij} of A are given by

$$a_{ij} = \sum_{k=1}^{j} g_{ik}g_{jk} \text{ for } i \geq j. \tag{3.18}$$

The inverse of equation (3.18) can be defined as an iterative decomposition rule.

$$g_{ij} = \begin{cases} 0 & \text{for } i < j \\ \sqrt{a_{ii} - \sum_{k=1}^{i-1} g_{ik}^2} & \text{for } i = j \\ \frac{1}{g_{jj}} \left(a_{ij} - \sum_{k=1}^{j-1} g_{ik} g_{jk} \right) & \text{for } i > j \end{cases} \tag{3.19}$$

Let us apply this approach to the Hessian of the N dimensional underdosage objective function. The first three elements of the iterative decomposition rule are given by

$$g_{11} = \sqrt{\frac{\partial^2 F_i^{\mathrm{U}}}{\partial w_1^2}}. \tag{3.20}$$

$$g_{12} = \left(\frac{\partial^2 F_i^{\mathrm{U}}}{\partial w_1^2} \right)^{-1/2} \cdot \left(\frac{\partial^2 F_i^{\mathrm{U}}}{\partial w_2 \partial w_1} \right) \tag{3.21}$$

$$g_{22} = \sqrt{\frac{\partial^2 F_i^{\mathrm{U}}}{\partial w_2^2} - \left(\frac{\partial^2 F_i^{\mathrm{U}}}{\partial w_1^2} \right)^{-1} \cdot \left(\frac{\partial^2 F_i^{\mathrm{U}}}{\partial w_2 \partial w_1} \right)^2} \tag{3.22}$$

From the one dimensional case we know that there are possible combinations of dose, prescribed and biological parameters where g_{11} is real and non-zero. We do know that the second derivative exists for all values of $\boldsymbol{w}$ in the domain of F_1^{U} and therefore g_{12} also exists. The third non-zero element of the matrix is g_{22} which can be rearranged to

$$g_{22} = \sqrt{\left(\frac{\partial^2 F_i^{\mathrm{U}}}{\partial w_1^2} \right)^{-1} \cdot \left[\frac{\partial^2 F_i^{\mathrm{U}}}{\partial w_2^2} \frac{\partial^2 F_i^{\mathrm{U}}}{\partial w_1^2} - \left(\frac{\partial^2 F_i^{\mathrm{U}}}{\partial w_2 \partial w_1} \right)^2 \right]} \tag{3.23}$$

$$= \sqrt{q \left(\frac{\partial^2 F_i^{\mathrm{U}}}{\partial w_1^2} \right)^{-1}}. \tag{3.24}$$

We assumed that g_{11} is real and therefore $\frac{\partial^2 F_i^{\mathrm{U}}}{\partial w_1^2} > 0$. In the previous section we already determined in equation (3.16) that q is always negative if $\alpha_{i1}/\sqrt{\beta_{i1}} \neq \alpha_{i2}/\sqrt{\beta_{i2}}$. Hence g_{22} is complex, the Cholesky decomposition fails and the polynomial is not positive definite. Unfortunately, this does not allow to judge if the objective function is convex as a positive definite Hessian is not necessary. We could not determine if there is a limited domain for which convexity is preserved.

3.1.3 Discussion and Conclusions

Unfortunately it was not possible to clearly mark a domain for which the biological objective function is convex in N dimension. The limits derived in one and two dimensions can be taken as a lower limit. In cases where the optimization does only converge slowly or not at all it might be helpful to initialize the doseburst weights $\boldsymbol{w}$ with values larger than a potential solution as the overdosage objective function is always convex. In the following section two methods will be presented to initialize the weights.

3.2 Preconditioning spot weights for simultaneous optimization of multiple radiation modalities

A major feature of *KonRad* is the use of the D_{ij} concept that does in principle allow to combine different radiation modalities in the same treatment plan as dose calculation and optimization are independent from one another. While the optimization algorithm is the same for the whole plan an individual dose engine can be selected for each beam. Once the D_{ij} matrix is calculated optimization is in principle straight forward. In practice it turns out that the problem is so ill conditioned that it will not converge to a satisfying solution no matter if we employ physical or biological optimization. For a study presented in the following chapter we have attempted to biologically optimize treatment plans consisting of carbon ion and photon fields. Our standard optimization algorithm L–BFGS–B (Boyd and Vandenberghe 2004) by default initialized with zero starting weights failed to achieve an acceptable solution before the default termination criterion (5 iterations with less than 0.1 % change of the objective function value) struck. The obtained solution did only use dose from the carbon ion beams. With the termination criterion turned off the optimizer eventually started to rise the photon doses but required more than 500 iterations to obtain an acceptable solution. When studying the problem in more detail the following issues influencing the convergence could be identified:

- The shape of the depth dose curves is probably the most important influence factor. While the peak dose of a carbon ion beam will usually be within the target it is most likely outside the target for a photon beam. Hence, an increase of the weight is on a first glance always more beneficial for particles than for photons.

- The size and shape of the D_{ij} matrix of each radiation field depends largely on the radiation modality. Not only is the number of dose bursts per field significantly different ($\sim 1,000$ up to more than $20,000$ for carbon ions vs. several 100 for photons) but the number of voxels irradiated by each dose burst is smaller for carbon ions than for photons.

- The biological parameters of the radiation modalities differ significantly. This impacts the value of the gradient (compare equation (3.4)) and also the convexity of the optimization function in general (cf. section 3.1). Let us briefly review the requirements for convexity of the one dimensional objective function where the minimum

dose $d_{\min}$ in a target voxel irradiated by a single dose burst is given by equation (3.9)

$$d_{\min} = \frac{-3\alpha + \sqrt{12\beta\bar{\mathcal{E}} + 3\alpha^2}}{6\beta}. \tag{3.25}$$

Given a prescribed lower RWD of 1.8 Gy(RBE) per fraction and a target consisting of chordoma tissue the prescribed effect $\bar{\mathcal{E}} = 0.342$. The smallest parameters will occur for photon irradiation which is as effective as the reference radiation (Co–60). A minimal dose preserving convexity in the one dimensional case is therefore $d_{\min} = 0.62$ Gy.

None of these three points can be directly influenced by the treatment planner. They are part of the physical and biological condition of the problem. The low dose limit and the delayed start of the optimizer lead us to develop two different approaches to ensure a solid starting solution and improve the convergence speed.

3.2.1 Preoptimization

As a simple, straightforward solution we optimize each of the N fields separately to deliver $1/N$ of the prescribed dose for one iteration. A single iteration of the L–BFGS–B consists of up to twenty internal iterations as the optimizer has to determine an appropriate step length and search direction. The number of internal iterations depends on the available history of previous iterations that can be used to update the Hessian. N first iterations with no history can be very time consuming. A big advantage of this approach is its independence of the radiation modality. If biological optimization is used one has to switch to physical optimization to preoptimize photon beams. Otherwise the convexity criterion may not be fulfilled and a single iteration is not sufficient to get appropriate starting weights.

3.2.2 Precalculation

In addition we implemented a heuristic approach where we precalculate the weights for each doseburst. For the precalculation we compared various methods of different levels of sophistication e.g. the analytical weight function for Bragg peaks to create a flat SOBP (Bortfeld and Schlegel 1996) was adapted. Some of these methods resulted in very good starting solutions but had the disadvantage that individual solutions were required for each radiation modality. Most of the approaches also required knowledge about the lateral (and longitudinal) doseburst distance. It turned out that a simple and universal solution was to

ensure that the mean RWD in all target voxels should be equal to $1/N$ times the prescribed RWD $\overline{D}_{\text{biol}}$. A simple function setting appropriate weights w_j of doseburst j that belong to field b is

$$w_j = \frac{\overline{D}}{N} \frac{N_t}{\sum_{j \in b} \sum_{i \in t} D_{ij}} \tag{3.26}$$

where N_t is the number of voxels i belonging to target volumes t and $\overline{D}$ is the prescribed absorbed dose. When combining photon and carbon ions their different effect has to be considered i.e. the treatment planner does not prescribe an absorbed dose but an RWD. Photons are assumed to be as effective as the reference radition i.e. the prescribed absorbed dose is equal to the prescribed RWD. For carbon ions the required absorbed dose depends on the local particle spectrum which in turn depends on the dose distribution. In our biological optimization the energy spectrum is reflected by the distribution of α_{ij}. As a rapid approximation we calculate the absorbed dose that yields the prescribed RWD using the maximum α_{ij} of each beam within the target.

$$\overline{D} = \frac{\sqrt{\alpha_{\text{max}}^2 + 4\beta \left(\alpha_{\text{x}} \overline{D}_{\text{biol}} + \beta_{\text{x}} \overline{D}_{\text{biol}}^2 \right)} - \alpha_{\text{max}}}{2\beta} \quad \text{with } \alpha_{\text{max}} = \max_{j \in b, i \in t} \alpha_{ij} \tag{3.27}$$

We assumed that β is constant across the target.

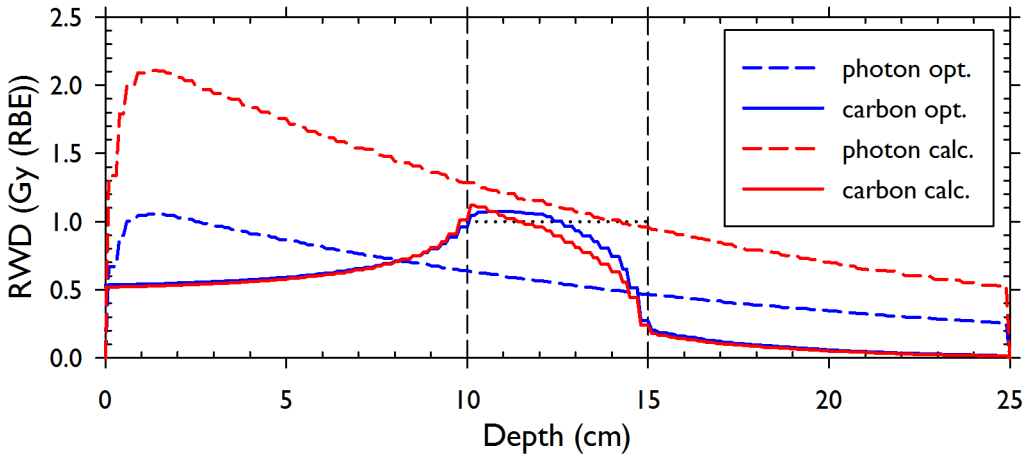

Figure 3.1: *Photon and carbon ion RWD of a single field using only either preoptimized (opt.) or precalculated (calc.) doseburst weights. No further optimization was used. An RWD of* 1 Gy (RBE) *(dotted black) was prescribed as target dose. The target is outlined by the dashed black lines.*

3.2.3 Dose distributions of the initial weights

Figure 3.1 displays an RWD profile of a preoptimized and a precalculated treatment field of either photons and carbon ions. Both methods are able to initialize the problem with weights close to a potential solution. If any of the approaches reduces the number of iterations until the problem converges to a satisfying solution has to be determined from realistic patient cases. The carbon ion RWDs are of very similar shape and average RWD while the absolute photon doses differ significantly. A significant difference is observed in the time required for preoptimization (more than 10 seconds) and precalculation (less than 0.1 seconds). We expect these timing differences to increase if we go to clinically relevant plan sizes. These considerations were employed in section 4.2 where we studied the time and number of iterations cases of relevant size required to converge.

Chapter 4

From Bench to Bed: Potential Clinical Applications of Existing Radiobiological Models

Radiobiology is a field of ongoing research. It is common knowledge that no understanding has yet been achieved. As long as patients are treated with photons a constant beam quality can be assumed throughout the patient i.e. dose may be a sufficiently accurate measure to estimate radiation damage. For particles on the other hand beam quality changes consistently while particles travel through the patient. Radiobiological considerations are essential to determine the dose that needs to be delivered to reach the treatment goals. Notwithstanding our limited knowledge, more than 50,000 patients have been treated with particles and there is a high demand for the application of biological models in the clinic. In this chapter we will take a few steps towards the use of biological optimization in the clinic. For carbon ions it is undisputed that a biological effect optimization is necessary but for protons clinical standard is the use of a constant RBE. In section 4.1 we compare the constant RBE to an existing variable proton RBE model to better understand the risks but also the potential of a variable RBE optimization. Assuming our RBE predictions are sufficiently accurate we can exploit new methods of treatment plan optimization. One option is the combination of multiple radiation modalities in the same treatment plan, a so far mostly unused feature of *KonRad*. A treatment planning procedure using a simultaneous carbon ion boost for a regular photon plan is introduced in section 4.2. A regular technical issue in treatment planning is the accuracy of the range prediction and the patient positioning. Treatment plans that are robust against range and setup uncertainties can be generated using worst case optimization. This concept was extended to biological

optimization in section 4.3 and compared to the conventionally used margin concept.

4.1 Variable or constant proton RBE?

In the second chapter the functional relationship between radiation quality and biological effectiveness was discussed. Currently it is practice in clinical radiotherapy with protons to ignore the variability of these dependencies and assume a constant RBE of 1.1 as it is recommended by the ICRU (Paganetti *et al.* 2002, ICRU 2007). Figure 2.2 shows estimates of the proton RBE for a simple SOBP. Clearly, the RBE is both under– and overestimated using a constant RBE of 1.1 by more than 10 % in some regions though its mean across the SOBP is still 1.1. It can be questioned how much value a single field SOBP has for a clinical setting were multiple beams overlap and irregular shaped fields are used. We are therefore going to apply the LSM model (section 2.2.2) to four clinical cases and evaluate the impact of the variable RBE. This comparison focuses on the differences in RWD that are observed when a treatment plan optimized with a constant RBE is recalculated with a variable RBE. The potential risks of using a constant RBE approach with respect to target volumes and organs at risk (OARs) especially in regard to an underestimated extension of the bioeffective range (Robertson *et al.* 1975) are also evaluated. This uncertainty in variations of RBE values and the positioning of the bioeffective range of protons in the tissues complicates the assessment of proton treatment plans and their safety for treatment delivery. Additionally, we will study the influence of the choice of radiosensitivity parameters for the same organ and show that it is feasible to optimize treatment plans biologically and achieve a similar plan quality as a treatment plan optimized with a constant RBE. This section has been previously published (Frese *et al.* 2011a).

4.1.1 Selecting patients, treatment plans, and biological input parameters

Patient selection and definition of volumes of interest Four patients with nasopharyngeal carcinoma who were treated previously with intensity-modulated photon radiotherapy at the German Cancer Research Center (DKFZ), Heidelberg, Germany were selected. These head and neck (HN) tumors are potentially suitable targets for proton therapy as they require highly conformal dose distributions with steep dose gradients towards near risk structures. The TNM classifications of the four tumors were were: T1N0M0, T2N2M0, T3N2M0 and T4N1M0. The original computed tomography (CT) data sets with a slice thickness of 3 mm were used for target definition and IMPT planning. Based on the clinical

data and pre–therapy diagnostic CT/MR images, the gross tumor volumes of the primary tumor (GTV–T) and of the nodal metastases (GTV–N) were delineated on each CT slice. In all cases, an automatic margin of 1.5 cm was added to GTVs in order to create PTVs. The elective treatment volume (PTV-N) consisted of bilateral cervical lymph node stations in levels Ib to V. All PTVs were modified wherever they encountered neural tissues or bony structures without evidence of tumor infiltration. The delineated OARs and the applied dose/dose–volume constraints are listed in table 4.1.

Table 4.1: *Dose and dose–volume constraints for OARs in all plans. TM = temporo-mandibular.* $D_{\max}$ *is the absolute maximal dose in a single voxel.*

Volume	Dose (Gy (RBE))
Spinal cord	$D_{\max} \leq 50$
Brainstem	$D_{\max} \leq 60$
Temporal lobes	$D_{\max} \leq 65$
TM joints	$D_{\max} \leq 60$
Optic chiasm & nerves	$D_{\max} \leq 54$
Eyes	$D_{\max} \leq 25$
Inner ears	$D_{\text{mean}} < 45$
Mid-external ears	$D_{\text{mean}} < 40$
Larynx	$D_{\text{mean}} < 30$
Trachea/esophagus	$D_{\text{mean}} < 30$
Parotid glands (single gland)	$D_{\text{mean}} < 26$

Dose prescription and treatment planning Dose prescriptions in RWD for all fractions to PTVs of macroscopic tumor (PTV–66) and elective volumes (PTV–54) are 66 Gy (RBE) and 54 Gy (RBE), respectively, to be delivered in 30 fractions with the simultaneous integrated boost technique.

For preparation of all IMPT plans we used *KonRad*. We used four coplanar beams with gantry angles of 90°, 135°, 225°, and 270° covering the nasopharyngeal cavity and upper neck and three coplanar beams with gantry angles of 0°, 135°, and 225° covering the lower neck. This setup was chosen to avoid range uncertainties originating from the nasal cavities and unnecessary dose to the shoulder joints.

For each patient, three IMPT plans were prepared. The first treatment plan was physically optimized (IMPT–PO plans) assuming a constant RBE value of 1.1 in the whole patient i.e. the RWD is calculated from the absorbed dose by a simple multiplication with 1.1. In the second step, the IMPT–PO plan was recalculated (IMPT–RE plans) employing a variable RBE model. Here, the absorbed dose optimized for the IMPT–PO plans was kept

constant and only the RWD changed. A comparison of these two plans gives information about the variations in the RWD distributions purely due to the biological dose calculation. Finally, IMPT–BO plans were biologically optimized to investigate whether it was possible to generate treatment plans of at least similar quality as the IMPT–PO plans when a variable RBE model is applied. The 3D IMPT treatment plans were created using the virtual proton device introduced in section 2.3.1. Proton spots were placed with a lateral distance of 5 mm and in a distance of 3 mm along the beam axis.

Plan Comparison For comparison of the treatment plans we used the dose–volume statistics outlined in section 2.3.4. During the 3D RBE calculation and optimization of the plans one set of biological parameters was assigned to each defined tissue. Based on the published data for parotid glands and the spinal cord we used more than one set of parameters in order to evaluate the variations of RWD distributions within the organs in the same plans.
In delineation of target volumes and OARs on CT images often two or more structures could overlap and thereby the same voxel could belong to more than one structure. However, in the optimization process only one structure with a certain set of parameters could be assigned to each voxel. Since calculation of dose–volume data for each structure required inclusion of all voxels within the structure we recalculated RWD distributions for each structure individually. This means that different biological parameter sets were assigned to the shared voxels depending on the structure to be evaluated. With this approach the same voxel could contribute to more than one volume of interest with different RWDs.
In our target definition PTV–66 was embedded in PTV–54. In order to evaluate the RWD distribution in PTV-54 more accurately with respect to dose homogeneity and dose gradients we excluded all voxels from PTV–66 in calculation of the DVH and dose–volume parameters. Overlapping regions with OARs were not excluded from PTV–54.

Deriving Model Parameters In order to calculate RBE variations within the treatment volume, values of tissue specific parameters α_x and β_x for low–LET reference radiation modality are required. These parameters were calculated in accordance to Lof *et al.* (1995) based on the parameters D_{50}, γ, and α_x/β_x extracted from the literature for each volume of interest. Employed parameters can be found in table 4.2. If not stated differently the values from Schultheiss (Schultheiss 2008) and Eisbruch (Eisbruch *et al.* 1999) for spinal cord and parotids were employed, respectively. Non–specific normal tissues were assigned a constant RBE value of 1.1.
In the LSM two model specific parameters have to be determined for each tissue: α_0 and

Table 4.2: *Biological parameters employed in this study.* α_0 *was calculated using* $\lambda_{1.1} = 0.008\ \mu\text{m keV}^{-1}\text{Gy}^{-1}$.

Tissue	Endpoint	D_{50} (Gy)	γ	Ref.	α/β (Gy)	α_x (Gy^{-1})	$\beta_x = \beta_p$ (Gy^{-2})	α_0 (Gy^{-1})
Nasoph. cancer T1 & T2	Tumor control	57.0	2.7	Cronqvist (1995)	10	0.1124	0.0112	0.1084
Nasoph. cancer T3 & T4	Tumor control	70.5	2.5	Cronqvist (1995)	10	0.0854	0.0085	0.0814
Subclinical disease	Tumor control	27.0	0.6	Withers *et al.* (1995)	10	0.0554	0.0055	0.0514
Brainstem	Necrosis / infarction	65.1	2.4	Cronqvist (1995)	2	0.0532	0.0266	0.0492
Spinal cord	Myelitis / necrosis	68.6	1.9	Cronqvist (1995)	2	0.0407	0.0203	0.0367
Spinal cord (Schultheiss)	Myelopathy (cervical cord)	69.4	4.7	Schultheiss (2008)	0.87	0.0577	0.0663	0.0537
Optic nerves	Blindness	65.0	2.3	Cronqvist (1995)	2	0.0511	0.0256	0.0471
Chiasm	Blindness	65.0	2.3	Cronqvist (1995)	2	0.0511	0.0256	0.0471
Eyes	Blindness	65.0	1.8	Cronqvist (1995)	2	0.0407	0.0203	0.0367
Brain / temporal lobes	Necrosis / infarction	60.0	2.6	Cronqvist (1995)	2	0.0620	0.0310	0.0580
Parotids	Xerostomia	46.0	1.8	Cronqvist (1995)	3	0.0675	0.0225	0.0635
Parotids (Eisbruch)	Flow ratio < 25 %/1 year	28.4	2.2	Eisbruch *et al.* (1999)	3	0.1300	0.0433	0.1260
Parotids (Roesink)	Flow ratio < 25 %/1 year	39.0	0.9	Roesink *et al.* (2001)	3	0.0413	0.0138	0.0373
Inner Ears	Sensori-neural hearing loss	50.0	0.7	Honoré *et al.* (2002)	3	0.0265	0.0088	0.0225
Middle–external ears	Chronic serous otitis	65.0	3.5	Cronqvist (1995)	3	0.0915	0.0305	0.0875
Temporomandibular joints	Marked trismus	70.3	3.8	Cronqvist (1995)	3	0.0918	0.0306	0.0878
Larynx	Laryngeal edema	80.0	1.2	Cronqvist (1995)	3	0.0281	0.0094	0.0241
Trachea–esophagus	Clinical stricture	68.0	2.8	Cronqvist (1995)	3	0.0708	0.0236	0.0668

λ. We calculated α_0 using equation (2.15) and the linear parameter λ was obtained using the second method presented in section 2.2.2. Hence, we are not using a λ value that was obtained from measurements but one that reflects the clinically observed mean RBE of 1.1. We will refer to this value as $\lambda_{1.1}$. As evidence for individual $\lambda_{1.1}$ values for each tissue is scarce we decided to use the same for all tissues. The mean RBE of 1.1 reported by Paganetti *et al.* (2002) is based on the clinical experience in target volumes. We therefore decided to extract the mean dose and LET from the GTV i.e. PTV–66 and calculated individual $\lambda_{1.1}$ values for each patient using equation (2.18). The resulting values were then averaged for a global $\lambda_{1.1}$ that was used for all variable RBE calculations.

4.1.2 Results

Determination of the linear parameter λ Table 4.3 shows the mean LET and mean dose in PTV–66 for one single fraction extracted from the IMPT–PO plans for four patients. Based on the parameters given in table 4.2 $\lambda_{1.1}$ was calculated according to equation (2.18). The average value for all four patients was $\overline{\lambda_{1.1}} = 0.008\ \mu\text{m}/\,(\text{keV} \cdot \text{Gy})$. It will be used for further calculations of the RWD and biological optimizations. Since non–specific normal tissues were assumed to have a constant RBE of 1.1 for these tissues $\lambda = 0.0\ \mu\text{m}/\,(\text{keV} \cdot \text{Gy})$.

Table 4.3: *Mean LET $\overline{L}$ and absorbed dose $\overline{D}$ in the PTV–66 for IMPT–PO plans and the value of $\lambda_{1.1}$ for an RBE of 1.1 for the mean values.*

Patient	stage	$\overline{L}$ (keV/μm)	$\overline{D}$ (Gy)	$\lambda_{1.1}$ (μm/keV/Gy)
A	T4	2.13	2.00	0.0074
B	T3	2.22	2.00	0.0070
C	T1	2.35	2.00	0.0086
D	T2	2.25	2.00	0.0091

Treatment plan comparison Tables 4.4 and 4.5 show the mean values for dose–volume statistics for IMPT–PO, IMPT–RE and IMPT–BO plans. The results demonstrate that for PTV–54 there was a general increase of RWD in IMPT–RE plans compared to IMPT–PO plans. For PTV–66, the RWD increments were seen mainly in the high dose regions (the tail of DVHs) except for patient A whose IMPT–RE plan showed a general rise of the dose in the whole target. Indeed, in patients C and D the mean doses in PTV–66 were 0.4 to 0.6 Gy (RBE) lower than the IMPT-PO plans. On average D_{mean} of PTV–66 and PTV–54

Table 4.4: *Dose–volume statistics for PTV–66 and PTV–54 averaged over all four patients. To asses the difference between the patients the standard deviation (σ) of the mean is also displayed. All doses are RBE–weighted absorbed doses given in Gy (RBE) and all volumes are given in percent of the total volume of the structure.*

		IMPT–PO		IMPT–RE		IMPT–BO	
		Mean	σ	Mean	σ	Mean	σ
PTV–66	D_{95}	62.87	1.01	63.95	1.68	63.11	1.04
	D_5	67.37	0.75	70.42	2.35	67.29	0.8
	D_{99}	59.07	2.61	60.77	2	59.42	2.42
	D_1	68.59	1.59	72.91	3.34	68.39	1.56
	D_{mean}	65.65	0.24	66.92	1.87	65.73	0.18
	σD_{mean}	1.84	0.54	2.17	0.68	1.56	0.63
	V_{95}	95.3	2.23	96.13	4.37	95.93	1.9
	V_{105}	0.91	1.36	18.35	24.14	0.84	1.43
	IC 1	0.07	0.02	0.1	0.02	0.06	0.02
	IC 2	0.14	0.06	0.18	0.06	0.14	0.06
PTV–54	D_{95}	51.39	1.33	54.88	1.51	51.92	1.13
	D_5	56.53	2.53	65.77	2.25	58.05	4.28
	D_{99}	46.94	2.97	53.05	2.86	48.07	2.42
	D_1	58.29	3.78	69.54	3.01	60.57	6.09
	D_{mean}	53.96	0.33	58.93	1.46	54.35	0.66
	σD_{mean}	1.86	1.05	3.48	0.79	2.08	1.46
	V_{95}	95.2	2.83	99.34	0.95	96.23	2.51
	V_{105}	4.32	6.34	69.51	17.77	6.48	9.31
	IC 1	0.09	0.07	0.18	0.04	0.11	0.1
	IC 2	0.21	0.12	0.28	0.08	0.23	0.15

increased modestly in the order of 1.3 and 5.0 Gy (RBE), respectively. The IMPT–RE plans were in general more inhomogeneous than the original plans. The absolute difference between mean V_{105} for PTV–66 and PTV–54 were 17.4% and 65.2%, respectively.
When the IMPT plans were biologically optimized the difference between the mean DVH parameters became very modest for both PTV–66 and PTV–54.
With respect to OARs, there was a small increase of D_{mean} or D_{max} in IMPT–RE plans for most of the tissues (tables 7 and 8). In OARs with mostly parallel structures the dose increments in D_{mean} was below 4.33 Gy (RBE). In neural structures, the increase of the mean D_{max} was < 3 Gy (RBE) and the doses were still far below the tolerance thresholds of the structures. For structures such as inner ears, larynx and trachea–esophagus the mean D_{max} (D_1 or D_5) was increased up to 11 Gy (RBE). For the spinal cord and middle–external ears, there was a slight decrease in D_{mean} and D_{max}.

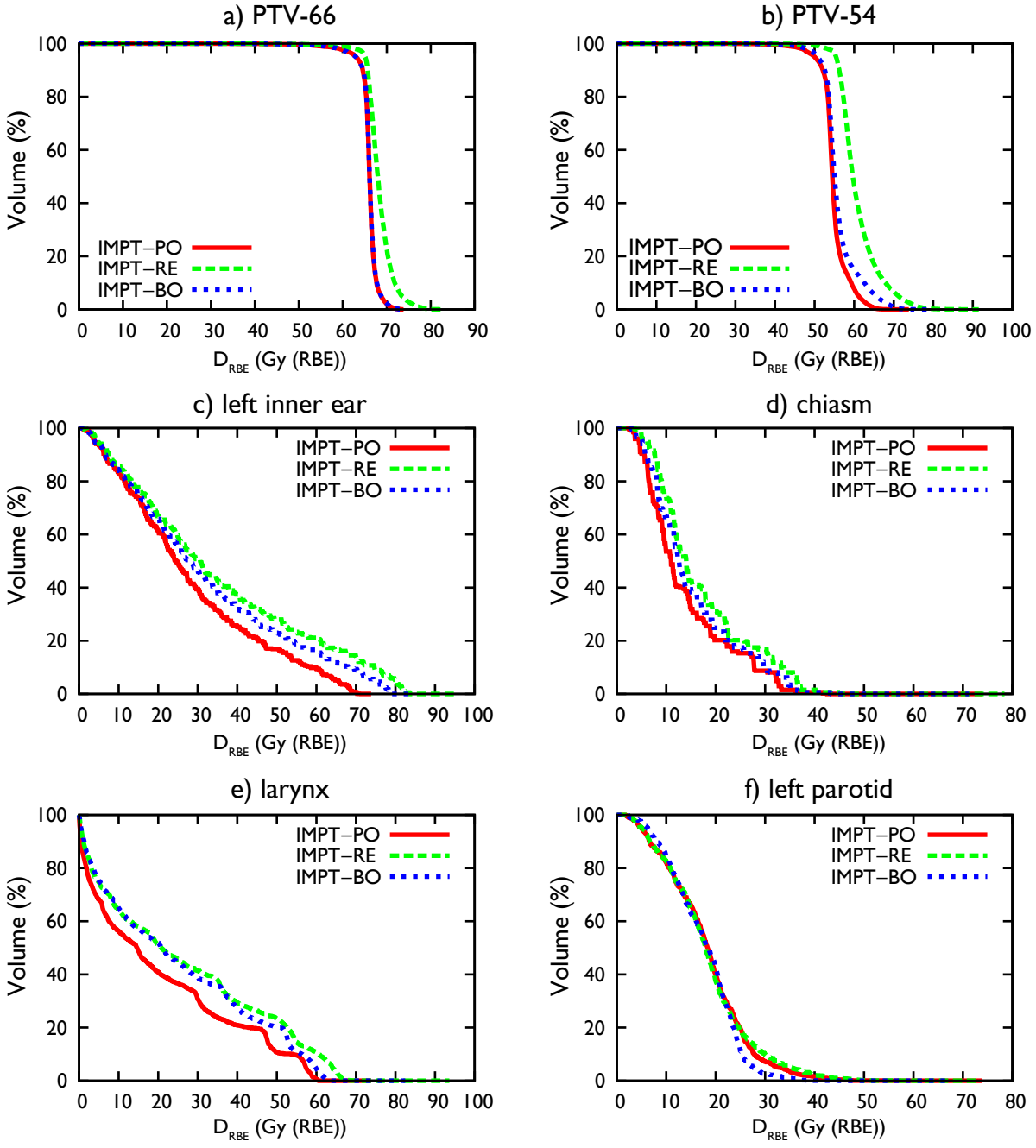

Figure 4.1: *RBE–weighted absorbed dose (D_{RBE}) volume histograms for one exemplary patient with a T4N1M0 tumor illustrating the difference between constant (IMPT–PO) and variable (IMPT–RE) RBE for the same absorbed dose distribution. The biological optimization (IMPT–BO) obtains similar results than IMPT–PO.*

In IMPT–BO plans, mean D_{mean} or D_{max} could be variable (lower or higher) for OARs and in most cases doses could be kept below the dose–volume constraints.
Figure 4.1 shows the DVHs of three sets of IMPT plans for target volumes and some OARs for the patient with the T4N1M0 tumor. As it was expected the effect of high LET in less radiosensitive late responding tissues (lower α_0 values) such as inner ears, optic chiasm and larynx was higher which demonstrated itself by a shift of the DVH curves to the right in IMPT–RE plans. However, in the parotid glands with a higher α_0 value, a variable LET made insignificant changes in the RWD distribution for the most parts of the tissue.
When we used different sets of biological data for biological calculation and optimization of the dose in parotid glands and spinal cord (Cronqvist (Cronqvist 1995), Roesink (Roesink *et al.* 2001) and Eisbruch (Eisbruch *et al.* 1999) for parotid glands and Cronqvist and Schultheiss (Schultheiss 2008) for spinal cord) we could not see any major change in the dose distribution parameters in either of the organs (see table 4.6).

Influence of the LET on RWD In figure 4.2 for each of the patients the distribution of RWD, absorbed dose and LET in PTV–66 are visualized using adapted DVHs. Please note that for patient A and B (T3 and T4 tumors) the applied biological parameters differed from those used for patients C and D (T1 and T2 tumors).
For all four patients the IMPT–RE RWD distribution is smeared out as the LET variations were not considered during optimization. Additionally for patients A and B the mean target RWD is slightly increased. In the IMPT–BO plans the biological optimization could compensate the influence of the LET in different ways for each of the patients. In patient A the absorbed dose is reduced and the LET increased. In contrary in patient B the mean absorbed dose does not change and the LET is reduced. In patients C and D the mean absorbed dose increases and the mean LET is reduced. The absorbed dose is less homogeneous in PTV–66 for all four patients in the IMPT–BO plans compared to the IMPT–RE plans. General trends in the change of the LET distribution if optimized biologically instead of physically were not observed.

4.1.3 Discussion

A constant lambda for all tissues The choice of λ is crucial for the estimation of tissue response on higher LETs. Introduction of a single value for λ in all tissues might not be the most accurate approach but it has been a feasible one in our model since currently there are no clinically verified values available. The relative change in the biological effect with LET is larger for those tissues that have a small α value, an effect that has been

Table 4.5: *Dose–volume statistics for organs at risk averaged over all four patients. To asses the difference between the patients the standard deviation (σ) of the mean is also displayed. All doses are RBE–weighted absorbed doses given in Gy (RBE) and all volumes are given in percent of the total volume of the structure.*

		IMPT–PO		IMPT–RE		IMPT–BO	
		Mean	σ	Mean	σ	Mean	σ
Spinal cord	D_1	24.95	0.68	23.74	1.89	24.83	0.16
	D_5	23.08	0.62	21.61	0.61	23.51	1.16
Brainstem	D_1	30.43	6.46	31.65	7.05	30.68	6.59
	D_5	22.62	4.93	23.49	6.9	22.84	5.7
Optic chiasm	D_1	15.66	17.98	17.71	19.97	15.11	17.86
	D_5	14.6	16.57	16.48	18.46	14.44	17.03
Optic nerves	D_1	21.19	19.68	23.57	20.63	20.96	19.55
	D_5	19.18	18.23	21.62	19.54	18.99	18.46
Temporal lobes	D_{mean}	4.74	2.86	4.82	2.85	4.22	2.68
	D_1	40.21	9.94	42.23	10.34	37.25	9.69
	D_5	23.49	9.96	24.25	10.26	20.77	9.8
Eyes	D_{mean}	0.26	0.54	0.38	0.76	0.18	0.34
Inner ears	D_{mean}	16.36	8.34	19.17	10.39	19.32	9.32
	D_1	45.39	19.31	53.82	22.44	50.89	21.63
	D_5	39.21	20.44	45.43	23.05	42.95	20.71
Mid.–ext. ears	D_{mean}	15.05	5.57	14.3	5.24	14.05	6.67
	D_1	30.48	5.29	29.78	4.93	28.88	5.85
	D_5	26.54	5.75	25.08	5.35	24.98	6.88
Parotid gl.	D_{mean}	16.3	6.04	16.63	6.04	14.97	6.13
	$V_{26\text{Gy(RBE)}}$	12.16	12.53	14.41	12.04	9.12	12.38
	D_{30}	18.57	4.89	19.34	5.96	16.82	5.06
TM joints	D_{mean}	19.12	5.31	22.45	4.34	20.25	3.31
	D_1	43.68	7.91	44.04	8.21	40.88	6.56
	D_5	35.16	3.93	35.81	4.46	34.36	3.49
Trachea	D_{mean}	10.02	1.03	10.85	2.84	16.73	13.04
	D_1	36.17	3.29	40.99	3.95	31	3.67
	D_5	26.14	2.9	30.14	3.59	21.27	7.38
Larynx	D_{mean}	16.33	6.76	20.75	7.25	20.55	6.64
	D_1	51.36	7.78	62.77	2.79	55.3	5.95
	D_5	47.48	11.38	55.04	7.36	51.43	9.02

Table 4.6: *The RWD distributions for parotid glands and spinal cord have been recalculated with different parameter sets. The results are averaged over all four patients (mean). To asses the difference between the patients the standard deviation (σ) of the mean is also displayed. All doses are RBE–weighted absorbed doses given in Gy (RBE) and all volumes are given in percent of the total volume of the structure. On the left recalculated IMPT–PO plans are shown and on the right recalculated IMPT–BO plans.*

	IMPT–PO						IMPT–BO					
Parotid glands												
Reference	Cronqvist		Roesink		Eisbruch		Cronqvist		Roesink		Eisbruch	
	Mean	σ	Mean	σ	Mean	σ	Mean	σ	Mean	σ	Mean	σ
D_{mean}	17.8	7.7	18.6	8.2	16.6	6	17.1	7	17.4	7.6	15	6.1
$V_{26\text{Gy(RBE)}}$	16.4	14.5	17.7	15.3	14.4	12	12.1	13.8	15.3	13.6	9.1	12.4
D_{30}	21.6	9.4	22.4	10.4	19.3	6	19.3	7	20.3	7.6	16.8	5.1
Spinal cord												
Reference	Cronqvist		Schultheiss				Cronqvist		Schultheiss			
	Mean	σ	Mean	σ			Mean	σ	Mean	σ		
D_1	25.3	3.7	23.7	1.9			26.2	1.8	24.8	0.2		
D_5	22.4	1	21.6	0.6			24.1	1.6	23.5	1.2		

reported before for carbon ions (Weyrather *et al.* 1999). Compare, for example, the change of RWD from IMPT–PO to IMPT–RE plans for parotid glands (largest α_x value) and inner ears or larynx. These changes are significantly more pronounced for the last two tissues.

The role of the LET Introduction of a biological optimization changes the LET distributions of a treatment plan. The optimizer combines absorbed dose and LET locally and sometimes introduces distinct changes in the distribution. The resulting physical dose distribution is definitely less homogeneous for the IMPT–BO plans compared to the IMPT-PO plans but this is expected.

RBE–weighted dose distributions In this simulation study, we have used a theoretical model to estimate the 3D RBE variations in IMPT plans assuming that such variations are tissue, absorbed dose, and LET dependent in the patients. The variable RBE calculations of our IMPT plans resulted in small RWD increments in the targets in general despite of assuming a high value for the α/β–ratio ($\alpha_x/\beta_x = 10$ Gy) in these tissues. A rise of the RBE above 1.1 in the targets may translate into more favourable tumor control rates. The disadvantage of such RWD increments especially on the high RWD side is when large volumes of normal tissues are embedded within the target. Yet in other cases we observed an RBE value slightly lower than 1.1 in IMPT–RE plans which could jeopardize the tumor control rates. The change in RBE depends mainly on the relative size of α_x to λ as it can be expected from equation (2.17). The smaller α_x the higher the impact of the LET. This was demonstrated in the patient with T4N1M0 tumor where RBE variations in normal tissues with higher sensitivity for dose per fraction, i.e. smaller α_x values such as inner ears and larynx, were more apparent. On the other hand, RBE variations in OARs such as parotid glands with a relatively high radio–sensitivity ($\alpha_x = 0.13$ Gy^{-1}) were insignificant with practically no impact on the average dose deposited in the organ. For neural structures such as optic apparatus, spinal cord, and brainstem, the dose depositions in the IMPT–PO plans were low and thereby small increases in the D_{mean} or D_{max} due to RBE variations in IMPT–RE plans were still below the tolerance of these tissues. Altogether our results suggest that the clinical significance of RBE variations in many late reacting OARs is dependent on the tissue type, the physically deposited dose and the location of the organ with respect to the high dose target volumes.
In the variable RBE model employed in this study, we have made several biological assumptions that might have confounded our results. Most of the basic biological parameters for calculation of α_x and β_x (D_{50} and γ) for target volumes and normal tissues were adapted from the literature. The uncertainty in the validity of these empirical parameters by itself

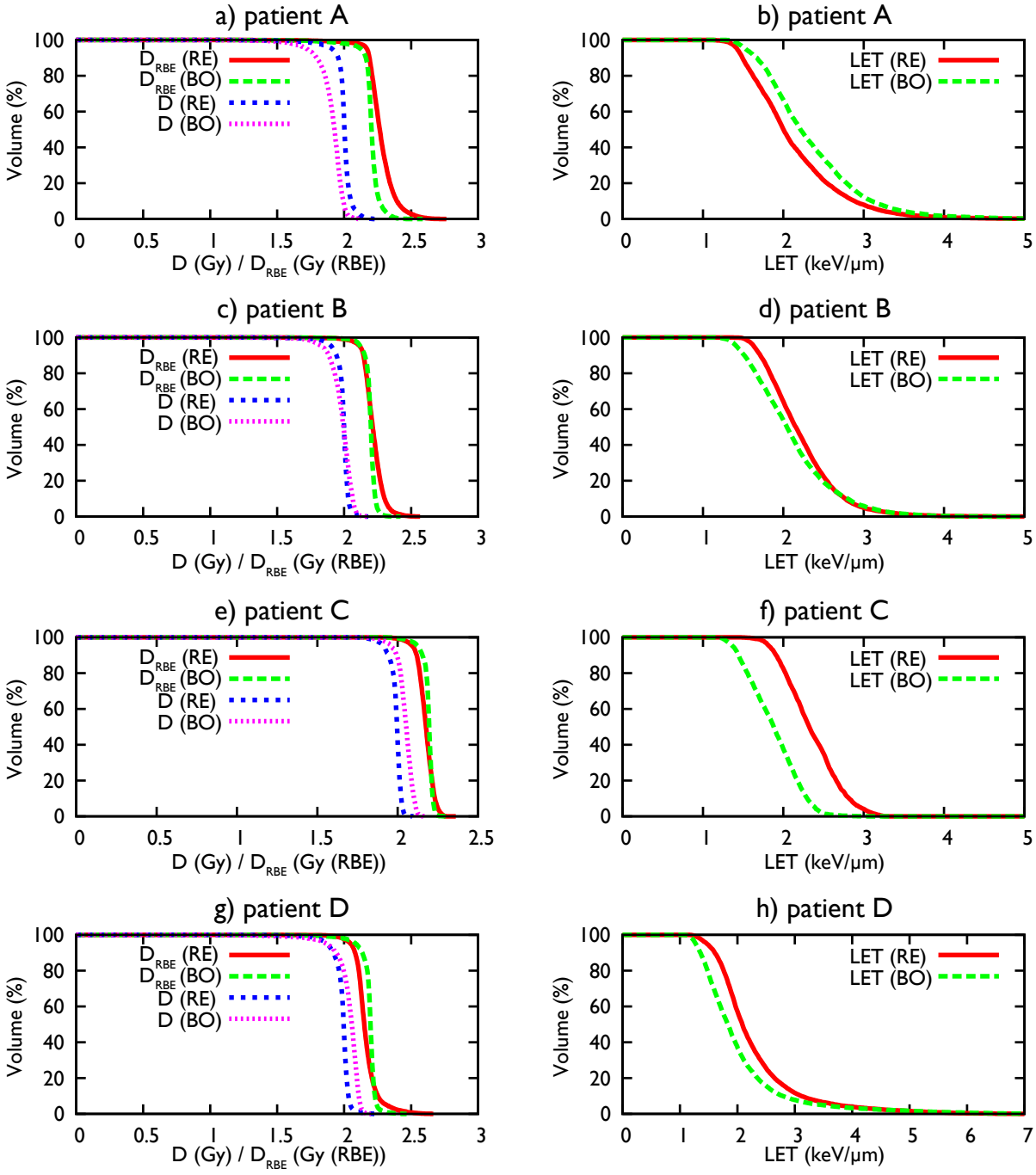

Figure 4.2: *Dose–volume histograms showing the absorbed dose D, the RBE–weighted absorbed dose D_{RBE} and the LET of each patient's PTV–66.*

is a source of error. Nevertheless, these data are used in clinical photon radiation treatment planning due to the absence of more reliable data and therefore their application in this study can be justified. For organs such as parotid glands, spinal cord and inner ears we applied biological parameters which were based on recent publications in which 3D dose depositions in the organs were correlated with measurable endpoints (Schultheiss 2008, Eisbruch *et al.* 1999, Roesink *et al.* 2001, Honoré *et al.* 2002). Neither for parotid glands nor for the spinal cord could we find any clinically significant changes in the dose distribution parameters in IMPT–RE plans when different sets of tissue specific parameters (D_{50} and γ) were used. This reflects that at least for these two tissues and for the dose ranges used in our plans, the variations of RBE values based on the tissue-specific parameters in use will have no major clinical impact in terms of rate of xerostomia or myelopathy.
Finally, the results of this study showed that optimization of IMPT plans based on a variable RBE model is also feasible. Our IMPT–BO plans were at least as good quality as IMPT–PO plans. It is possible that further optimization of IMPT–BO plans with respect to individual tissues and targets could have improved the quality of the plans.

Biological assumptions In the current study, variations in tissue oxygenation and their impact on RBE were not considered. It is known that oxygen enhancement ratio (OER) decreases with increasing LET (Barendsen *et al.* 1966, Furusawa *et al.* 2000). However, these changes seem to be relevant for LET values higher than the maximum LET values observed in this study. As OER is usually not considered in radiation treatment planning for photons, we have used the same strategy for protons to get comparable results.
Fractionation effects were not explicitly considered in this work. We chose $\lambda_{1.1}$ as a function of the dose per fraction. Therefore it has to be adjusted for other fractionation doses to keep the mean RBE at 1.1.

4.1.4 Conclusions

In conclusion, the results of this study indicate that the application of a variable RBE model in the planning of IMPT plans is clinically more useful for accurate assessment of feasibility of the plans from a biological point of view. However, more robust and clinically validated biologically data are needed for accurate assessment of RBE variations within the target and late responding tissues especially for those located in the vicinity of high dose targets. According to our model radio–resistant normal tissues have a higher risk of accidental overdosage than radio–sensitive tissues. Therefore the LET distribution in these regions should be closely monitored. LET hot spots should be avoided in any case.

4.2 A simultaneous carbon ion boost

Carbon ions and protons are frequently used in combination with photon therapy to give a dose boost to the macroscopic tumor residual to improve local control. Usually the boost is applied sequentially i.e. prior to the photon treatment or after it is completed (Schulz-Ertner *et al.* 2004, Nihei *et al.* 2005). Slater *et al.* (2005) used a concomittant proton boost: on the last 17 days of the conventional photon treatment patients received an additional fraction of proton radiotherapy to a boost volume. Both scenarios share certain issues that compromise the plan quality. A treatment involving two different radiation modalities (in different fractions) requires at least two treatment plans. These treatment plans have to be optimized separately, they have to be combined for evaluation, and the treatment planner has to go back to each TPS to adapt the plans. The combined dose distributions have to be evaluated carefully as the overlap of two radiation modalities may create local hot spots since the treatment planning systems do not know that the other treatment plan exists. Overall this is a very time consuming procedure that does not even guarantee that the best possible treatment plan is obtained. Additionally, this kind of treatment planning disregards the potential of particles to shape steep dose gradients. With a fixed ratio of carbon ion to photon dose we cannot properly combine the benefits of protons and carbon ions. To overcome both problems, the fixed ratio and the multiple treatment plan issue, we propose a novel approach where the patient is treated with a simultaneous carbon ion boost as an addition to a regular photon plan. The latest generation of carbon ion therapy centers like the NROCK in Kiel, Germany, will have photon and carbon ion treatment rooms in such close proximity that it is possible to keep the time between both radiation modalities so short that they can be considered to be in one fraction. The advantages of such a simultaneous boost are evident: only one treatment plan has to be optimized and the TPS decides on the best combination of particle and photon dose. Thereby, local hot spots can be avoided and the high dose gradients of particles can be exploited. In addition, the patient should receive a lower integral dose compared to a sequential particle boost. Treatment plans for the latter tend to exhibit an increased normal tissue and non–boost target area dose. In a simultaneous boost optimization additional doses from carbon ion fields outside the boost are automatically considered in the photon dose prescription. This method was developed for carbon ions and photons but it should work as well for protons as boost irradiation.

4.2.1 Preparation of the TPS and its input parameters

The D_{ij} approach employed in our in–house TPS *KonRad* separates dose calculation from optimization and allows to mix different radiation modalities in the same treatment plan. For each radiation modality a dedicated dose calculation algorithm can be used (cf. section 2.3.2). The difficulty in combining two radiation modalities of different biological effectiveness like carbon ions lies in the calculation of the total biological effect and its optimization. The total effect of different radiations can be obtained using the synergistic effect of radiations approach (Zaider and Rossi 1980) as it is used in the biological optimization for carbon ions implemented in *KonRad* (Wilkens and Oelfke 2006). Details of this approach are discussed in section 2.2.1. It requires in addition to each D_{ij} element a respective set of parameters α_{ij} and β_{ij} for each combination of voxel i and doseburst j. We already assumed that the quadratic parameter β_{ij} is constant and equal to the reference parameter β_{x}. Additionally, therapeutic photon beams are assumed to be as biologically efficient as the reference radiation. Therefore, $\alpha_{ij} \equiv \alpha_{\mathrm{x}}$ if j is a photon doseburst. For carbon ions the previously introduced depth dependent α input is used (section 2.3.2). The same tissue parameters were applied throughout all volumes in both phantom and patient cases. In accordance with the current clinical practice at HIT we used chordoma tissue (reference parameters $\alpha_{\mathrm{x}} = 0.1\ \mathrm{Gy}^{-1}$ and $\beta_{\mathrm{x}} = 0.05\ \mathrm{Gy}^{-2}$) for all tissues.
The aim of this study is to use a simultaneous carbon ion boost. Hence, we had to ensure that carbon ions dominate the delivered dose only inside the boost volume. In all other volumes the carbon ion dose shall only be considered in order to stay within the bounds of the prescribed doses. Therefore, a modified version of *KonRad* was developed that allows the user to choose individual targets for each field. Dosebursts are then only placed across the respective target volumes. The optimization itself is not aware of any restrictions.
In the previous chapter we already discussed that treatment plans employing different radiation modalities are generally ill conditioned and converge only slowly to an acceptable solution. Placing dosebursts only in some regions of the target does not reduce this issue. Hence, before using the novel method in multiple patient cases we tested the two methods proposed in section 3.2 both in regard to the time it took to generate initial beam weights and to the convergence speed.

4.2.1.1 Fractionation schemes

Whichever radiation modality is used to deliver a boost we can come up with a number of fractionation schedules to combine it with a basic treatment plan:

(i) A simultaneous (carbon ion or photon) boost is given in all fractions.

Table 4.7: *Four fraction schemes delivering the same total RWD of 72 Gy (RBE) in the . Each volume is irradiated for N_{frac} fractions with a RWD D_{frac} up to a total dose of D_{total}. All RWD are given in Gy (RBE).*

		Boost		Target		Radiation	
Scheme	N_{frac}	D_{frac}	D_{total}	D_{frac}	D_{total}	X–rays	C–12
SIM–X	30	2.4	72.0	1.8	54	✓	
SIM–30	30	2.4	72.0	1.8	54	✓	✓
SEQ	6	3.0	18.0	–	–		✓
	30	1.8	54.0	1.8	54	✓	
SIM–15	15	3.0	45.0	1.8	27	✓	✓
	15	1.8	27.0	1.8	27	✓	

(ii) The boost volume is sequentially irradiated with carbon ions in additional fractions.

(iii) A simultaneous carbon ion boost is prescribed for only a limited number of fractions.

The second method has been employed at GSI (Schulz-Ertner *et al.* 2004). Here, we are going to compare treatment plans of type (i) with a 30 fraction simultaneous photon (SIM–X) or carbon ion boost (SIM–30), of type (ii) with a six fraction sequential carbon ion boost (SEQ), and of type (iii) with a simultaneous carbon ion boost for 15 fractions (SIM–15). Fractionation schedules delivering a total RWD of 72 Gy (RBE) and 54 Gy (RBE) to the boost and the target, respectively, are listed in table 4.7.

4.2.1.2 Treatment plans

We investigated the potential of a simultaneous carbon ion boost in a phantom and several patient cases. For a feasibility study and an easier understanding of the observed effects we used a cylindrical water phantom with a C–shaped target molded around a cylindrical organ at risk in the center of the phantom (left column of figure 4.3). Inside the target volume a C–shaped boost volume was delineated. The phantom is irradiated with seven equidistant photon beams and two opposing carbon ion beams from incident gantry angles of 90° and 270°, respectively. Out of the several patient cases that were studied an exemplary case is presented here. A brain tumor is irradiated with an identical beam configuration as the phantom. The right column in figure 4.3 shows a representative CT slice of the patient with the contours of the target, the boost, and the brainstem. Target and boost dose prescriptions for both cases can be found in table 4.7.
Photon IMRT fields were simulated using a 6 MV linear accelerator equipped with an

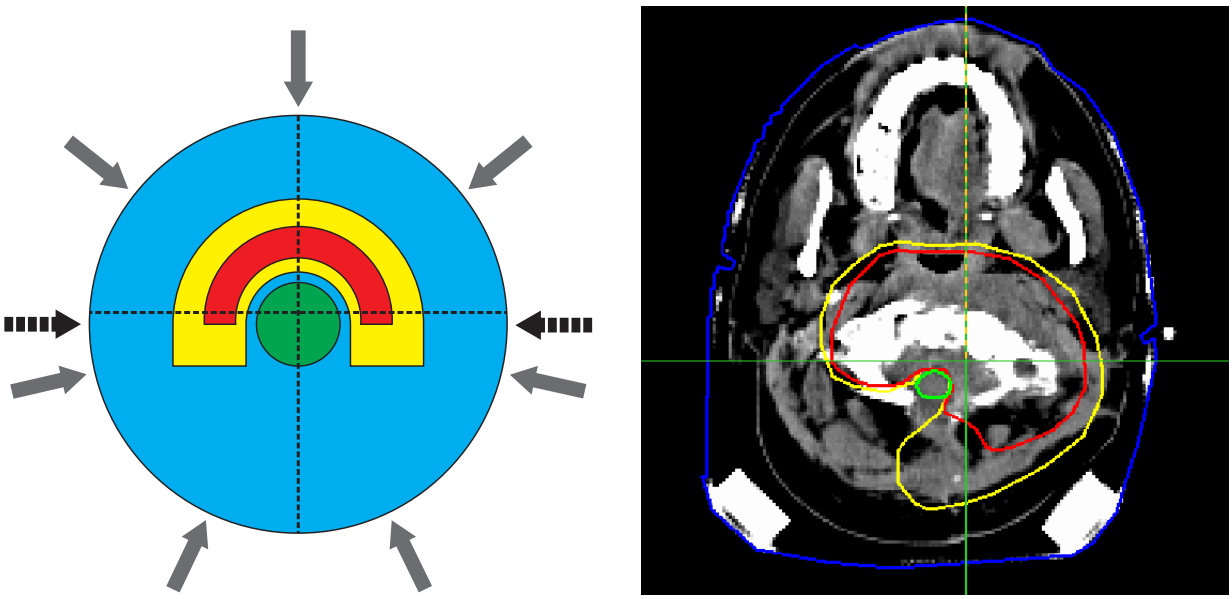

Figure 4.3: *Phantom (left) and patient case (right) studied in this section. In the water phantom the boost (red) is enclosed by the target (yellow) which is molded around the OAR (green). The patient CT slice shows a boost volume (red) and a target volume (yellow). The only organ at risk outlined in this CT slice is the brainstem (green). Gray and dashed black arrows represent incident beam directions for photons and carbon ions, respectively. The same directions were used for phantom and patient treatment plans*

MLC with 5 mm leaf width. The optimized photon fields were not sequenced. Carbon ion dosebursts are laterally and longitudinally spaced with 3 mm distance.

4.2.2 Results

4.2.2.1 Convergence performance of a simultaneous boost treatment plan

It turned out that the standard optimization with starting weights of zero and its preset convergence criterion i.e. 5 iterations with less than 0.1 % change of the objective function value, will not return an acceptable solution for a SIM–30 or SIM–15 treatment plan. The optimizer returns a solution using only dose from the carbon ion beams and no photon irradiation at all. Though the solution fulfills the planning constraints of the boost volume it completely fails in the target volume. If the convergence criterion is turned off the optimizer increases the carbon doseburst weights rapidly in the beginning followed by a large number of iteration with very small changes i.e. several dozen of iteration with less than 0.1 % change in the objective function value. In some cases the optimizer eventually begins to rise the weights of the photon dose bursts and will finally return an acceptable solution. In other cases it remains stuck in this unacceptable solution. As a representative

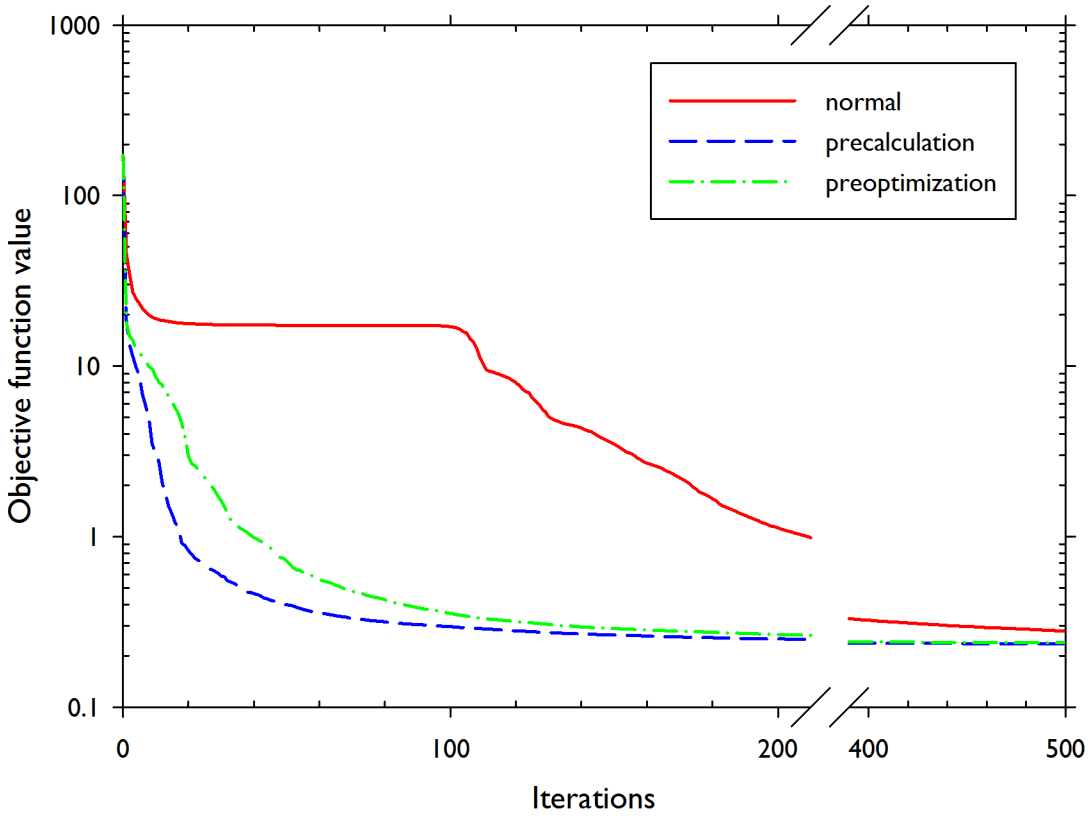

Figure 4.4: *The objective function value of the treatment plan with a simultaneous carbon ion boost for 30 fractions in the phantom depends on the initial solution.*

example figure 4.4 shows the objective function value as a function of the number of iterations for a simultaneous carbon ion boost in the phantom applied for all 30 fractions. In this example the objective function value is nearly constant for 65 fractions before the optimizer starts to use the photon beams. Both the preoptimization and the precalcualtion method generate starting solutions that ensure an acceptable solution found with less iterations. In the case of our example the preoptimized and the precalculated optimization fulfilled the termination criterion after 243 and 175 iterations, respectively. The objective function value of the preoptimized (precalculated) plan after 243 (175) iterations is ~ 63 % (~ 87 %) smaller than the regular optimization after the same number of iterations. After 500 iterations the objective function value of the regular optimization is still approximately 10 % larger than the termination value of both other methods.

Both methods generate starting solution of similar quality but they differ significantly in their time consumption. The preoptimization of the weights of the example presented in figure 4.4 took 679 s, the precalculation took 7.5 s. Due to this significant difference the

precalculation method was employed for all simultaneous optimizations of carbon ion and photon beams.

4.2.2.2 Comparison of the fraction schemes

The phantom

Figure 4.5 shows the DVHs of all four phantom treatment plans. Boost voxels were excluded from the target for DVH calculation. On a first glance only minor clinically relevant differences can be observed. Three general observations could be made:

- Any kind of carbon ion boost increased the homogeneity of the boost coverage.
- The SEQ plan received significantly more dose in the target than all other plans.
- The maximum OAR dose was also increased for the SEQ plan.

There is definitely an increase of the dose in the SEQ plans probably due to the separate optimization of two treatment plans that are later added up. For a better understanding of the observed effects figure 4.6 shows horizontal and vertical RWD profiles along the dashed lines in figure 4.3. Clearly, the additional target dose of the SEQ plan is deposited in the entrance channel of the carbon ion beams (panel a). Locally, the sum of the separately

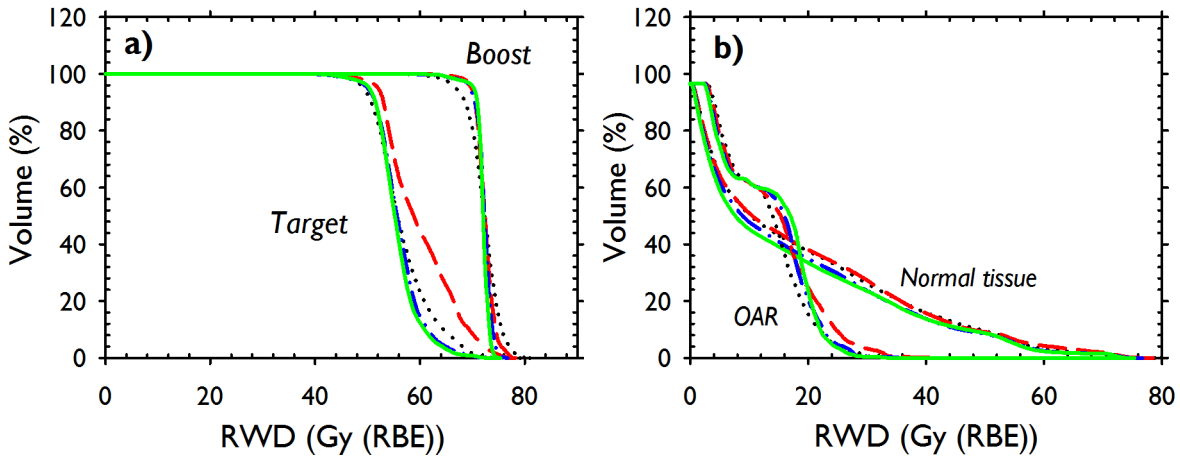

Figure 4.5: *Combined RWD DVHs of the SIM–X plan (dotted black), the SEQ plan (dashed red), the SIM–15 (dashed–dotted blue), and the SIM–30 (solid green) plan of the phantom. The target DVHs do not include the RWD of boost voxels.*

optimized treatment plans of the SEQ plan increases the RWD along the incident beam direction by 10 to 20 Gy (RBE) compared to the SIM–30 plan. There is literally no difference between target and boost dose in the carbon ion beam entrance channel for the

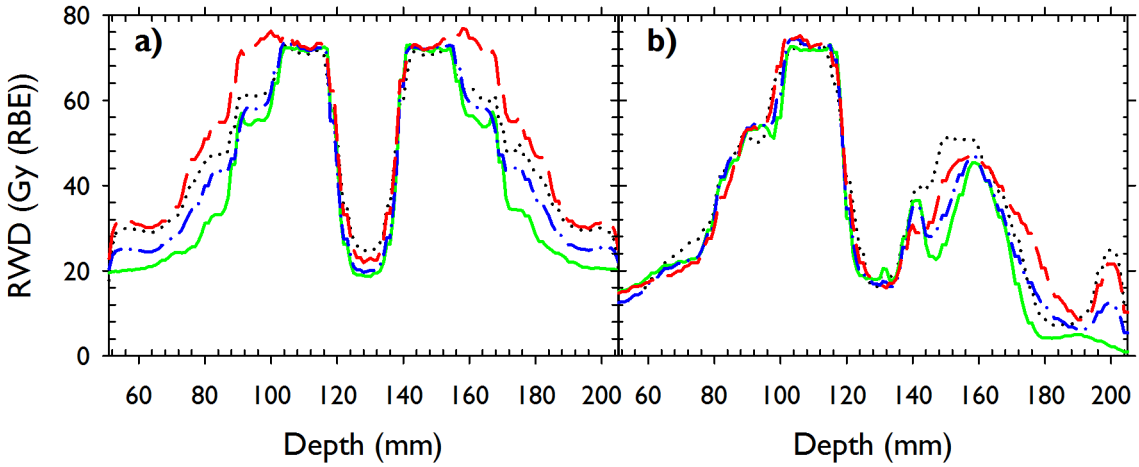

Figure 4.6: *Panels a) and b) are horizontal and vertical RWD profiles of the phantom's central CT slice, respectively. All four fractionation schemes are shown: The SIM–γ plan as dotted black line, the SEQ plan as dashed red line, the SIM–15 plan as dash–dotted blue line, and the SIM–30 plan as solid green line.*

SEQ plan. Perpendicular to this axis no significant difference is observed between SIM–30, SIM–15, and SEQ plan. The SIM–X plan shows an increased RWD in the lower half of the phantom which is caused by the need of shaping the boost with photon beams. The steepness of the RWD gradients towards the OAR does not differ among those plans using carbon ions.

In the introduction to this chapter we claimed that a simultaneous optimization of carbon ions and photons would allow to shape local dose gradients predominantly with carbon ions. Figure 4.7 shows single fraction dose and RWD profiles of the SIM–30 plan for each radiation modality. The RWD of the respective radiation modalities was calculated by multiplying their absorbed dose with the RBE of the total dose distribution. As expected, the maximum carbon ion doses are observed at the edges of the boost volume towards the OAR. In the horizontal profile (panel a) the maximum carbon RWD is only ~ 0.4 Gy (RBE), less than the 0.6 Gy (RBE) difference between prescribed boost and target dose. Vertically (panel b) the maximum RWD is ~ 0.75 Gy (RBE), more than the difference between boost and target RWD. The gradient towards the OAR is shaped with the lateral dose gradient not with the distal.

It should be noted that due to the synergistic effects of radiation that are reflected in the β term of LQ–model (equation (2.13)) the RBE of photons is not unity when they irradiate the same voxel as carbon ions. As a side aspect, we can also observe the dose dependence of the RBE in figure 4.7 a). Though the carbon ion LET increases along the depth of the carbon ion beam the total RBE decreases which is due to the mixing of photon and carbon

ion doses. As a result the maximum RBE is observed in normal tissue, not in the target.

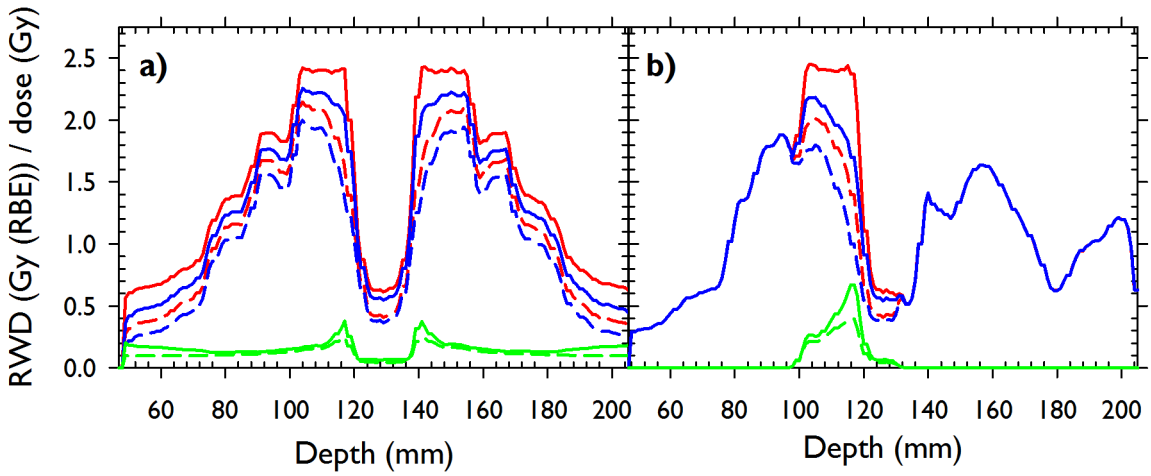

Figure 4.7: *Dose (dashed) and RWD (solid) profiles for a single fraction of the SIM–30 plan by radiation modality. Carbon ions (green) and photon (blue) doses add up to the total dose (red). Panels a) and b) are horizontal and vertical cuts through the phantom's central CT slice, respectively.*

The patient case

Figure 4.8 shows the DVHs of the four fractionation schemes applied to a representative patient case. Observations made when studying the phantom treatment plans are confirmed by these results. Again, all plans comprising carbon ions have a higher conformity of the boost RWD. In the case of the SEQ plan this comes at the cost of a significant increase in the target RWD due to the entrance dose of the carbon ion beams. Regarding the OAR dose it seems far fetched to make any general statements. We can only state that the SIM–30 plan has the lowest RWDs in any OAR. Those OARs not reported here sustained doses well below the critical limits.
There are no detailed results presented here showing the dose distributions of the treatment plans in depth as they are a mere repetition of the above results and do not add anything to the understanding of the simultaneous optimization.

4.2.3 Discussion and Conclusions

In this section we have presented a novel approach for the combination of carbon ion and photon irradiation. It is introduced as an alternative to a sequential carbon ion boost and has two major advantages. The photon to carbon ion dose is not fixed in each fraction

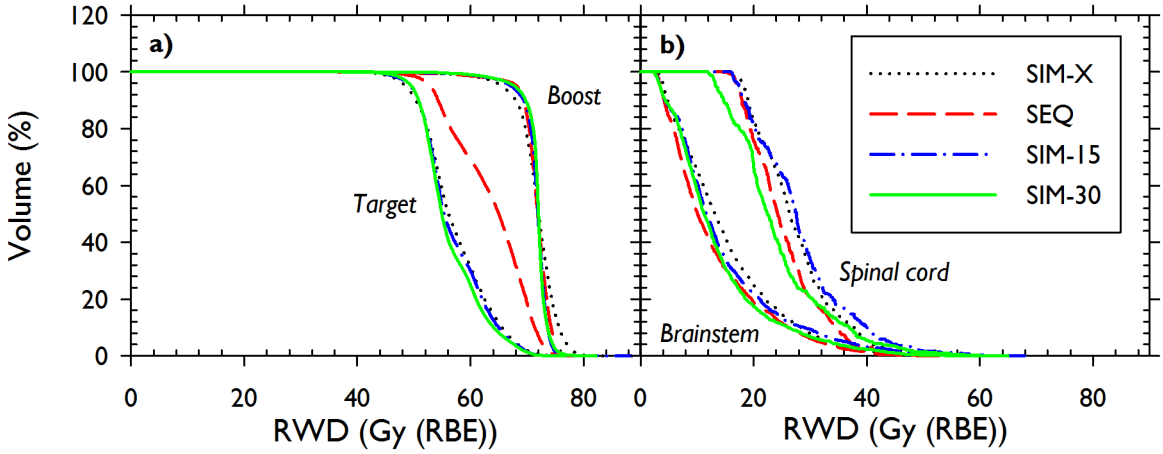

Figure 4.8: *Combined RWD DVHs of the SIM–X plan (dotted black), the SEQ plan (dashed red), the SIM–15 (dashed–dotted blue), and the SIM–30 (solid green) plan of an exemplary patient case. The target DVHs do not include the RWD of boost voxels.*

which allows the optimizer to use the carbon ion dose to shape steep dose gradients towards critical structures. Additionally, it is advantageous to optimize a single plan only and not having to optimize two plans as it is done for a sequential boost where the treatment planner has to go back and forth between the treatment plans to avoid hot spots. A very time consuming procedure that can only overcome the extra dose to target and normal tissue to a limited degree.

Still one has to be careful using a simultaneous carbon ion boost. If none homogeneous fields are applied it is critical that the patient is correctly positioned. In most situations a patient will have to be moved from one treatment room to another when treated with two different modalities. At best he remains on the same couch and in the same position. If the patient has to be repositioned for the second radiation modality the chance of misalignment is not to be neglected. In a mixed field approach slight changes in the position may easily lead to areas of over– and underdosage.

The major advantage of the simultaneous to the sequential boost seems to be that the optimization of both modalities is performed simultaneously and we are automatically compensating for additional doses. Obviously this could be overcome if the sequential boost and the photon treatment plan are optimized simultaneously. While this sounds relatively simple in the first place it is actually very challenging. Currently we are prescribing a fixed RWD $\bar{D}_{\text{biol}}$ or biological effect for N_{frac} fractions and the treatment planning system is optimizing the RWD or effect per fraction. If the sequential boost shall be optimized simultaneously we would not only have to optimize the total RWD or biological effect. Let's

assume a target voxel receives an extra dose due to the sequential boost of 12 Gy (RBE) in 6 fractions. If we now reduce the target dose in the entrance channel by 0.4 Gy (RBE) per fraction the total RWD is the same, but the total biological effect is different. Assuming chordoma tissue the total effect due to carbon and photon dose is $\mathcal{E} = 9.54$ while it is 10.26 for 30 photon fractions of 1.8 Gy. To keep the effect constant a photon fraction dose of 1.5 Gy would have to be applied with the sequential carbon ion boost. This calculation has to be repeated for every voxel. Hence, the total RWD distribution in the target would be inhomogeneous though the biological effect is constant. One way out of this dilemma is the use of biological effective doses (BED) which are defined by

$$BED\left(d, N_{\text{frac}}\right) = N_{\text{frac}} \cdot \frac{\mathcal{E}\left(d\right)}{\alpha} = D\left(1 + \frac{d}{\alpha/\beta}\right) \tag{4.1}$$

where d is the dose per fraction and $D = d \cdot N_{\text{frac}}$ is the total dose after N_{frac} fractions. This way the biological effect is expressed in a well known unit (Gy) and incorporates fractionation effects. BED solves the problem of displaying inhomogeneous doses but it does not provide any means on the splitting of doses among the radiation modalities. In some way or another it has to be decided that one of the modalities has to give a certain fraction dose and the other modality is used to fill the gap to the prescribed BED. A possible objective function that does not make a difference between under– and overdosage for a target voxel i in this scheme is

$$F_{i\notin\text{boost}}\left(\boldsymbol{w}\right) = \left[\bar{\mathcal{E}} - N_{\text{C}}\left(\sum_{j\in\text{C}}\alpha_{ij}D_{ij}w_j + \left(\sum_{j\in\text{C}}\sqrt{\beta_{ij}}D_{ij}w_j\right)^2\right) - N_{\text{X}}\left(\sum_{j\in\text{X}}\alpha_{ij}D_{ij}w_j + \left(\sum_{j\in\text{X}}\sqrt{\beta_{ij}}D_{ij}w_j\right)^2\right)\right]^2 \tag{4.2}$$

where N_{C} (N_{X}) is the number of carbon ion (photon) fractions and C (X) is the assemble of carbon ion (photon) dosebursts. A boost voxel i could be optimized using

$$F_{i\in\text{boost}}\left(\boldsymbol{w}\right) = \left[\bar{\mathcal{E}}_{\text{C}} - N_{\text{C}}\left(\sum_{j\in\text{C}}\alpha_{ij}D_{ij}w_j + \left(\sum_{j\in\text{C}}\sqrt{\beta_{ij}}D_{ij}w_j\right)^2\right)\right]^2 + \left[\bar{\mathcal{E}}_{\text{X}} - N_{\text{X}}\left(\sum_{j\in\text{X}}\alpha_{ij}D_{ij}w_j + \left(\sum_{j\in\text{X}}\sqrt{\beta_{ij}}D_{ij}w_j\right)^2\right)\right]^2 . \tag{4.3}$$

Here, the total prescribed boost effect is $\bar{\mathcal{E}}$, the effect supposed to be delivered by the carbon ion fractions $\bar{\mathcal{E}}_{\mathrm{C}}$ and $\bar{\mathcal{E}}_{\mathrm{X}} = \bar{\mathcal{E}} - \bar{\mathcal{E}}_{\mathrm{C}}$. The treatment planner looses control over the fractionation doses in the target and needs a lot of trust in the biological models.
In conclusion, simultaneous carbon ion boosts provide the potential of steeper dose gradients and reduced target and integral dose. The SIM–15 treatment plan seems to be a reasonable alternative to a SIM–30 plan as none of the planning objectives is compromised though the number of carbon ion fractions is reduced by a factor of two. It can be questioned if the simultaneously carbon ion boost can be applied in clinical routine due to the difficulty of positioning the patient correctly. Additionally, one can argue that most of the improvement from sequential to simultaneous boost is rather due to the simultaneous optimization than the variable carbon ion to photon dose ratio. It has to be investigated whether a simultaneously optimized sequential carbon ion boost is of similar treatment plan quality than a simultaneous boost.

4.3 Biological worst case optimization

The quality of a delivered 3D IMPT plan depends largely on accurate planning CTs and patient positioning. Throughout this work we made use of the highly localized dose depositions of particles and their steep lateral and distal gradients. In consequence, the optimization algorithms created treatment plans with individually inhomogeneous fields that rely on accurate superimposition to generate the desired dose distributions. A slight misalignment of the patient or an erroneous particle range could have large influences on the outcome (Lomax 2008). Multiple authors have developed methods to include potential errors into the optimization and reduce their impact (Unkelbach *et al.* 2007, Pflugfelder *et al.* 2008, Fredriksson *et al.* 2011). During the work on this thesis the worst case optimization by Pflugfelder *et al.* (2008) was adapted to optimize in addition to the absorbed dose also RBE–weighted absorbed dose distributions for protons and carbon ions. The methodology was applied to objective functions for the biological effect i.e. additionally to worst case dose cubes this method also requires worst case α or LET cubes, respectively.
In conventional radiotherapy with photons and particles range uncertainties and setup errors are accounted for by increasing the clinical target volume (CTV) to a planning target volume (PTV) following margin recipes (van Herk *et al.* 2000). According to a publication by van Herk *et al.* (2000) "the PTV is a geometrical concept, and it is defined to select appropriate beam sizes and beam arrangements, taking into consideration the net effect of all the possible geometrical variations and inaccuracies in order to ensure that the prescribed dose is actually absorbed in the PTV." A major assumption of the margin concept is that a shift of the patient does not significantly alter the shape of the dose distribution. This assumption is most likely not fulfilled for particle plans. Worst case optimization replaces the margin concept by intrinsically creating margins according to the expected errors. Additionally, the changing relative assembly of the beams is also taken into account.
In this section we will briefly review the worst case optimization and its implementation. The modified method was applied to several patient cases out of which one exemplary case irradiated with carbon ions will be presented here. We will compare the worst case to conventionally optimized treatment plans especially in regard to their capability of compensating errors. For these comparisons the conventional treatment plans were optimized with the PTV as planning target volume while the worst case optimization used only the CTV.

4.3.1 Methods

4.3.1.1 Worst case optimization

The aim of the worst case optimization is the simultaneous optimization of the nominal dose distribution and a worst case dose distribution. The objective function F_{wco} is defined as the weighted sum of the values of an objective function F evaluating the nominal dose distribution D_{nom} and the worst case dose distribution D_{wco}

$$F_{\text{wco}}(\boldsymbol{w}) = F(D_{\text{nom}}(\boldsymbol{w})) + p_{\text{wco}} F(D_{\text{wco}}(\boldsymbol{w})). \tag{4.4}$$

Here, p_{wco} is the worst case penalty weighting the influence of the worst case dose distribution. In this work we will be employing $p_{\text{wco}} = 1$. The objective function applied to the respective dose distributions in equation (4.4) is not specified and not restricted to a specific method. For physical and biological worst case optimization we could therefore employ the quadratic objective for the dose and the biological effect, respectively (cf. section 2.3.3).

The worst case dose distribution is defined as the worst dose that can be expected in a voxel i. In a practical implementation a set of test distributions has to be defined out of which the worst case is selected. Depending if a voxel belongs to a target volume or an OAR this can be the voxel's minimum or maximum dose in the test distributions. The voxelwise selection makes the worst case dose distribution unphysical but it serves well as a lower limit of the potential deviations of the nominal dose distributions. Which kind of error the worst case optimization compensates is solely depending on the test distributions. Pflugfelder *et al.* (2008) defined test distributions for three different scenarios:

(i) *Range uncertainties* have multiple possible sources both on the patient side and on the treatment planning side. Here, we are only going to consider the uncertainties of Hounsfield unit to stopping power conversion. The different errors all translate into a change of the range of the Bragg peaks. Hence, a spectrum of potential ranges has to be considered. In practical implementation it is sufficient to calculate additional dose distributions for the smallest and greatest range (Pflugfelder *et al.* 2008). It is assumed that the range uncertainties of all dose bursts with the same lateral position i.e. on the same ray (cf. gray lines in figure 2.5) are correlated. Therefore for each voxel the worst case of each ray has to be determined not for each dose burst. In terms of computational efficiency it has to be considered that this method requires two additional dose calculations that have to be performed and stored in additional D_{ij} matrices. In each iteration the worst case has to be determined for each ray.

(ii) *Setup uncertainties* are most likely due to a misaligned patient. Here, not only the shift of the voxels in each ray but in each field are correlated. It is again assumed that it is sufficient to account for the extreme shifts. If a positive and a negative shift are considered for each direction a total of six additional dose calculations has to be performed. Due to the correlation of all spots for each voxel the worst case can be determined by field which reduces the computational time in each iteration compared to the evalutation by ray.

(iii) *Combined range and setup uncertainties* are treated in the same way as setup uncertainties. Dose distributions are calculated for each extreme setup and range error i.e. eight in total. To reduce the complexity of the problem the worst case is evaluated by field.

In any of the above scenarios the required memory increases by the number of additional D_{ij}s that have to be stored. We will refer to WCO compensating for the range, setup, or both uncertainties as WCO–R, WCO–S, and WCO–RS, respectively.
The above description has so far only considered physical optimization. For carbon ions and to some extend also for protons it has to be extended to biological optimization This can be done by using the objective function for the biological effect and replacing test dose distributions by test biological effect distributions. Assuming that shifts in biological parameters and dose are correlated for each test dose distribution a corresponding α distribution has to be calculated. It is assumed that β is constant. After each iteration the worst case has to be determined from the test effect distributions and not the test dose distributions. In all other means the worst case optimization remains unchanged.

4.3.1.2 Treatment plan comparison

Dose distributions The biological WCO was tested on several patient cases with similar results. As an exemplary patient case a prostate carcinoma was selected. Figure 4.9 shows a representative CT slice of this case. The CTV was outlined and used as target volume for all worst case optimized treatment plans. For regularly optimized treatment plans a PTV was created by adding an isotropic margin of 7 mm as suggested by Rasch *et al.* (2005). The only organs at risk considered in this comparison are the bladder and the rectum. It was decided to use three beams to irradiate the patient with gantry angles 0°, 120°, and 240°. A 60 Gy (RBE) target RWD applied over 30 fractions was prescribed.
The aim of this study was a comparison of a regular plan with margins against a WCO plan in regard to their capability of coping with either range, setup, or combined uncertainties. Therefore we optimized four treatment plans: one regular plan and one for each of the worst

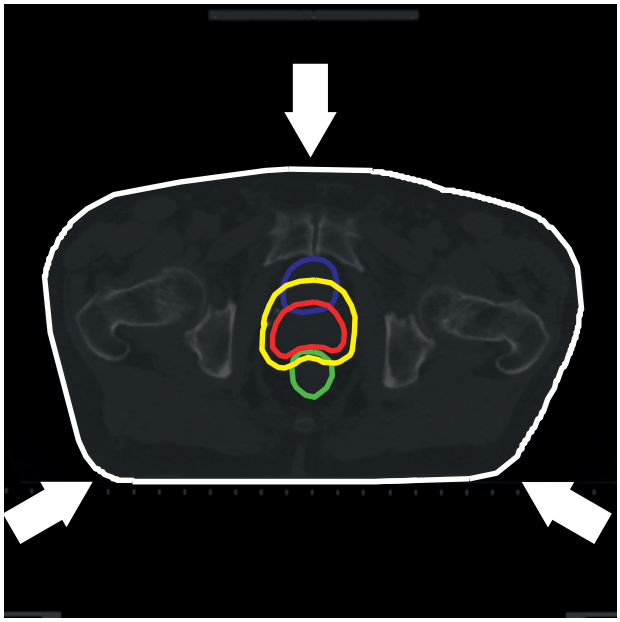

Figure 4.9: *A representative CT slice of the patient geometry. The CTV (red), the PTV (yellow), the rectum (green), and the bladder (blue) have been delineated. White arrows indicate gantry angles (*0°, 120°, 240°*) of the three beams.*

case scenarios. A comparison was performed as follows: Depending on the WCO mode we recalculated each treatment plan with 98 different range errors (RE–R), setup errors (RE–S), or combined errors (RE–RS). The regularly optimized plan was recalculated with each of the error sets for comparison. DVHs and dose–volume statistics (cf. section 2.3.4) were used to compare the results. Below is a description of the uncertainties that were used in the WCO and the generation of the error cases by worst case scenario. The combined scenario is not listed independently as it is a combination of the other two.

Range Uncertainties that were considered in the first scenario are assumed to be completely due to Hounsfield unit to stopping power conversion errors. Schaffner and Pedroni (1998) report that in soft tissue and bone the water equivalent proton range is afflicted with an error of ±1.1 % and ±1.8 %, respectively. As the worst case optimization in *KonRad* can only handle a single relative range error value we assumed that all ranges are afflicted with an error of ±1.8 %. Hounsfield unit (HU) is the unit of the greyscale value CT in a CT voxel. They are defined as the attenuation μ of the CT beam in the respective voxel relative to the attenuation $\mu_{\mathrm{H_2O}}$ of water

$$CT = \frac{\mu - \mu_{\mathrm{H_2O}}}{\mu_{\mathrm{H_2O}} - \mu_{\mathrm{air}}} \cdot 1000\ \mathrm{HU}, \tag{4.5}$$

Table 4.8: *Random and systematic patient positioning errors extracted from Rasch et al. (2005). The total error is the squared sum of the random and the systematic error.*

Direction	Random	Systematic	Total
Left–right	2.7 mm	2.1 mm	3.4 mm
Cranial–caudal	2.3 mm	2.8 mm	3.6 mm
Anterior–posterior	3.3 mm	3.6 mm	4.9 mm

where μ_{air} is the attenuation coefficient of air. We assume that the error in the range calculation is usually given as a relative error $\Delta\mu/\mu$ of the attenuation coeffient. This translates into an error ΔCT in the absolute CT value of

$$\Delta CT = \left(CT + 1000 \cdot \frac{\mu_{\text{H2O}}}{\mu_{\text{H}_2\text{O}} - \mu_{\text{air}}} \right) \frac{\Delta\mu}{\mu}. \tag{4.6}$$

If we assume that air does not attenuate the beam ($\mu_{\text{air}} = 0$) equation (4.6) is simplified to

$$\Delta CT = (CT + 1000) \frac{\Delta\mu}{\mu}. \tag{4.7}$$

This latter equation has been used to modulate errors in HU to stopping power conversion error. The 98 scenarios were created by assuming that the actual $\Delta\mu/\mu$ is normally distributed about 0 with a $\sigma = 1.8$ %.

Setup uncertainties that are considered in the second scenario translate simply into shifts of the patient isocenter. Rotation of the patient is not considered. Rasch *et al.* (2005) published an analysis of random and systematic patient positioning errors for prostate patients. The squared sum of random and systematic errors is assumed to be the width of a normal error distribution about 0 which was used to generate the error cases. The worst case optimization assumes that the setup uncertainties are isotropic. To cover all errors we used a setup error of 4.9 mm in the optimization.

4.3.2 Results

4.3.2.1 Evaluation of optimized plans

All treatment plans were optimized with the same penalty factors. A representative CT slice with its RWD distribution of all four plans is shown in figure 4.10. Additionally, figure 4.11 shows the dose, α, and RBE distribution of the same slice for the regular, the

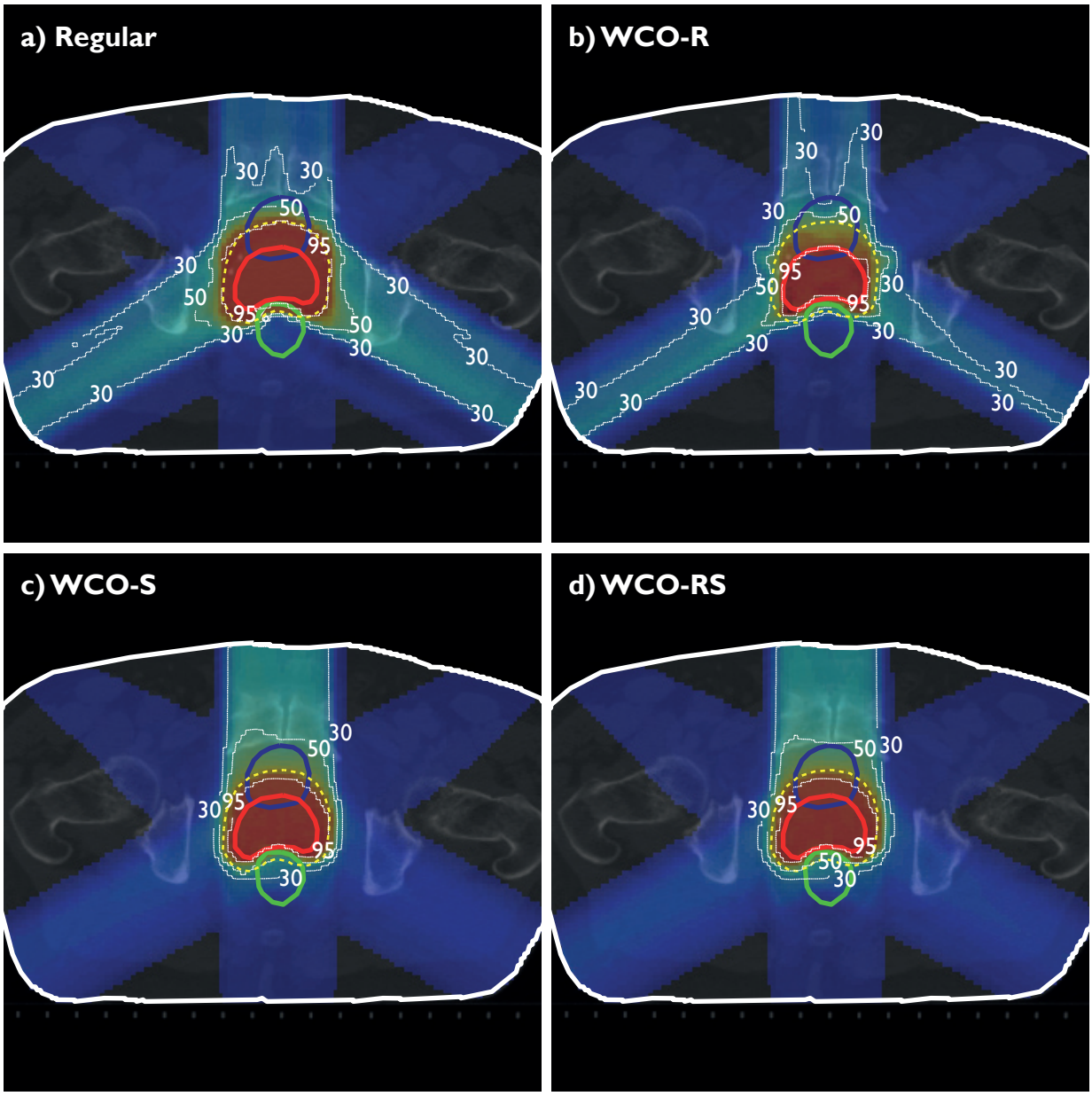

Figure 4.10: *Comparison of a conventionally optimized treatment plan (panel a) and worst case optimized plans correcting for a range error of 1.8 % (panel b), a setup error of 4.9 mm (panel c), and combined range and setup errors of 1.8 % and 4.9 mm (panel d), respectively. Isodose lines are given as percentage of the prescribed RWD.*

WCO–R, and the WCO–S plan. Due to the similarity of the WCO–S and the WCO–RS plan we refrain from showing details for this plan. The color coding for all panels showing the same unit was normalized to the same value. A brief comparison of the four RWD distributions shows that all treatment plans provide a similar CTV coverage. The extend to which the high RWD volume (95 % of the prescribed RWD) exceeds the CTV differs significantly. Figure 4.11 shows that the highest α values are always a the distal edge of the anterior field, within or close to the CTV. The largest RBE values are observed in those regions that receive predominantly fragment dose. Detailed descriptions for each treatment plan follow below.

Regular optimization The homogeneous high RWD region of the regular plan (figure 4.10 a) covers as intended the full PTV. Dose gradients at the edge of the PTV especially towards the rectum are shaped with distal field gradients. The α values in these regions are especially large. A local RBE minimum is found in the center of the CTV and a local RBE maximum in the rectum outside the PTV. The highest RBE values are observed in fragment tails were the dose is very low and α large.

WCO–R The high RWD volume is nearly identical with the CTV and the color coding of the incident beams suggests that most gradients are now shaped with lateral gradients that are invariant under range changes. In consequence, the maximum α values are smallest for this plan. Instead of using lateral gradients the optimizer could have also compensated range uncertainties by adding a margin at the distal edge of each field. The necessary margin of approximately 4.8 mm (1.8 % of 26.5 cm i.e. the depth of distal edge of the posterior fields) cannot be observed. The overshooting fragment tail of the 0° gantry angle beam is significantly shorter compared to the regular plan where it crosses through the rectum. Due to the low dose in the rectum the WCO–R exhibits the highest RBE in the rectum and there are two local RBE minima within the CTV.

WCO–S The dose is deposited by three homogeneous fields with the high RWD region exceeding the CTV but not all the way across the PTV. The 0° gantry angle beam delivers significantly more dose than the other two. It is the beam that is least affected by a shifted isocenter. A lateral shift of this beam in any direction has the least impact on any OAR: the rectum's position exceeds the beam range and the bladder is anyway completely within the beams entrance channel. As long as the anterior field is homogeneous a lateral shift should not alter the dose in the bladder. Dose and α distribution support the previous findings. High α values at the border of CTV and rectum indicate that here the RWD gradient is

shaped with the distal field gradient. The RBE of the WCO–S is very homogeneous but also lower in the target than anywhere else.

WCO–RS The RWD of the WCO–RS plan is shown in panel d) of figure 4.10. The uncertainty in the patient setup is dominating the range uncertainty and hence panels c) and d) look very much alike. Only the slight range difference of the fragment tail of the 0° gantry angle beam shows that the range errors are also accounted for.

4.3.2.2 Sensitivity of WCO and margin plans to errors

Range uncertainties Figure 4.12 a) and b) show the DVHs of the regular and the WCO–R plan, respectively. Underlying in grey are the DVHs of the 98 recalculated plans. While the CTV coverage of the regular plan is superior it is also sufficient for the WCO–R plan but at a significantly reduced integral and rectum RWD. The latter is not astonishing as the PTV partly overlaps with the rectum. How different the underlying dose distributions are becomes apparent when we compare the recalculated plans. The WCO–R plan is significantly less sensitive to range uncertainties than the regular optimized plans. In table 4.9 these visual observations are supported by numbers. The dose–volume statistics of the nominal CTVs are very similar. Large deviations are only observed in the inhomogeneity coefficients. Both organs at risk benefit from the WCO as the margins of the CTV are drastically smaller. The recalculated plans show that the worst case optimization reduces the impact of range errors to a greater extend than margins. Smaller standard deviations also indicate a reduced risks of unexpected overdoses for WCO–R plans due to falsely determined ranges.

Setup uncertainties Figure 4.12 shows the DVHs of the regular optimized plan in panel c) and the setup error compensating worst case plan in panel d). Corresponding dose–volume statistics can be found in table 4.9. Visually we already observed a considerable margin around the CTV when compensating for setup instead of range uncertainties. This is also reflected in an increased RWD in bladder and rectum. The DVHs already show that the WCO–S compensates significantly better for setup uncertainties than simple margins. Disregarding a few extreme cases the worst case optimization ensures that on average the dose distributions are well within the prescribed bounds and at the same time the dose to the OARs is significantly reduced. Performing the WCO–S with an increased setup error of 7 mm did not yield any major improvements. Both in the nominal plan and in the recalculated plans we observed a similar target coverage as with a margin of 4.5 mm but at the cost of a higher RWD in bladder and rectum (results not shown here). It is noteworthy

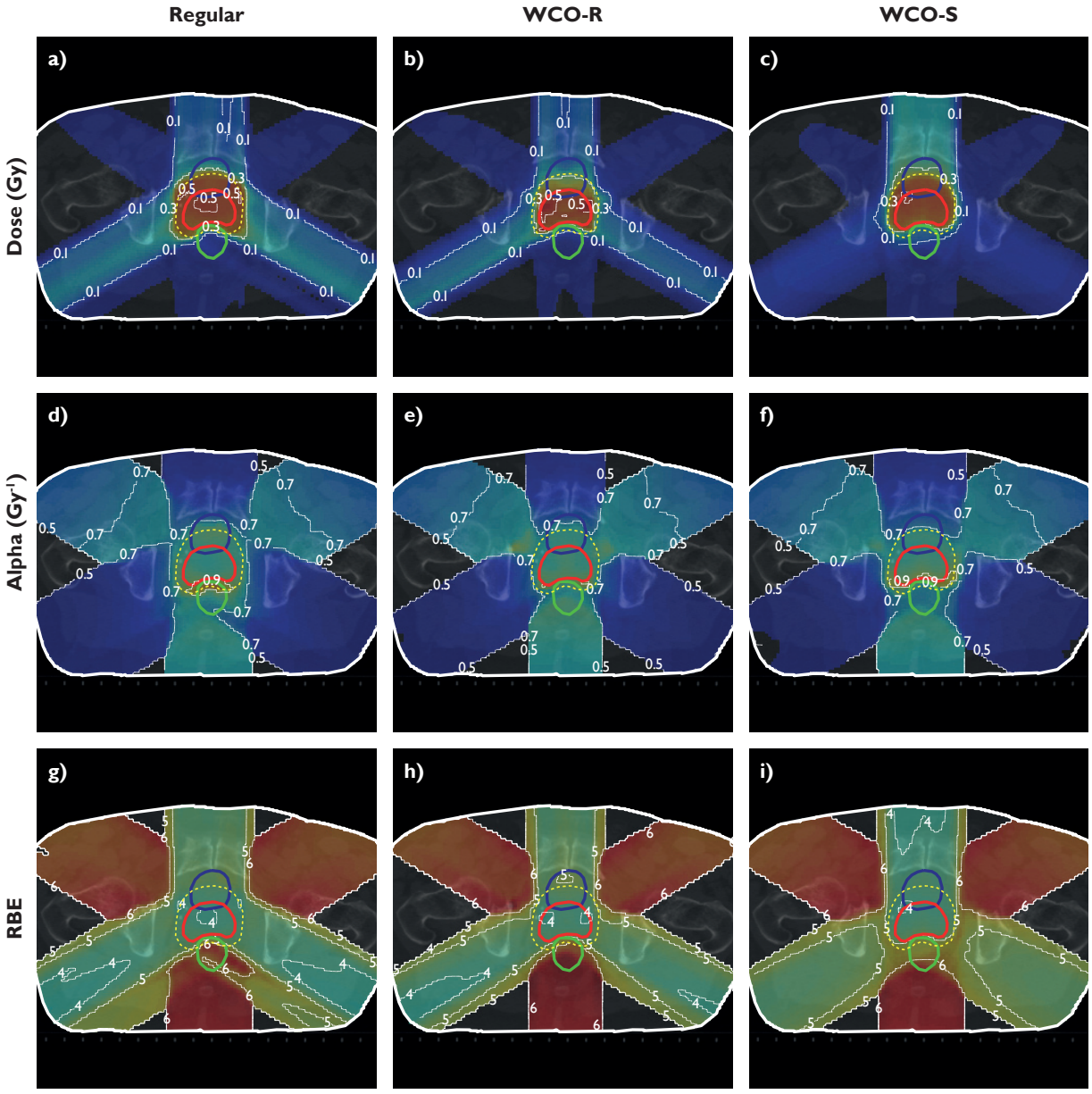

Figure 4.11: *Dose, α, and the RBE of the regular, the WCO–R, and the WCO–S plan. The colormap ranging from blue (small values) to red (large values) was normalized in each row to the same value.*

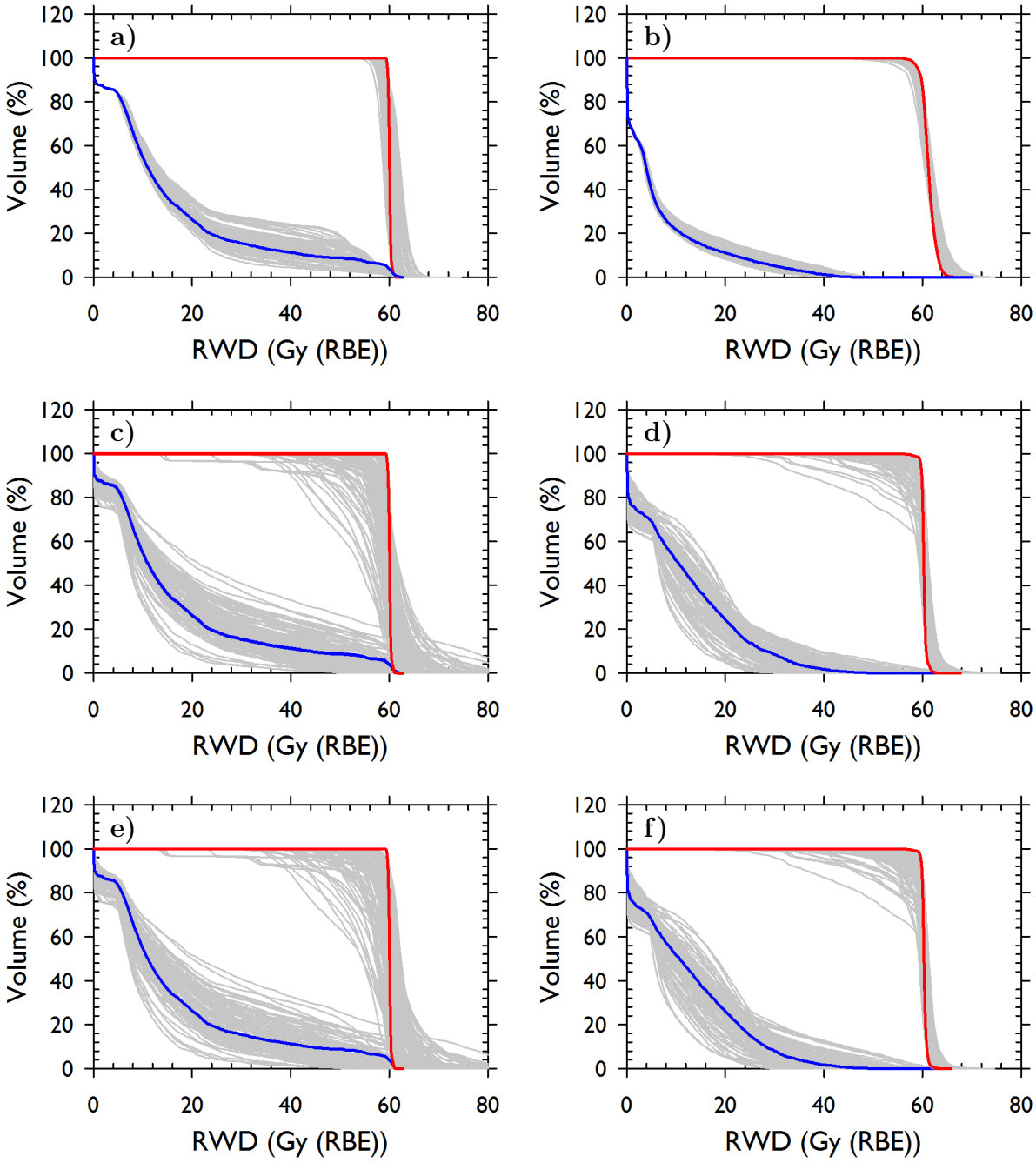

Figure 4.12: *DVHs of a regular plan (left column) and worst case optimized plans (right column). The nominal plans are shown in red (CTV) and blue (rectum). WCO in panels b), d), and f) compensated for range, setup, and both uncertainties, respectively. Each nominal plan was recalculated with varying errors. Errors applied to both plans in a row are those the respective worst case optimization compensated for. The nominal treatment plan in the left column is the same across all rows.*

that WCO–S has reduced inhomogeneity coefficients compared to WCO–R though they are still larger than those of regular optimized plan.

Combined uncertainties A first visual comparison of the dose distribution of the WCO–S and WCO–RS plans already showed that they are very similar. The DVHs (figure 4.12 panels e) and f)) and dose–volume statistics (table 4.9) support this finding. Visually it is difficult to determine differences between the WCO–S and WCO–RS plan. It is also difficult to determine differences among the recalculated plans. Both the recalculated regularly optimized DVHs and the recalculated WCO–RS DVHs look very much like those that were only subject to setup errors. It does seem like setup errors dominated the range errors in our configuration. Hence, our observations for the WCO–RS plan and the RE–RS distributions coincide with those for setup errors. An increased setup error of 7 mm did also not improve the results of the WCO–RS.

4.3.3 Discussion and Conclusions

We have extended the WCO to biological optimization modes. It is now possible to optimize the biological effect of protons and carbon ions under consideration of range, setup, and combined range and setup uncertainties. The ability of WCO to ensure ample target dose under various error scenarios was compared to the margin concept. It could be shown that for carbon ion IMPT both the range and setup errors are significantly better compensated by WCO than by margins. The results indicate that the margin concept is not applicable for particles.

4.3.3.1 Optimized plans

Though this is not a new result it is probably most striking that the current biological model predicts significantly lower RBEs in the target region than everywhere else (Wilkens and Oelfke 2008). For some combinations the RBE is even larger in the entrance channels of the beams than in the target. The more beams are used the worse is the relation of target to normal tissue RBE. Clearly, the effect of an increasing α value is lower than that of a low dose i.e. it is not the biological effectiveness that creates good carbon ion plans but only the good peak–to–entrance ratio of a carbon ion peak. The dose deposition actually has to compensate the RBE.
Biological and physical WCO (Pflugfelder *et al.* 2008) give very similar RWD distributions. The underlying dose and α distributions were as expected.

Table 4.9: *Selected dose–volume statistics of a regular (regular opt.) and three WCO plans compensating for range (WCO–R), setup (WCO–S), and both uncertainties (WCO–RS), respectively. Statistics are shown for each nominal plan (nom.) and the average and standard deviation of 98 recalculated plan. The recalculation was subject to varying range (RE–R), setup (RE–S), or both errors (RE–RS).*

	Regular opt.		WCO–R		Regular opt.	WCO–S		Regular opt.	WCO–RS	
	nom.	RE–R	nom.	RE–R	RE–S	nom.	RE–S	RE–RS	nom.	RE–RS
CTV										
D_{mean}	60.0	60.2 ± 0.7	61.2	61.2 ± 0.4	59.4 ± 2.3	60.2	60.1 ± 1.0	59.2 ± 2.3	60.3	59.9 ± 1.0
V_{95}	100.0	99.6 ± 1.1	99.3	98.4 ± 1.2	85.2 ± 16.8	99.6	93.6 ± 6.8	83.5 ± 16.7	99.7	92.8 ± 7.1
V_{99}	99.5	83.7 ± 20.2	93.1	89.5 ± 5.3	64.6 ± 23.3	97.6	85.0 ± 10.6	59.5 ± 23.1	97.9	83.7 ± 10.4
I_1	0.03	0.06 ± 0.04	0.12	0.15 ± 0.03	0.28 ± 0.18	0.06	0.24 ± 0.13	0.30 ± 0.18	0.05	0.24 ± 0.13
I_5	0.01	0.04 ± 0.02	0.07	0.09 ± 0.02	0.18 ± 0.12	0.02	0.12 ± 0.10	0.19 ± 0.12	0.02	0.12 ± 0.10
Bladder										
D_1	60.8	61.4 ± 1.61	58.8	58.7 ± 0.2	62.0 ± 3.92	59.7	58.7 ± 3.2	61.8 ± 3.99	59.7	58.8 ± 3.2
D_5	59.4	59.3 ± 1.26	33.4	33.1 ± 0.7	55.3 ± 8.60	53.8	50.4 ± 9.4	55.0 ± 8.89	53.9	50.4 ± 9.5
D_{mean}	10.7	10.8 ± 0.40	4.8	4.8 ± 0.0	11.8 ± 4.50	9.5	10.4 ± 4.0	11.8 ± 4.50	9.4	10.3 ± 4.0
Rectum										
D_1	61.1	60.8 ± 0.84	41.0	40.6 ± 2.9	59.4 ± 8.78	42.3	43.8 ± 8.5	58.8 ± 8.65	43.0	43.9 ± 8.9
D_5	59.4	56.3 ± 4.21	30.5	30.2 ± 3.3	52.3 ± 10.33	33.6	33.9 ± 6.9	50.7 ± 10.34	33.3	35.1 ± 8.0
D_{mean}	16.5	17.0 ± 1.81	7.1	7.1 ± 0.7	17.5 ± 3.63	12.4	12.2 ± 1.9	17.2 ± 3.77	12.6	12.6 ± 2.1

4.3.3.2 Sensitivity analysis

The sensitivity analysis showed that the worst case optimization is superior to the margin concept for both tested uncertainties. From the point of target coverage and OAR dose the WCO–R plan is nominally favorable to all other plans. This would also be beneficial in regard to time and memory constraints. But we have severe doubts that it withstands even small setup uncertainties. This should be tested in a future project. The WCO-S and WCO–RS plan on the other hand seem to be very robust in all regards. It should be studied if a WCO–S by itself is also insensitive to range uncertainties which would reduce the computational and time effort. For the WCO–S and WCO–RS plan we tested the two different setup errors and concluded that considering larger setup uncertainties does not necessarily result in more robust plans. In a future investigation the necessary error values should be studied.

Chapter 5

Accessing the Beam Quality: Analytical Dose and LET Models for Fragmenting Ion Beams

The quantification of the biological properties of an ion beam is difficult and physical measures of beam quality are required. One of the most prominent and widely used measures is the LET (Wilkens and Oelfke 2003). The importance of LET calculations becomes apparent when we consider the change of heavy ion RBE with LET (Kraft 1987) or the change of the hypoxia reduction factor (HRF) with LET (Barendsen *et al.* 1966, Furusawa *et al.* 2000).

Analytical methods to calculate the energy deposition of ion beams by electromagentic interactions and thereby dose and LET have been known for decades (Bethe 1930). While analytical calculations for protons are straight forward, the situation for heavy ion beams is far more complicated as we not only have to consider the LET of the primary ions but also contributions from beam fragments created by inelastic nuclear interactions. They have a significant dose contribution (about 6% at the Bragg peak of a 200 MeV/u carbon ion beam (Gunzert-Marx *et al.* 2008)) but even more important their range exceeds that of the primary ions by up to a factor of 9 (tritium fragments vs. carbon–12 ions) which has to be considered in radiation therapy planning. Moreover, if in these regions also the biological effects shall be considered we need to quantify the beam quality by calculating the LET.

Now, why do we need additional analytical dose and LET models for fragments? The physics of primary ions and their secondary fragments is the same. In a given depth the dose or LET is the combined contribution of all the observed particles. The sole difference

between primary ions and fragments is the local energy spectrum. Primary ions are created at a single source, fragments have an infinite number of sources all along the path of the primary ions. Hence, for primary ions a single energy spectrum has to be considered while for fragments the energy spectra of all the sources have to be combined. And the contribution of all these spectra is what we are looking for.
In this section we present an analytical model to calculate the dose, the fluence, and both the dose–averaged LET ($\mathrm{LET_d}$) and track–averaged LET ($\mathrm{LET_t}$) of a fragmenting ion beam. First, we outline briefly how existing analytical models for proton dose calculation (Bortfeld 1997) and proton LET calculation (Wilkens and Oelfke 2003) can be adapted for primary heavy ions. Next, we develop an analytical model for the dose and LET of fragments based on a simple power law for the range of protons as a function of their energy (Wilson 1946). The model does not provide any means to calculate the magnitude of the respective fragmentation channels. This required input will be taken form Monte Carlo simulations. In order to get a first estimate on the $\mathrm{LET_d}$ in therapeutic applications we will take a look at two SOBP consisting of a single or two opposing fields respectively. Though the model was designed with carbon ion therapy in mind it is also applicable to other ion beams. All fragment calculations depend on the mass and the charge of the fragment. Therefore the term "fragment" refers to a specific isotope not all isotopes of an element.

5.1 From protons to primary heavy ions

In section 2.1 we have already introduced the basic definitions of dose and LET and a simple power law for the range of protons as a function of their kinetic energy (equation (2.5)). We already showed that in accordance with the Bethe–Bloch equation (Bethe 1930) the power law can be adapted for heavier ions of charge Z_{hi}, mass number A_{hi}, and kinetic energy E_{hi} by

$$R_{\mathrm{hi}} = \frac{A_{\mathrm{hi}}}{Z_{\mathrm{hi}}^2} k_{\mathrm{p}} \left(\frac{E_{\mathrm{hi}}}{A_{\mathrm{hi}}} \right)^p = k_{\mathrm{hi}} E_{\mathrm{hi}}^p \tag{5.1}$$

using $k_{\mathrm{hi}} = A_{\mathrm{hi}}^{1-p}/Z_{\mathrm{hi}}^2 \cdot k_{\mathrm{p}}$. The adapted power law allows to easily modify the analytical proton dose (Bortfeld 1997) and LET (Wilkens and Oelfke 2003) models such that they are valid for heavier primary ions.
It can be shown that the adapted straggling width $\sigma_{\mathrm{s,hi}}$ (Bortfeld 1997) for heavy ions is

given by

$$\sigma_{\mathrm{s,hi}} = \frac{1}{Z_{\mathrm{hi}}^{4/p-2} A_{\mathrm{hi}}^{2-2/p}} \frac{e^4 NZ}{4\pi\epsilon_0} p^2 \frac{k_{\mathrm{p}}^{2/p}}{3-2/p} R_{\mathrm{hi}}^{3-2/p}, \tag{5.2}$$

where NZ is the electron density of the irradiated matter, ϵ_0 the vacuum permittivity and e is the charge of the electron. A derivation of (5.2) can be found in appendix B.

5.2 From primary heavy ions to fragments

The analytical description for dose, fluence, and LET arising from a fragment of mass A_{f}, charge Z_{f}, and kinetic energy E_{f} produced from primary ions of mass A_{hi}, charge Z_{hi}, and kinetic energy E_{hi} were derived under the following assumptions:

- only remnants of primary ions are considered
- the kinetic energy per nucleon is conserved in the fragmentation process: $E_{\mathrm{hi}}/A_{\mathrm{hi}} = E_{\mathrm{f}}/A_{\mathrm{f}}$
- the additional fragmentation of fragments can be neglected
- the cross section of each respective fragmentation channel can be approximated by an energy independent constant.
- the attenuation of the primary beam is the source of fragments. Each fragmentation channel f has an associated attenuation coefficient μ_{hif}. The sum of the attenuation coefficients is the total attenuation coefficient μ_{hi}. If we assume a very simple attenuation model the fluence $\Phi_{\mathrm{hi}}(z)$ is

  $$\Phi_{\mathrm{hi}}(z) = \Phi_0 \mathrm{e}^{-\mu_{\mathrm{hi}} z} \approx (1 - \mu_{\mathrm{hi}} z)\, \Phi_0 = \left(1 - \sum_f \mu_{\mathrm{hif}} z\right) \Phi_0 \tag{5.3}$$

  Here, Φ_0 is the fluence of the primary particle beam. Therefore the production rate of a specific fragment isotope f is equal to the loss of primary ions in the specific fragmentation channel

  $$\left.\frac{\mathrm{d}\Phi_{\mathrm{hi}}(z)}{\mathrm{d}z}\right|_{\mathrm{hif}} \approx \mu_{\mathrm{hif}} \Phi_0. \tag{5.4}$$

Let's consider a heavy ion beam of range $R_{\mathrm{hi},0}$ from which a fragment is created at depth $z' < R_{\mathrm{hi},0}$. The remaining energy E_{hi} of the primary ion at z' is

$$E_{\mathrm{hi}}(z') = k_{\mathrm{hi}}^{-1/p} \left(R_{\mathrm{hi},0} - z'\right)^{1/p}. \tag{5.5}$$

The kinetic energy per nucleon is conserved in fragmentation. Therefore, the newly created fragment's kinetic energy is given by $E_{\mathrm{hi}}(z)' \cdot \frac{A_{\mathrm{f}}}{A_{\mathrm{hi}}}$. This energy translates into a range $R_{\mathrm{f},z'}$ given by

$$R_{\mathrm{f},z'} = \frac{A_{\mathrm{f}}}{Z_{\mathrm{f}}^2} \frac{Z_{\mathrm{hi}}^2}{A_{\mathrm{hi}}} \left(R_{\mathrm{hi},0} - z'\right) = \lambda_{\mathrm{f}}^{\mathrm{hi}} \left(R_{\mathrm{hi},0} - z'\right). \tag{5.6}$$

Here, $\lambda_{\mathrm{f}}^{\mathrm{hi}} = (A_{\mathrm{f}}/Z_{\mathrm{f}}^2) \cdot (Z_{\mathrm{hi}}^2/A_{\mathrm{hi}})$. If the rate at which fragments are created is described by equation (5.4) the fluence $\Phi_{\mathrm{f},z'}(z)$ is given by

$$\Phi_{\mathrm{f},z'}(z) = \begin{cases} 0 & \text{for } z < z' \text{ and } z > R_{\mathrm{f},z'} \\ \mu_{\mathrm{hif}} \Phi(0)\, \mathrm{d}z' & \text{for } z' < z < R_{\mathrm{f},z'} + z' \end{cases} \tag{5.7}$$

where $\mathrm{d}z'$ is an infinitesimal short distance around z'. Once a fragment is created it undergoes the same physical interactions as any other ion. Rearranging equation (5.1) we obtain an energy range relationship for fragments

$$E_{\mathrm{f},z'}(z) = k_{\mathrm{f}}^{-1/p} \left(\lambda_{\mathrm{f}}^{\mathrm{hi}} \left(R_{\mathrm{hi},0} - z'\right) - (z - z')\right)^{1/p} \tag{5.8}$$

where $k_{\mathrm{f}} = A_{\mathrm{f}}^{1-p}/Z_{\mathrm{f}}^2 \cdot k_{\mathrm{p}}$. Taking the derivative of equation (5.8) with respect to z yields the stopping power $S_{\mathrm{f},z'}$. The above set of equation enables us to determine the fluence, dose, $\mathrm{LET_t}$, and $\mathrm{LET_d}$ of fragments.

5.2.1 Monoenergetic fragments

For now we assume that all the fragments of the same isotope created at z' have the same kinetic energy. If we want to know the contribution of all the fragments of this isotope at another depth z we have to combine the contribution of all fragments that are present at that depth. Once those fragments have been determined, fluence and dose are simply the sum of the respective contributions while $\mathrm{LET_t}$ and $\mathrm{LET_d}$ are the either fluence or dose weighted average of all stopping powers. As there is an infinite number of depths at which fragments are created the sums will be carried over to integrals. The lower (z'_{low}) and upper (z'_{max}) integration limits are a function of z and can be determined using equation

(5.6). Two types of fragments with different integration limits can be distinguished by their relative stopping power. The first looses less energy ($\lambda_{\mathrm{f}}^{\mathrm{hi}} > 1$) and the second looses more energy ($\lambda_{\mathrm{f}}^{\mathrm{hi}} < 1$) per unit distance than primary ions of the same energy per nucleon. Let us first consider those fragments that have a smaller stopping power than the primary particles ($\lambda_{\mathrm{f}}^{\mathrm{hi}} > 1$). No matter in which depth z' these fragments are created their range exceeds the range of the primary particles in the same depth and they reach at least the depth $R_{\mathrm{hi},0}$:

$$R_{\mathrm{f}}(z') > R_{\mathrm{hi}}(z') \Longrightarrow R_{\mathrm{f}}(z') + z' > R_{\mathrm{hi}}(z') + z' = R_{\mathrm{hi},0} \tag{5.9}$$

Hence, in depths $z \leq R_{\mathrm{hi},0}$ all fragments that were already created in smaller depths contribute i.e. $z'_{\mathrm{low}} = 0$ and $z'_{\mathrm{max}} = z$. In depth exceeding $R_{\mathrm{hi},0}$ the fluence is reduced as some fragments come to rest. The maximum depth a fragment can reach decreases with the depth in which it is created as the primary particles loose more energy per nucleon per unit distance than the fragment. The fragments reaching the greatest depths are those created at $z'_{\mathrm{low}} = 0$ cm and therefore reaching all depths in which the fragment can be observed. The fragment with the lowest energy that still reaches $z > R_{\mathrm{hi},0}$ can be determined by equation (5.6)

$$z = R_{\mathrm{f},z'_{\mathrm{max}}} + z'_{\mathrm{max}} \Longrightarrow z'_{\mathrm{max}} = \frac{\lambda_{\mathrm{f}}^{\mathrm{hi}} R_{\mathrm{hi},0} - z}{\lambda_{\mathrm{f}}^{\mathrm{hi}} - 1}. \tag{5.10}$$

Next, we will consider those fragments that have a greater stopping power than the primary particles ($\lambda_{\mathrm{f}}^{\mathrm{hi}} < 1$). These fragments loose more energy per nucleon per unit distance than the primary ions. Hence, the smaller the depth in which a fragment is created the smaller the maximum depth it can reach. The first fragment stopping is the fragment created at $z' = 0$ cm. The maximum depth it reaches is $z = R_{\mathrm{f},0} = \lambda_{\mathrm{f}}^{\mathrm{hi}} R_{\mathrm{hi},0}$. In any smaller depth all fragments already created contribute i.e. $z'_{\mathrm{low}} = 0$ and $z'_{\mathrm{max}} = z$. In depths $z > \lambda_{\mathrm{f}}^{\mathrm{hi}} R_{\mathrm{hi},0}$ some fragments have already come to rest and do not contribute any more. The fragments with the lowest energy at $z > \lambda_{\mathrm{f}}^{\mathrm{hi}} R_{\mathrm{hi},0}$ are those created at

$$z'_{\mathrm{min}} = \frac{\lambda_{\mathrm{f}}^{\mathrm{hi}} R_{\mathrm{hi},0} - z}{\lambda_{\mathrm{f}}^{\mathrm{hi}} - 1}. \tag{5.11}$$

Any fragment created at a greater depth will contribute and therefore has to be considered ($z'_{\mathrm{max}} = z$). To conclude our reasoning we explicitly list the lower and upper integration limits:

i $\lambda_{\mathrm{f}}^{\mathrm{hi}} > 1$ and $z \leq R_{\mathrm{hi},0}$: $z'_{\mathrm{low}} = 0$ and $z'_{\mathrm{max}} = z$

ii $\lambda_{\mathrm{f}}^{\mathrm{hi}} > 1$ and $z > R_{\mathrm{hi},0}$: $z'_{\mathrm{low}} = 0$ and $z'_{\mathrm{max}} = \frac{\lambda_{\mathrm{f}}^{\mathrm{hi}} R_{\mathrm{hi},0} - z}{\lambda_{\mathrm{f}}^{\mathrm{hi}} - 1}$

iii $\lambda_{\mathrm{f}}^{\mathrm{hi}} < 1$ and $z \leq \lambda_{\mathrm{f}}^{\mathrm{hi}} R_{\mathrm{hi},0}$: $z'_{\mathrm{low}} = 0$ and $z'_{\mathrm{max}} = z$

iv $\lambda_{\mathrm{f}}^{\mathrm{hi}} < 1$ and $z > \lambda_{\mathrm{f}}^{\mathrm{hi}} R_{\mathrm{hi},0}$: $z'_{\mathrm{low}} = \frac{\lambda_{\mathrm{f}}^{\mathrm{hi}} R_{\mathrm{hi},0} - z}{\lambda_{\mathrm{f}}^{\mathrm{hi}} - 1}$ and $z'_{\mathrm{max}} = z$

Cases i) and iii) have the same limits. Therefore, we will present their results together. Following the above considerations the fluence $\widetilde{\Phi_{\mathrm{f}}}$ of a monoenergetic fragment is given by

$$\widetilde{\Phi_{\mathrm{f}}}(z) = \Phi_0 \mu_{\mathrm{hif}} \int_{z'_{\mathrm{low}}}^{z'_{\mathrm{max}}} \mathrm{d}z' = \frac{\Phi_0 \mu_{\mathrm{hif}}}{\lambda_{\mathrm{f}}^{\mathrm{hi}} - 1} \cdot \begin{cases} \left(\lambda_{\mathrm{f}}^{\mathrm{hi}} - 1\right) z & \text{i) \& iii)} \\ \lambda_{\mathrm{f}}^{\mathrm{hi}} R_{\mathrm{hi},0} - z & \text{ii)} \\ \lambda_{\mathrm{f}}^{\mathrm{hi}} \left(z - R_{\mathrm{hi},0}\right) & \text{iv).} \end{cases} \tag{5.12}$$

Next, we will take a look at the dose, $\mathrm{LET_t}$, and $\mathrm{LET_d}$ of monoenergetic fragments that are given by the following equations

$$\widetilde{D_{\mathrm{f}}}(z) = \frac{\Phi_0 \mu_0}{\rho} \int_{z'_{\mathrm{low}}}^{z'_{\mathrm{max}}} \mathrm{d}z' \; S_{\mathrm{f},z'}(z) \,. \tag{5.13}$$

$$\widetilde{LET_{\mathrm{t,f}}}(z) = \frac{\Phi_0 \mu_0 \int_{z'_{\mathrm{low}}}^{z'_{\mathrm{max}}} \mathrm{d}z' \; S_{\mathrm{f},z'}(z)}{\widetilde{\Phi_{\mathrm{f}}}(z)} \tag{5.14}$$

$$\widetilde{LET_{\mathrm{d,f}}}(z) = \frac{\int_{z'_{\mathrm{low}}}^{z'_{\mathrm{max}}} \mathrm{d}z' \; S^2{}_{\mathrm{f},z'}(z)}{\int_{z'_{\mathrm{low}}}^{z'_{\mathrm{max}}} \mathrm{d}z' \; S_{\mathrm{f},z'}(z)} \tag{5.15}$$

There are only two additional integrals that have to be solved. The solution of the first integral is

$$\int_{z'_{\mathrm{low}}}^{z'_{\mathrm{max}}} \mathrm{d}z' \; S_{\mathrm{f},z'}(z) = \tilde{S} \cdot \begin{cases} \left[\delta^{1/p} - \varepsilon^{1/p}\right] & \text{i) \& iii)} \\ \delta^{1/p} & \text{ii)} \\ -\varepsilon^{1/p} & \text{iv)} \end{cases} \tag{5.16}$$

Here, $\tilde{S} = A_{\mathrm{f}}/A_{\mathrm{hi}} \cdot E_{\mathrm{hi},0} / \left(\lambda_{\mathrm{f}}^{\mathrm{hi}} - 1\right)$, $\delta = 1 - z / \left(\lambda_{\mathrm{f}}^{\mathrm{hi}} R_{\mathrm{hi},0}\right)$ and $\varepsilon = 1 - z/R_{\mathrm{hi},0}$. In the same fashion we obtained

$$\int_{z'_{\mathrm{low}}}^{z'_{\mathrm{max}}} \mathrm{d}z' \; S^2{}_{\mathrm{f},z'}(z) = \frac{\lambda_{\mathrm{f}}^{\mathrm{hi}} - 1}{p\,(2-p)} \frac{\tilde{S}^2}{\lambda_{\mathrm{f}}^{\mathrm{hi}} R_{\mathrm{hi},0}} \cdot \begin{cases} \left[\delta^{2/p-1} - \varepsilon^{2/p-1}\right] & \text{i) \& iii)} \\ \delta^{2/p-1} & \text{ii)} \\ -\varepsilon^{2/p-1} & \text{iv)} \end{cases} \tag{5.17}$$

Calculation of dose, $\mathrm{LET_t}$, and $\mathrm{LET_d}$ can be done easily using the above equations.

5.2.2 Including an energy spectrum

In the previous section we assumed that all fragments created at z' have a) the same kinetic energy per nucleon and b) do not straggle. This is of course an unrealistic approach. The primary ions are not monoenergetic and the physical interactions of the fragments are of statistical nature. Following the approaches for protons and primary ions we will assume that fragments have a Gaussian energy spectrum. To keep the calculations simple the energy spectrum is translated into an equivalent depth spectrum $\varphi_z(\bar{z})$. Each energy is identified with a water equivalent depth $\bar{z}$ in which a monoenergetic ion would have the same energy.
Let us first consider only fragments created at z'. For these fragments equations (2.8) to (2.11) can be applied directly. As these integrals only represent intermediate steps we are not going to present any results here. We can follow the arguments from the previous section to combine the contribution from all fragments of a specific isotope following the same arguments as in the previous section. Total fluence Φ_f and dose D_f are given by

$$\Phi_\mathrm{f}(z) = \mu_\mathrm{f}\Phi_0 \int_{z'_\mathrm{low}}^{z'_\mathrm{max}} \mathrm{d}z' \int_{-\infty}^{R_{\mathrm{f},z'}+z'} \mathrm{d}\bar{z}\, \varphi_z(\bar{z}) \quad \text{and} \tag{5.18}$$

$$D_\mathrm{f}(z) = \frac{\mu_\mathrm{f}\Phi_0}{\rho} \int_{z'_\mathrm{low}}^{z'_\mathrm{max}} \mathrm{d}z' \int_{-\infty}^{R_{\mathrm{f},z'}+z'} \mathrm{d}\bar{z}\, S_{\mathrm{f},z'}(\bar{z})\, \varphi_z(\bar{z}) \tag{5.19}$$

$$= \frac{\mu_\mathrm{f}\Phi_0}{\rho} \langle S_\mathrm{f} \rangle_z \tag{5.20}$$

Here, the Gaussian depth spectrum

$$\varphi_z(\bar{z}) = 1/\left(\sqrt{2\pi}\sigma_\mathrm{f}\right) \exp\left(-\frac{(z-\bar{z})^2}{2\sigma_\mathrm{f}^2}\right) \tag{5.21}$$

about the mean depth z has been simplified by using the same width σ_f for all fragments in all depths. Comparison with numerical integration showed that the width due to straggling can be approximated with the straggling width $\sigma_{\mathrm{f,max}}$ (equation (5.2)) at depth $\lambda_\mathrm{f}^\mathrm{hi} R_{\mathrm{hi},0}$ (the maximum range of the longest reaching fragment) without loss of accuracy. Additional Gaussian spectra e.g. due to the energy spectrum of the primary particles can be incorporated by squared addition of the spectrum widths. Calculation of $\mathrm{LET_t}$ and $\mathrm{LET_d}$ is not as straight forward at first glance as there are two levels of averaging. Exemplary we

will show here which steps are necessary to calculate $\mathrm{LET_t}$. The first step is to calculate $\mathrm{LET_t}$ for a fragment created at z'

$$LET_{\mathrm{t,f},z'}(z) = \frac{\int_{-\infty}^{R_{\mathrm{f},z'}+z'} \mathrm{d}\bar{z}\; S_{\mathrm{f},z'}(\bar{z})\,\varphi_z(\bar{z})}{\int_{-\infty}^{R_{\mathrm{f},z'}+z'} \mathrm{d}\bar{z}\;\varphi_z(\bar{z})} \tag{5.22}$$

$$= \frac{\mu_{\mathrm{f}}\phi_0 \int_{-\infty}^{R_{\mathrm{f},z'}+z'} \mathrm{d}\bar{z}\; S_{\mathrm{f},z'}(\bar{z})\,\varphi_z(\bar{z})}{\Phi_{\mathrm{f},z'}(z)} \tag{5.23}$$

where $\Phi_{\mathrm{f},z'}$ is the fragment's fluence. Next we will have to repeat the averaging to combine all fragments of the same isotope

$$LET_{\mathrm{t,f}}(z) = \frac{\mu_F\Phi_0 \int_{z'_{\mathrm{low}}}^{z'_{\mathrm{max}}} \mathrm{d}z' LET_{\mathrm{t,F},z'}(z)\,\Phi_{\mathrm{f},z'}}{\Phi_{\mathrm{f}}(z)} \tag{5.24}$$

$$= \frac{\mu_F\Phi_0 \int_{z'_{\mathrm{low}}}^{z'_{\mathrm{max}}} \mathrm{d}z' \int_{-\infty}^{R_{\mathrm{f},z'}+z'} \mathrm{d}\bar{z}\; S_{\mathrm{f},z'}(\bar{z})\,\varphi_z(\bar{z})}{\Phi_{\mathrm{f}}(z)} \tag{5.25}$$

$$= \frac{\mu_F\Phi_0 \langle S_{\mathrm{f}}\rangle_z}{\Phi_{\mathrm{f}}(z)} \tag{5.26}$$

Hence, $\mathrm{LET_t}$ can be obtained using the same integrals used for dose and fluence. If the same method is applied to the $\mathrm{LET_d}$ the following equation is obtained

$$LET_{\mathrm{d,f}}(z) = \frac{\int_{z'_{\mathrm{low}}}^{z'_{\mathrm{max}}} \mathrm{d}z' \int_{-\infty}^{R_{\mathrm{f},z'}+z'} \mathrm{d}\bar{z}\; S^2{}_{\mathrm{f},z'}(\bar{z})\,\varphi_z(\bar{z})}{\int_{z'_{\mathrm{low}}}^{z'_{\mathrm{max}}} \mathrm{d}z' \int_{-\infty}^{R_{\mathrm{f},z'}+z'} \mathrm{d}\bar{z}\; S_{\mathrm{f},z'}(\bar{z})\,\varphi_z(\bar{z})} \tag{5.27}$$

$$= \frac{\langle S_{\mathrm{f}}^2\rangle_z}{\langle S_{\mathrm{f}}\rangle_z} \tag{5.28}$$

which reduces the total number of integrals that have to be calculated to three. For a detailed evaluation of the three integrals see appendix C. The solutions are presented below in terms of the parabolic cylinder function D_ν.

$$\Phi_{\mathrm{f}}(z) = \frac{\phi_0\mu_0}{\sqrt{2\pi}\left(1-\lambda_{\mathrm{f}}^{\mathrm{hi}}\right)} \begin{cases} \mathrm{e}^{-\xi^2/4}D_{-2}(\xi) - \mathrm{e}^{-\chi^2/4}D_{-2}(\chi) & \text{i) and iii)} \\ \sqrt{\pi}2^{-1/2} - \mathrm{e}^{-\chi^2/4}D_{-2}(\chi) & \text{ii)} \\ \mathrm{e}^{-\xi^2/4}D_{-2}(\xi) - \sqrt{\pi}2^{-1/2} & \text{iv).} \end{cases} \tag{5.29}$$

To shorten the displayed equation we introduced $\chi = \frac{z-\lambda_{\mathrm{f}}^{\mathrm{hi}} R_{\mathrm{hi},0}}{\sigma_{\mathrm{f,max}}}$, $\xi = \frac{\lambda_{\mathrm{f}}^{\mathrm{hi}}\left(z-R_{\mathrm{hi},0}\right)}{\sigma_{\mathrm{f,max}}}$.

$$\langle S_{\mathrm{f}} \rangle_z = \tilde{S}_1 \cdot \begin{cases} \mathrm{e}^{-\xi^2/4} D_{-1/p-1}(\xi) - \mathrm{e}^{-\chi^2/4} D_{-1/p-1}(\chi) & \text{i) and iii)} \\ \frac{\sqrt{\pi} 2^{-1/2p}}{\Gamma((p+1)/2p)} - \mathrm{e}^{-\chi^2/4} D_{-1/p-1}(\chi) & \text{ii)} \\ \mathrm{e}^{-\xi^2/4} D_{-1/p-1}(\xi) - \frac{\sqrt{\pi} 2^{-1/2p}}{\Gamma((p+1)/2p)} & \text{iv).} \end{cases} \tag{5.30}$$

where

$$\tilde{S}_1 = \frac{\sigma_{\mathrm{f,max}}^{1/p} \Gamma(1/p)}{\sqrt{2\pi} p k_{\mathrm{f}}^{1/p} \left(1-\lambda_{\mathrm{f}}^{\mathrm{hi}}\right)}. \tag{5.31}$$

and the third integral yields

$$\left\langle S_{\mathrm{f}}^2 \right\rangle_z = \tilde{S}_2 \cdot \begin{cases} \mathrm{e}^{-\xi^2/4} D_{-2/p}(\xi) - \mathrm{e}^{-\chi^2/4} D_{-2/p}(\chi) & \text{i) and iii)} \\ \frac{\sqrt{\pi} 2^{-1/p+1/2}}{\Gamma(1/p)} - \mathrm{e}^{-\chi^2/4} D_{-2/p}(\chi) & \text{ii)} \\ \mathrm{e}^{-\xi^2/4} D_{-2/p}(\xi) - \frac{\sqrt{\pi} 2^{-1/p+1/2}}{\Gamma(1/p)} & \text{iv).} \end{cases} \tag{5.32}$$

with

$$\tilde{S}_2 = \frac{\sigma_{\mathrm{f,max}}^{2/p-1} \Gamma(2/p-1)}{\sqrt{2\pi} p^2 k_{\mathrm{f}}^{2/p} \left(1-\lambda_{\mathrm{f}}^{\mathrm{hi}}\right)} \tag{5.33}$$

Using the solutions to the integrals dose, $\mathrm{LET_t}$, and $\mathrm{LET_d}$ can be easily calculated. We refrain from displaying the actual equations as this would be a mere repetition.

5.2.3 The contribution of each fragment isotope

The derived model allows to calculate fluence, dose, and LET for each fragment isotope. Which is fine as a theoretical model but what we are eventually interested in is the beam quality of the complete carbon beam. One of our major assumptions was energy invariance of the cross section for each fragmentation channel. Hence, we need only one relative fluence or dose value for each isotope and the primary ions to combine all contributions. We do not intend to develop a model for this but instead want to go back to already published dose distributions of fragment elements. Benitsch (2005) simulated depth dose curves for all fragment elements with $Z \leq 6$ in a therapeutic carbon ion beam. We combined up to three isotopes to match the Monte Carlo depth dose curves of each element as good as

possible. This gives us relative contributions to the total dose that we can use to calculate the total dose and LET of a fragmenting ion beam.

5.3 Results

All results presented in this section were obtained for a carbon ion beam with a residual range of 14.35 cm in water corresponding to an initial energy $E_{\mathrm{hi},0} \approx 265$ MeV/u. We chose this energy to be able to compare our results to previously published Monte Carlo simulations (Benitsch 2005).

5.3.1 Dose, $\mathrm{LET_d}$, and $\mathrm{LET_t}$ for the primary ion beam

To verify our dose calculation we compared the primary carbon ion dose predicted by our analytical model to results from Monte Carlo simulations (Benitsch 2005). The original model (Bortfeld 1997) does not provide any means to calculate the absorption coefficient μ_{hi} which we therefore fitted to the data. Similarly, the model includes already straggling but the energy spread of the primary beam due to the employed ripple filter (Weber and Kraft 1999) still had to be included. With an additional energy spread $\sigma_{\mathrm{ripple}} = 3.5$ mm and an absorption coefficient $\mu_{\mathrm{hi}} = 0.0215\ \mathrm{cm}^{-1}$ we did not observe any differences between analytical model and simulation (cf. figure 5.1a).

5.3.2 Dose, dose–, and track–averaged LET of fragments

When comparing the shape of both the depth dose and the $\mathrm{LET_d}$ curve of the different isotopes we observed that the shape of the curves is similar for all fragments. Figure 5.2 shows the straggling corrected dose and $\mathrm{LET_d}$ for two example fragments. All fragments express the maximum dose and a simultaneous steep rise in $\mathrm{LET_d}$ in the same isotope dependent depth $R_{\mathrm{f}}(D_{\max})$. The value of $R_{\mathrm{f}}(D_{\max})$ depends only on $\lambda_{\mathrm{f}}^{\mathrm{hi}}$ and is given by

$$R_{\mathrm{f}}(D_{\max}) = \begin{cases} R_{\mathrm{hi},0} & \text{if } \lambda_{\mathrm{f}}^{\mathrm{hi}} > 1 \text{ and} \\ \lambda_{\mathrm{f}}^{\mathrm{hi}} R_{\mathrm{hi},0} & \text{if } \lambda_{\mathrm{f}}^{\mathrm{hi}} < 1. \end{cases} \tag{5.34}$$

For each of the respective cases an example can be found in figure 5.2. Depth–dose and $\mathrm{LET_d}$ curves for beryllium–9 (figure 5.2a, $\lambda_{\mathrm{f}}^{\mathrm{hi}} = 1.69$) and carbon–11 (figure 5.2b, $\lambda_{\mathrm{f}}^{\mathrm{hi}} = 0.91$) are shown. Both the dose peak and the $\mathrm{LET_d}$ rise can be explained by the fragment's range. $R_{\mathrm{f}}(D_{\max})$ is the depth of the first Bragg peak of a fragment of this isotope where the dose rises steeply.

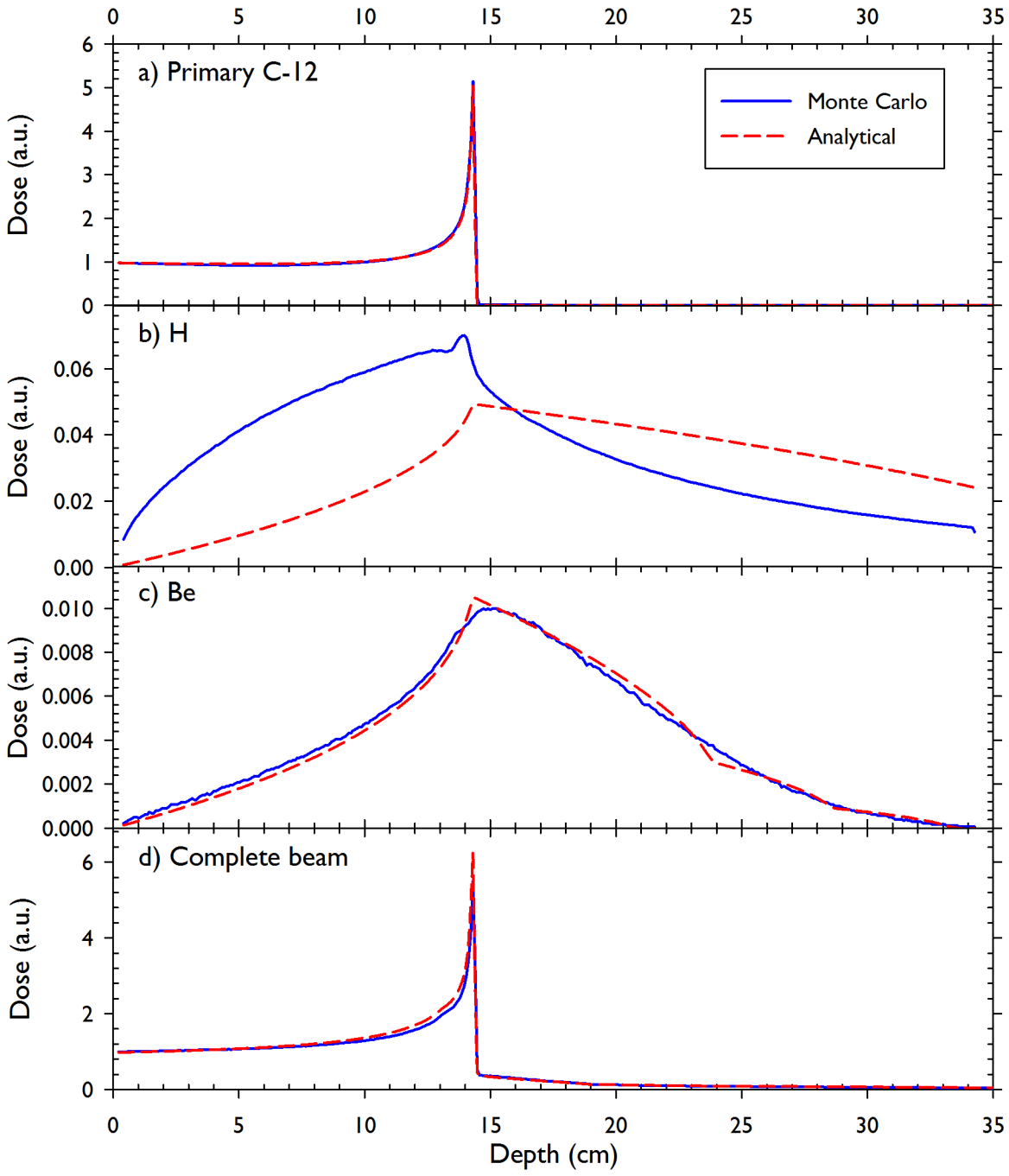

Figure 5.1: *Comparison of the dose of primary carbon ions, hydrogen fragments, beryllium fragments, and the total beam calculated with the analytical models and Monte Carlo simulations, respectively. All doses have been normalized to the entrance dose of the primary ions.*

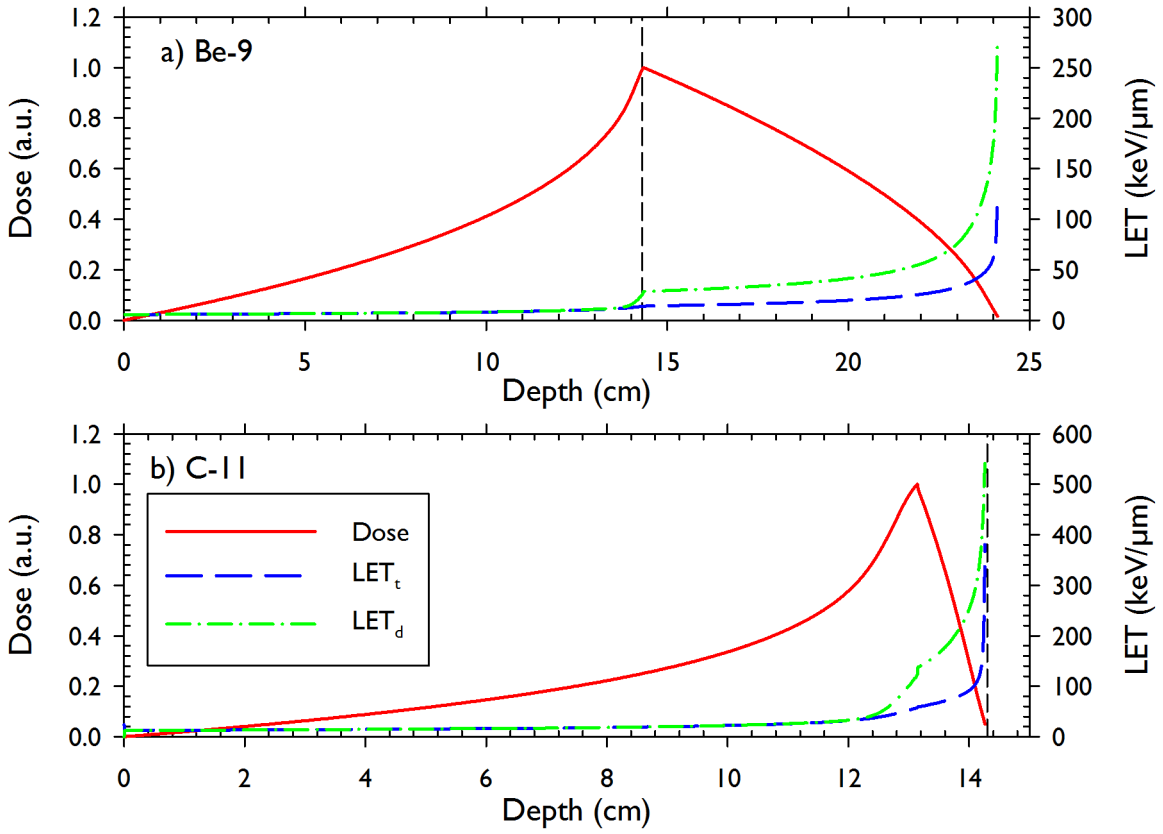

Figure 5.2: *Straggling corrected dose, LET_t, and LET_d of beryllium–9 and carbon–11. The Bragg peak of the primary ions is located at 14.35 cm (dashed black).*

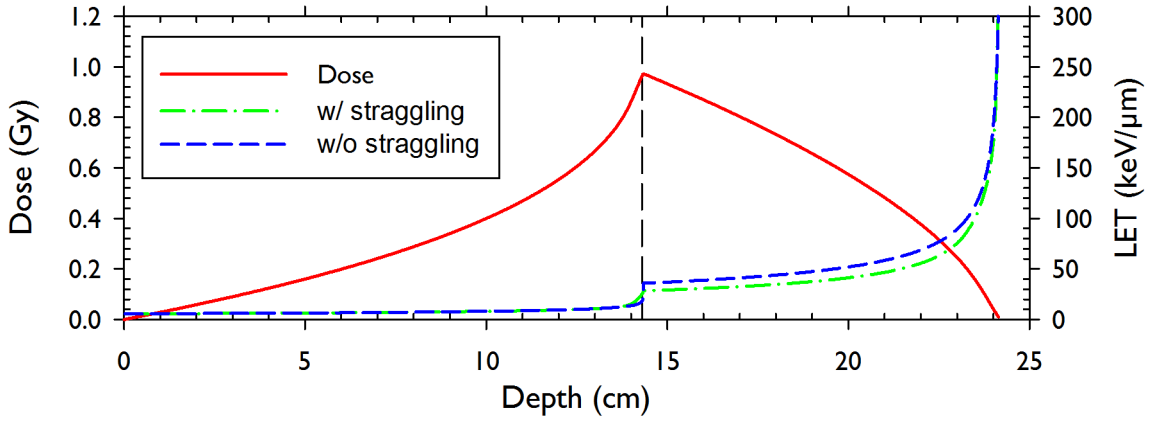

Figure 5.3: *LET_d and dose of beryllium–9 ions calculated with straggling and LET_d calculated without straggling. The range of the primary ions is highlighted by the dashed black line.*

Our calculations showed that the energy spectrum cannot be omitted when calculating $\mathrm{LET_d}$. Figure 5.3 shows $\mathrm{LET_d}$ predictions for beryllium–9 obtained with and without an energy spectrum. Up to $R_\mathrm{f}\,(D_\mathrm{max})$ the same values are predicted. Further into the water phantom the $\mathrm{LET_d}$ is significantly overestimated if straggling is omitted. The maximum value of the LET has to be considered carefully. The fluence is very small in this region and therefore $\mathrm{LET_d}$ approaches a singularity. No difference is observed among doses calculated with and without energy spectra (results not shown).

5.3.3 Comparison to Monte Carlo depth dose curves

By comparing our model to Monte Carlo results we verified our dose calculations and obtained the relative contribution of each fragment isotope to the total dose. The depth dose curve of the Monte Carlo simulation and the analytical model (figure 5.1) agree for the primary carbon ions and all fragments but hydrogen (figure 5.1b). When combining the dose from primary ions and all fragments the analytical model predicts less dose right ahead of the Bragg peak than the simulations (figure 5.1d). It does seem like we systematically underestimate the fragment dose in depths smaller than $R_\mathrm{f}\,(D_\mathrm{max})$. The relative contribution of each fragment isotope can be found in table 5.1.

Table 5.1: *The table lists up to three isotopes for each element whose weighted sum is the best analytical representation of a depth dose curve obtained by Monte Carlo simulation. The dose is normalized to a primary carbon ion beam with unity entrance dose.*

	Isotope 1		Isotope 2		Isotope 3	
Element	A	D_max(a.u.)	A	D_max(a.u.)	A	D_max(a.u.)
Hydrogen	1	0.046				
Helium	3	0.039	4	0.029		
Lithium	5	0.0055	6	0.0034	7	0.0017
Beryllium	8	0.0876				
Boron	9	0.0436	10	0.0533	11	0.0640
Carbon	9	0.0101	10	0.111	11	0.150

5.3.4 $\mathrm{LET_d}$ of the complete beam

Using the relative contributions of each isotope we can calculate the $\mathrm{LET_d}$ of the beam with primary ions and all its fragments (figure 5.4). The $\mathrm{LET_d}$ shows some very distinct steps and peaks that are correlated with different fragment isotopes. Those steps that are found in depth smaller than $R_{\mathrm{hi},0}$ are in depths $R_\mathrm{f}\,(D_\mathrm{max})$ of fragments with $\lambda_\mathrm{f}^\mathrm{hi} < 1$. The

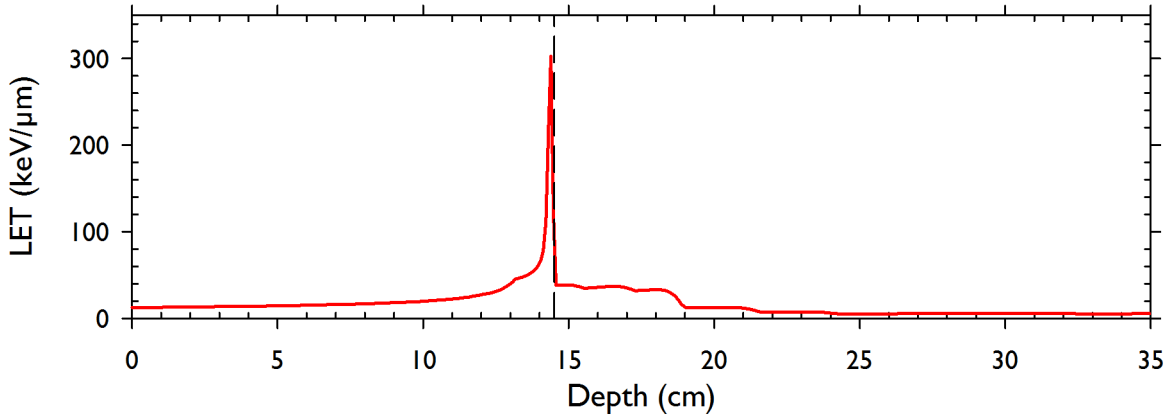

Figure 5.4: *Total LET_d of a carbon ion beam*

other steps are in depths were fragments with $\lambda_f^{hi} > 1$ reach their maximum depth $R_{f,max}$. Despite the high maximum LET_d values that we observed for individual fragment isotopes and the primary ions the total LET_d does not exceed 290 keV/μm. As high LET_d values are always linked to very low dose values the dose–averaging of the total LET_d suppresses most of these peaks. Hence, the only fully visible LET_d peak is that of hydrogen–1 and helium–4 as these fragments have the longest range in water. The peak is located at 45 cm water equivalent depth and therefore not visible in figure 5.4.

5.3.5 LET of SOBPs

The influence of dose–averaging is clearly visible when we turn to the LET_d of SOBPs. Figure 5.5 shows two SOBPs, one created with a single field (figure 5.5a) and the other created with two opposing fields (figure 5.5b). The length of the respective SOBPs is 4 cm and they are placed in the center of a 20 cm water phantom. Across the first SOBP (figure 5.5a) the LET_d rises with increasing depth from $\sim$ 40 keV/μm up to $\sim$ 130 keV/μm at the distal edge. It decreases monotonously behind the SOBP. The LET_d in the second SOBP is nearly symmetrical with two maxima ($\sim$ 90 keV/μm) located at the edges of the SOBP. In the center the LET_d drops down to $\sim$ 40 keV/μm. Outside the target the LET_d does not exceed $\sim$ 25 keV/μm.

5.4 Discussion and Conclusions

In this section we have shown how to adapt already existing analytical dose and LET calculation algorithms for protons such that they can be used for primary ions. The model

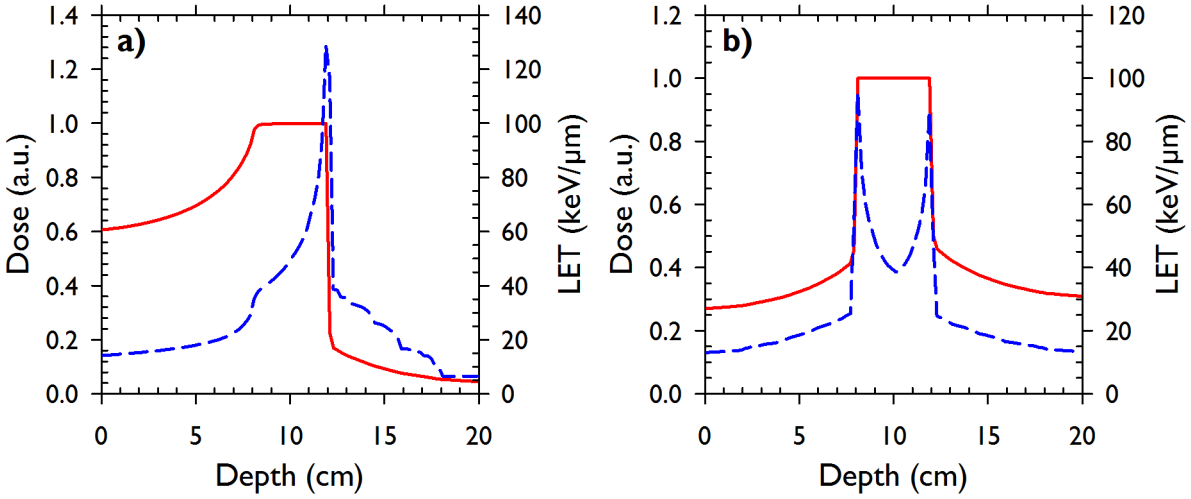

Figure 5.5: *Dose (solid red) and LET_d (dashed blue) of a spread out Bragg peak created with a single field (a) and two opposing fields (b).*

for primary ions reproduces Monte Carlo depth dose curves with an appropriate absorption coefficient and width of the energy spectrum. We also developed a novel analytical model for the dose, the fluence, and the LET of the fragments of ion beams making various assumptions. A comparison to Monte Carlo simulation results showed that the assumptions seem to be valid for all elements but hydrogen. We assumed that all fragments are remnants of primary ions. It turns out that the number of proton fragments that are not remnants of the primary ions cannot be neglected. A similar observation was made by Grassberger *et al.* (2010). They reported that for the LET calculation of therapeutic proton beams the contribution of secondary protons cannot be neglected. When we assumed that the energy per nucleon is conserved this included that the angular spread of newly created fragments is very small. This is clearly violated for secondary protons as experiments by Matsufuji *et al.* (2005) have shown. Straggling can definitely not be neglected. Ignoring it would overestimate the influence of fragments on LET_d behind the Bragg peak. As we expected we can more or less ignore the dose of fragments in front of the Bragg peak but the increase of 10 keV/μm in the LET_d cannot be ignored as this is the region where the fastest RBE changes are observed (Kraft 1987). Therefore the contribution of fragments to the total LET_d must not be ignored.

The actual single Bragg peak is unlikely to be used to irradiate a patient but it is more likely that large fields consisting of many Bragg peaks are used. When choosing the beam configuration it has to be considered that single fields offer higher LET_ds at least at their distal edge than SOBPs consisting of more than one field.

In conclusion we expect that the novel model for the calculation of LET_d and dose of fragmenting ion beams is sufficiently accurate to be used in the development of biological optimization routines for carbon ion therapy. It provides a fast and easily implementable way to assess the beam quality. For future developments we would like to conduct enhanced Monte Carlo simulations to verify our LET_d results and to improve the cross sections for each fragmentation channel. The high difference in LET_d within a SOBP underlines the high potential for selective shaping of the dose to radioresistant tumor regions. This potential can only be exploited by intensity modulated particle therapy where locally high dose gradients can be applied.

Chapter 6

Opening up New Avenues: Advancing Radiobiological Models

The aim of the following chapter is to make use of the newly developed beam quality measures and actually improve biological models. First, we will present a newly developed model to include the effect of oxygen on tissue radiosensitivity into treatment planning. Biological parameters for well oxygenated tissue are adapted for hypoxic tissues and it is demonstrated how this could be integrated into treatment planning. Recently, Carlson *et al.* (2008) introduced the RMF model, a mechanistic approach to describe the radiobiologic damage by relating double strand breaks to cell kill. The model has so far only been applied to monoenergetic proton and carbon ion beams. Here, we are going to show how it can be used to predict biological parameters and RBE of realistic particle beams.

6.1 Could C–12 overcome hypoxia effects? An approach to include hypoxia into particle treatment planning

The higher the LET of a radiation modality, the more sensitive is tissue to its dose (Ando and Kase 2009). The actual change of RBE with the LET depends not only on the cell type but also on the cell's microenvironment. One of the key factors in the microenvironment that impact radiosensitivity is the partial oxygen pressure (pO_2) (Alper and Howard-Flanders 1956). The lack of oxygen supply that can be observed in many tumors increases their radioresistance significantly. How much more dose is required to gain the same biological effect in poorly (hypoxic) compared to well oxygenated (aerobic) tissues

can be quantified by the hypoxia reduction factor (HRF; a description of the HRF and its relation to the oxygen enhancement ratio can be found in the following paragraph). *In vitro* some cell lines irradiated with photons have expressed HRF values exceeding 3, *in vivo* HRF values of up to 1.8 have been estimated (Carlson *et al.* 2006). When investigating the radiosensitivity of cells to heavy ion irradiation in the absence of oxygen it was observed that the HRF decreases with increasing LET (Barendsen *et al.* 1966). Hence, the RBE of high–LET radiation is reinforced by a decreasing HRF making it even more effective. There has been some speculation on the benefit of the reduced HRF but most studies have focused on measuring it *in vitro* (Furusawa *et al.* 2000). In order to get first estimates on the effectiveness of particles in the patient we developed a model to incorporate the HRF in an already existing treatment planning system for heavy ions. In modern 3D IMPT plans (Lomax 1999) the absorbed dose and LET distributions are highly degenerated, such that it is very complicated to estimate the biological effect in advance. Hence, it is difficult to infer from *in vitro* data points on the impact of actual distributions without knowing them. We do not claim to be able to predict real outcome in the patient as too many of the input parameters are subject to large uncertainties. We rather focused on clarifying our assumptions and ensuring that our results provide a reasonable guess i.e. our results shall give a realistic insight in what we may expect from using carbon ions for hypoxic tumors. The model was designed with carbon ions in mind but is not restricted to them. It can easily be extended to protons, other heavy ions, and even photons. All further calculations were performed for carbon ions.

Hypoxia reduction factor With decreasing partial oxygen pressure p more dose is required for the same rate of cell kill. The ratio of the dose $D(p)$ required in oxygen depleted cells to the dose $D(p_{\text{aerobic}})$ required for the same rate of cell kill in fully oxygenated cells is called hypoxia reduction factor (HRF) (Carlson *et al.* 2011)

$$HRF(p) = \frac{D(p)}{D(p_{\text{aerobic}})} \tag{6.1}$$

It is common practice to measure the influence of oxygen on the biological effect in terms of the oxygen enhancement ratio (OER) which is defined as

$$OER(p) = \frac{D(p_{\text{hypoxic}})}{D(p)} \tag{6.2}$$

where $D\left(p_{\text{hypoxic}}\right)$ is the dose required for fully hypoxic cells. The two definitions are related by the equation

$$HRF\left(p\right) = m\frac{1}{OER\left(p\right)} \tag{6.3}$$

Here m is the maximum HRF/OER. We believe that the definition of the HRF is more intuitive than OER as it is based on the normal situation of healthy cells (aerobic). With increasing abnormality and decreasing $p\mathrm{O}_2$ the factor increases i.e. healthy aerobic cells have an HRF of 1. The OER on the other hand is based on hypoxic cells that are usually not observed in healthy tissue. Healthy cells have the highest OER which is counterintuitive as the author has frequently observed in discussions with colleagues.

6.1.1 Methods and Materials

The new model was designed to be used within the existing biological effect optimization in *KonRad*. The two parameters of the LQ model, α and β, are input parameters for the treatment planning system. Due to the physical properties of carbon ions those parameters depend on the irradiated tissue, the initial energy of the carbon ion beam, and the depth of the tissue inside the patient. The new model adds another dependency: within the tumor the $p\mathrm{O}_2$ shall also be considered. Hence, two major sections of the new model can be identified: the generation of new $p\mathrm{O}_2$ dependent input parameters that are patient independent and the patient specific calculation of the $p\mathrm{O}_2$ in each voxel in the TPS. Therefore, the flowchart in figure 6.1 is split in two major parts. Within this section we will follow the circled numbers in the flowchart to describe each of the steps of the new model. A big effort was put on retaining a high degree of flexibility in the model. Each part is designed as a module that can be easily exchanged for future enhancements.

6.1.1.1 The preparation part

The first part of the model generates the patient independent input data for the treatment planning system. The current biological optimization uses the biological effect $\mathcal{E}$ instead of the RWD. The LQ–parameters α and β are input parameters derived from the LEM (Scholz and Kraft 1996) that are stored in tables. Parameters are available as a function of irradiated tissue, initial particle energy, and water equivalent depth. We assume that these parameters represent aerobic tissue and are going to use the dependency of the HRF on the LET to transform them for lower $p\mathrm{O}_2$. The work flow of generating these input parameters is outlined in figure 6.1. Starting from a data point on a depth dose curve

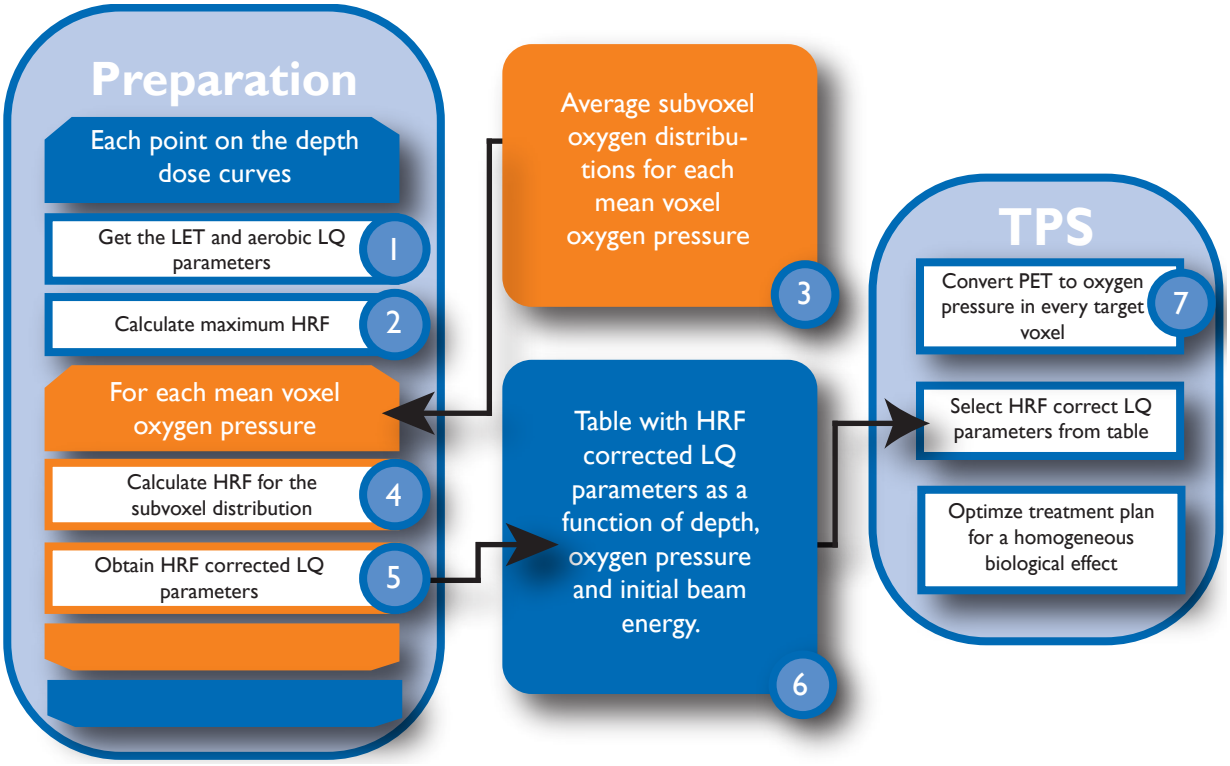

Figure 6.1: *A flow chart outlining the proposed treatment planning procedure.*

we take the respective biological parameters out of our tables and calculate the LET (1). The LET is calculated using the analytical model presented in chapter 5. Thereafter, we can use the dependence of LET and HRF to calculate the maximum HRF m (2). In the next step we take a look at a single voxel's pO_2. For numerous voxel pO_2 values we have simulated average underlying subvoxel pO_2 distributions (3). Given the LET and m the pO_2 distributions are converted into HRF distributions (4) for which we can determine surival curves. By fitting equation (2.12) to these curves the HRF–corrected parameters α_H and β_H are extracted (5). The data is then stored in a table (6) as input parameters for the treatment planning system.

HRF and LET Once we have calculated the dose–averaged LET for every data point we can turn towards its influence on the HRF. Based on published cell survival data obtained under hypoxic and aerobic conditions for a wide range of LET values (Furusawa *et al.* 2000) we model the change of the maximum HRF m with the LET using

$$m = r \cdot \mathrm{erf}\left(-s \cdot LET + t\right) + 2 \tag{6.4}$$

where r, s, and t are fit parameters. The term erf denotes the Gauss error function. According to equation (6.4) m decreased from $\approx r + 2$ to 1 with increasing LET. This model cannot describe all the effects of oxygen on the processing of radiation damage. We do make the assumption that the key role of oxygen is the fixation of initial DNA damage, a process that is independent of the cell type. Hence, we can use the same parameters r, s, and t for all cell lines. Parameters were determined by fitting the equation to the 10 % survival doses published in Furusawa *et al.* (2000) of carbon ions. Following our assumption that the HRF is cell line independent we combined the data for HSG and V79 cells.

HRF and pO_2 So far we can only describe the extreme situations of fully hypoxiy or aerobic cells. The critical cells at intermediate oxygen levels (Wouters and Brown 1997) cannot be considered correctly as there is no published data on the change of the HRF with pO_2 and LET. In the previous paragraph we assumed that the oxygen directly fixes the initial DNA damage. How much DNA is damaged depends on the radiation modality but the processing of the damage and the fixation by oxygen are independent of the radiation modality. Therefore, the change of radiosensitivity with pO_2 is modeled in analogy to the Alper–Howard–Flanders model (Alper and Howard-Flanders 1956) for photons by employing

$$HRF\,(p) = \frac{m \cdot K + p}{p + k} \tag{6.5}$$

as in Carlson *et al.* (2011).* The authors of the latter publication analyzed the data of various other publications and found that for photons $m = 2.8$ and $K = 1.47$ mmHg represent the data best. Following our assumptions we are going to use the same K value for carbon ions but replace m with equation (6.4). In combination with equation (6.5) we are going to use it to perform step (4) in figure 6.1.

Subvoxel oxygen distributions Whatever imaging modality is used to determine the pO_2 distribution in the tumor the information will always be per voxel. Due to physical limitations the spatial resolution of PET images is in the order of several mm. As the pO_2 changes on the μm scale within tissue, the actual oxygen supply of a cell within a voxel will certainly differ from the value measured for the whole voxel. We assume that the measured value is the mean of the underlying subvoxel oxygen distribution. Hence, we

*A very similar equation is used to describe the relation of the partial oxygen pressure and OER $OER\,(p) = [K_{\mathrm{OER}} + mp] \,/\, [K_{\mathrm{OER}} + p]$ where $K_{\mathrm{OER}} = m \cdot K$.

simulated possible underlying distributions using a published method (Petit *et al.* 2009). We are not going to present any details here as our simulation merely confirmed previously published results. In total we simulated subvoxel oxygen distributions for mean pO_2 values ranging from 0.5 mmHg up to 31.5 mmHg (maximum mean pO_2 in our simulation) in steps of 1.0 mmHg. For each mean pO_2 value at least 200 simulated distributions were averaged.

HRF–corrected parameters The simulated subvoxel oxygen distributions contain each 10,000 cells. To ease the storage of these data points the average subvoxel distributions are stored as histograms with a bin resolution of 0.1 mmHg. The value of each bin i is normalized such that it represents the relative number q_i of cells with a certain pO_2 p_i . For a given mean pO_2 $\bar{p}$, dose D, LET LET, and aerobic LQ parameters α_A and β_A the relative cell survival per voxel is

$$S(\bar{p}) = \sum_i q_i \exp\left(-\frac{\alpha_A}{HRF(p_i, LET)} D - \frac{\beta_A}{HRF^2(p_i, LET)} D^2\right) \tag{6.6}$$

$$= \exp\left(-\alpha_H(\bar{p}, LET)\, D - \beta_H(\bar{p}, LET)\, D^2\right) \tag{6.7}$$

We calculate cell survival curves up to 20 Gy using equation (6.6) and fitted equation (6.7) to them. Thereby we obtained the HRF–corrected LQ parameters α_H and β_H.

6.1.1.2 The TPS part

Once all the patient independent calculations have been performed the treatment planning system takes over. The crucial point at this stage is how to obtain the pO_2 in every single voxel. We assume at this point that it is possible to infer the pO_2 from functional images that have been co–registered to the treatment planning CT. Various dose–painting–by–numbers studies (Bentzen 2005) have been published, all using very different methods to prescribe the dose based on image intensities. Currently three different approaches are used to link imaging information to dose prescription. The first approach is to linearly scale the prescribed dose with the intensity obtained from the functional image (Grosu *et al.* 2007, Flynn *et al.* 2008, Rickhey *et al.* 2008, Alber *et al.* 2003). The second approach is to determine the partial oxygen pressure in a voxel from the imaging information and use known relationships between the pO_2 and cell survival to scale the dose (Petit *et al.* 2009, Malinen *et al.* 2006). The third approach is to relate radiosensitivity to information obtained from time resolved images and use a tumor control probability model for optimization (Thorwarth *et al.* 2005, 2007). We are not going to describe the existing methods in detail at this point. Within this model we will focus on the relationship of the partial oxygen

pressure and PET image intensities. In a recently published study (Chang *et al.* 2009) the authors performed FMISO PET scans and locally co–registered pO_2 measurements with Eppendorf electrodes. Though the exact relation between pO_2 and FMISO PET image intensity varied for each tumor they concluded that in voxel i the relationship of FMISO image intensity F_i and partial oxygen pressure p_i can be approximately described by

$$p_i = K_{50} \cdot \left(\frac{F_{\max}}{F_i} - 1 \right) \tag{6.8}$$

The maximum FMISO PET image intensity within the tumor is $F_{\max}$ and K_{50} is a fit parameter describing the partial oxygen pressure for which the image intensity is at half maximum. In their study they calculated a mean value of $K_{50} = (6.4 \pm 5.4)$ mmHg. We will be using this value in our study. We would like to clarify at this point that the choice of this model is not crucial for the feasibility of this project. As long as this model creates realistic distributions of the pO_2 in the tumor any other model would only change the local oxygen distribution but not the complete picture of the method. If any other more accurate model is available we can easily replace the current.
Once the pO_2 is determined, appropriate biological parameters can be selected from the table created in the preparation part and the standard biological optimization for carbon ions can be launched. To demonstrate the capability of the treatment planning system we optimized SOBPs in various scenarios. We also optimized treatment plans for two patient cases but are unfortunately not able to show these. The institution providing the PET data did not grant permission to publish any results based on them.

6.1.2 Results

HRF and LET A model for the change of the maximum HRF m with $\mathrm{LET_d}$ was obtained by fitting a simple model to the data extracted from Furusawa *et al.* (2000). Figure 6.2 depicts the data points for two different cell lines (V79 and HSG) and the maximum HRF m our fit of equation (6.4) to the data predicts. The goodness of the fit is $R^2 = 0.90$. The fit parameters can be found in table 6.1. According to figure 6.2 m changes mainly in the region of of 40 keV/μm to 110 keV/μm which corresponds to the $\mathrm{LET_d}$ range in a C–12 SOBP (cf. figure 5.5). The original publication contains data for two cell lines (V79 and HSG cells) for carbon ions. As it can be seen in figure 6.2 there is no obvious difference between the two cell lines. This goes along with our previous assumption that the HRF is independent of the cell type.

Table 6.1: *Parameters r, s, and t obtained by fitting equation (6.4) to data published by Furusawa et al. (2000).*

Parameter	Value
r	0.98
s	$1.65 \cdot 10^{-2}$ μm/keV
t	1.73

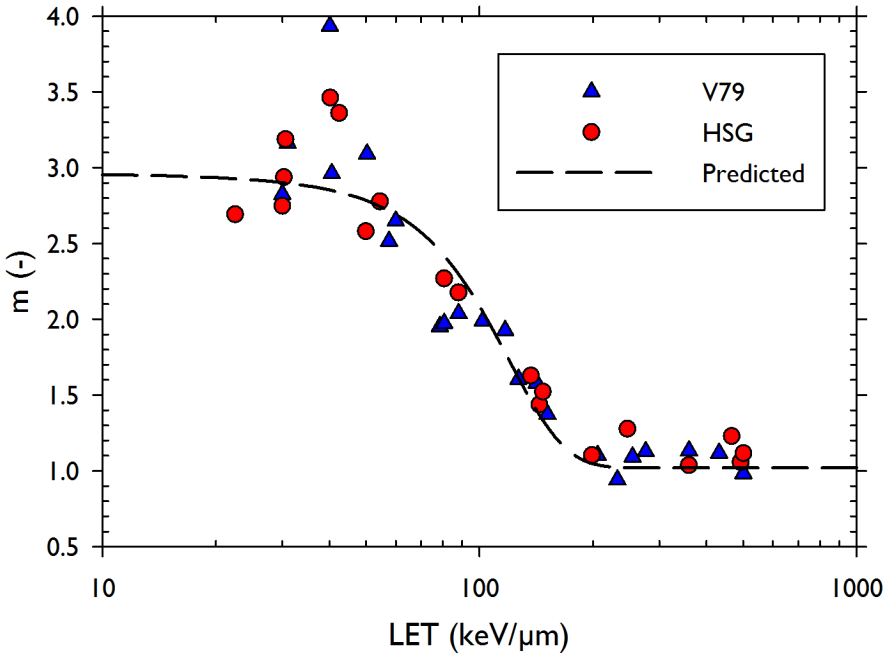

Figure 6.2: *Maximum HRF m as a function of the LET for two different cell lines. Data extracted from Furusawa et al. (2000). The dashed black line is the value of m predicted by equation (6.4) using parameters in table 6.1.*

HRF corrected LQ parameters α and β The influence of $\mathrm{LET_d}$ and the $p\mathrm{O_2}$ on cell survival is clearly reflected in the HRF corrected α and β curves we calculated. As an example figure 6.3 shows five curves of α as a function of depth for a carbon ion beam with an initial energy of 276 MeV/u. Each curve represents differently oxygenated chordoma tissue. The parameter α decreases with decreasing $p\mathrm{O_2}$. Assuming that tissue with a $p\mathrm{O_2}$ of 31.5 mmHg is aerobic the values drop down to half for fully hypoxic cells in low LET regions. Only very little change can be observed in the high LET region around the Bragg peak. According to figure 6.3 α changes more rapidly once the $p\mathrm{O_2}$ drops below 10 mmHg. Observations for β are similar. For very low $p\mathrm{O_2}$ values β is negligible.

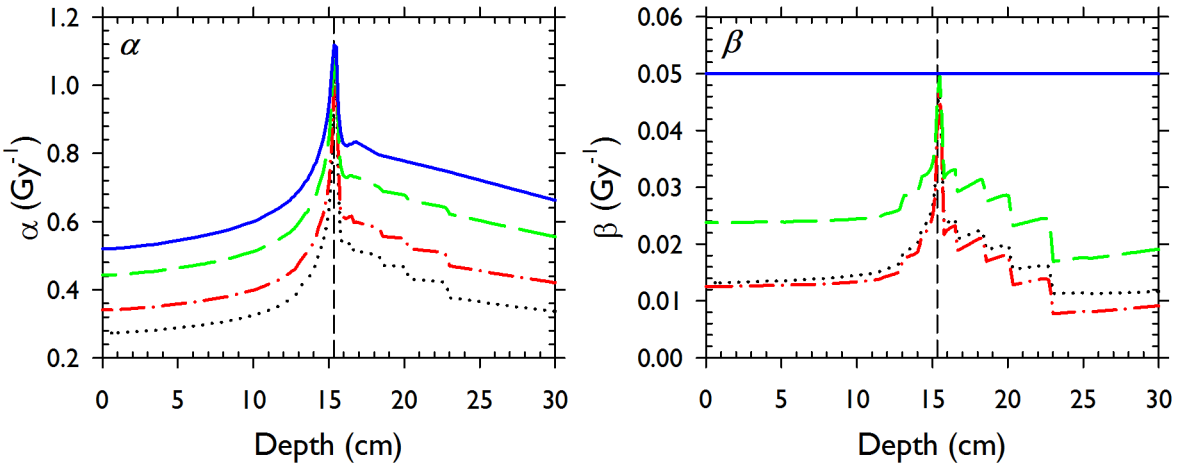

Figure 6.3: *The HRF–corrected parameters α and β for chordoma tissue as a function of depth for five different pO_2 values. Regular cells are assumed to have a pO_2 of 31.5 mmHg (solid blue). Additional curves are given for 10.5 mmHg (dashed green), 3.5 mmHg (dash–dotted red), and 0.5 mmHg (dotted black). Curves generated for a 276 MeV/u C–12 beam with a residual range of 14.3 cm (vertical dashed black line).*

Constant biological effect and different pO_2 values: SOBP and the simultaneous boost The new routine in the treatment planning system is able to optimize treatment plans with constant RWD. Figure 6.4 depicts the physical dose of five SOBP each delivering a constant RWD of 3 Gy (RBE) given different pO_2 values. The latter is constant across the whole target. We can clearly see that with reduced pO_2 more dose is necessary for the same biological effect. The additionally required dose depends significantly on the local LET. At the distal edge of the SOBP only little extra dose is required compared to the dose at the proximal edge. The increase in dose is not only due to the higher HRF but also due to the lower RBE. The LQ–model predicts a decreasing RBE with increasing dose. Please note that the dose distributions for the low pO_2 values could never be delivered in a patient. The normal tissue dose exceeds the allowed limits by far if we assume that normal tissue has similar biological parameters as a fully oxygenated tumor. HRF alone is an inadequate measure to quantify the benefit from carbon ions under hypoxic conditions. Oxygen depleted regions require more dose which reduces the RBE i.e. the benefit is reduced. The ratio of hypoxic and aerobic doses shown in figure 6.5 includes both effects. Essentially, the RBE decrease did not outrun the benefit of an reduced HRF and we need significantly less additional carbon ion than photon dose. Among the carbon ion doses the inhomogeneity of the distributions indicates that the high LET effect is pronounced for low pO_2 situations. The photon ratios were calculated by applying equation (6.5) to the respective subvoxel oxygen distributions.

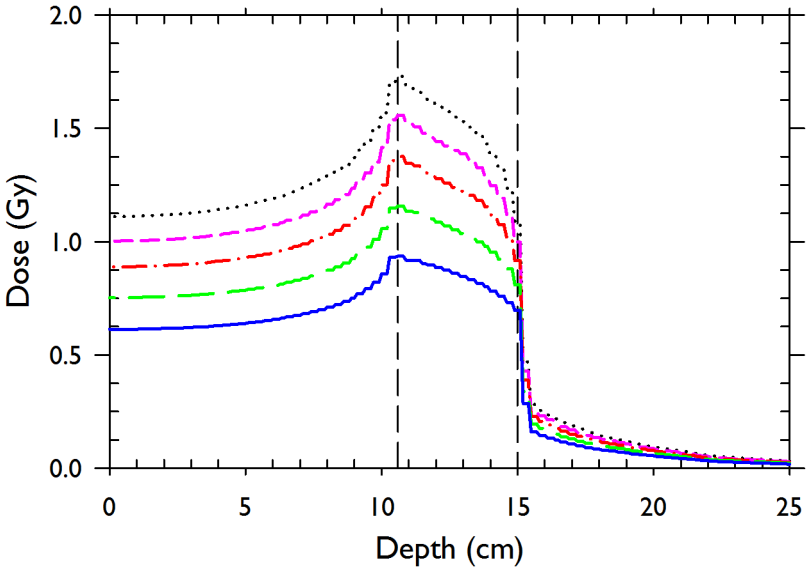

Figure 6.4: *Absorbed dose of five SOBPs delivering a constant RWD of 3 Gy (RBE) given a respective pO_2 of 0.5 mmHg (dotted black), 2.5 mmHg (short–dashed pink), 5 mmHg (dash–dotted red), 10 mmHg (long–dashed green), and 31.5 mmHg (solid blue) across the target (dashed black).*

The capability of carbon ions to deliver highly conformal RWD distributions with very steep absorbed dose gradients is shown in figure 6.6. A dose of 3 Gy (RBE) was prescribed to a target with an oxygen depleted region in its center. We varied the pO_2 of the oxygen depleted region and kept it constant in the remainder of the target at 31.5 mmHg (fully oxygenated). In any case the treatment planning system optimized a treatment plan with a constant RWD across the whole target volume created by two opposing fields. The dose at the edges of the oxygen depleted region is in any case lower than in the center due to the increased LET at the edges. The lower the pO_2 the higher the influence of the LET (cf. figure 6.3). In order to generate constant RWD distributions the TPS creates highly degenerated dose distributions. For the low pO_2 cases the dose has to be varied within the oxygen depleted region by up to 20 %. The reduction of the radiosensitivity in an oxygen depleted region within the target is significantly lower for carbon ions than for photons. Figure 6.7 shows the ratio of doses required in the oxygen depleted region to the dose required in the fully oxygenated case. The influence of the LET is visible in the drop of the ratio at the edges of the oxygen depleted region. Comparing figures 6.5 and 6.7 we observe that the optimizer is able to model the biological effect better if only a small region within the target is oxygen depleted and not the whole target.

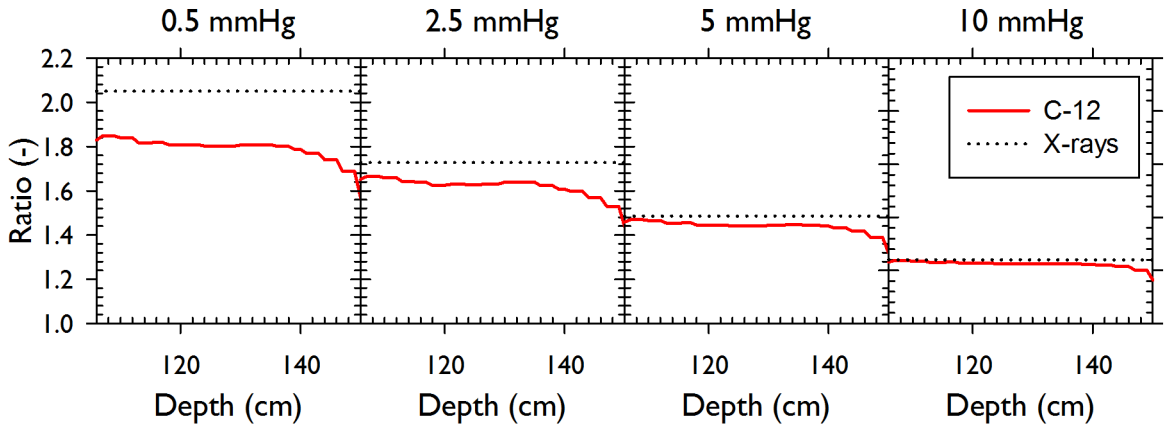

Figure 6.5: *The ratio of doses required to deliver a constant RBE-weighted dose of 3 Gy (RBE) across a 5 cm wide target for carbon ions and photons if the pO_2 across the whole target drops from 31.5 mmHg (aerobic) to the respective value. Carbon ion doses were optimized with the treatment planning system while the photon doses are ideal doses.*

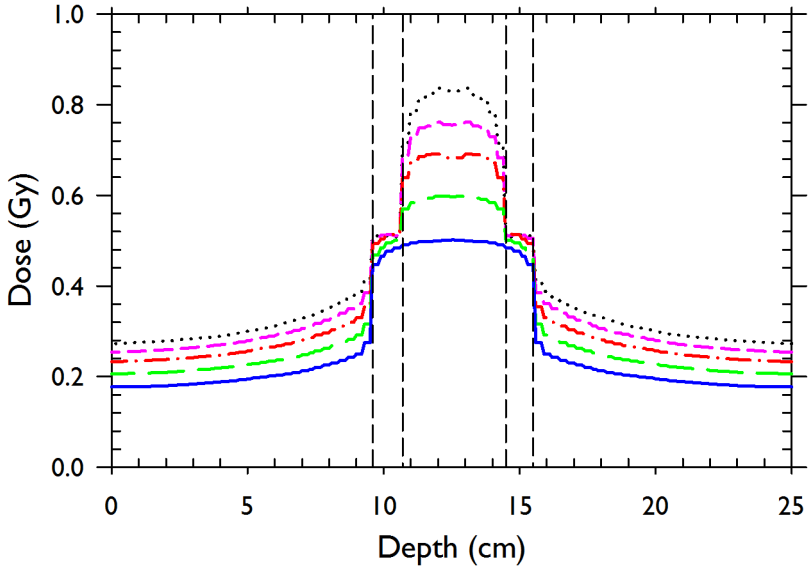

Figure 6.6: *Absorbed dose of five opposing field SOBPs all delivering a constant RWD of 3 Gy (RBE) across a target with a central boost region of 0.5 mmHg (dashed black), 2.5 mmHg (short–dashed pink), 5 mmHg (dash–dotted red) and 10 mmHg (long–dashed green) pO_2. The target region outside the boost is fully oxygenated.*

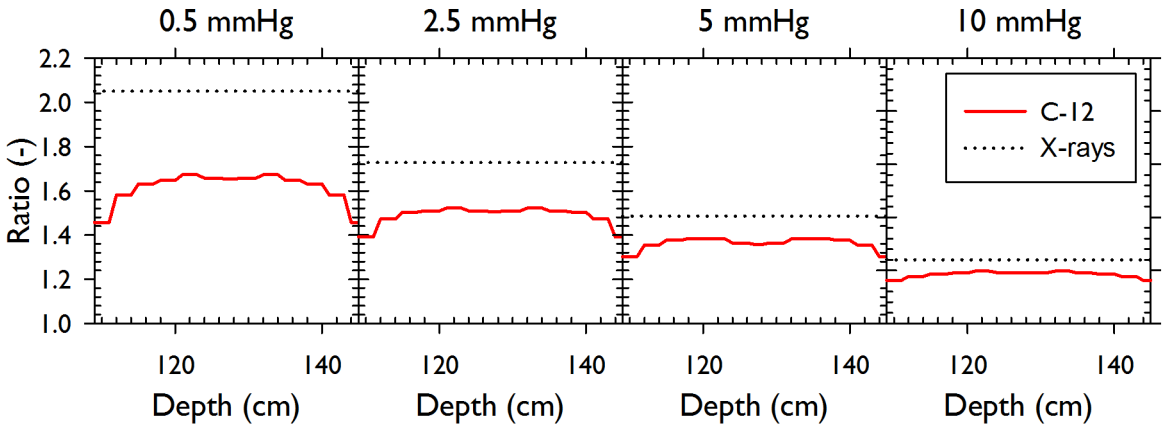

Figure 6.7: *The ratio by which the carbon ion and photon dose across four different low pO_2 boost volumes has to be increased compared to an aerobic case (31.5 mmHg) in order to maintain a constant RWD of 3 Gy (RBE). Carbon ion ratios were calculated from figure 6.6 while the photon ratios are ideal calculations for simulated subvoxel distributions using equation (6.5).*

6.1.3 Discussion and Conclusions

The aim of this study was the design and testing of a treatment planning routine for carbon ions that incorporates the influence of the partial oxygen pressure on the tumor radiosensitivity. The complexity of the novel approach ranging from unknown branching fractions of fragmentation channels to the relation of PET tracer uptake and pO_2 forced us the make numerous severe assumptions. In this section we are going to revisit those assumptions that have the biggest influence on the outcome of the treatment plans.
Knowing the LET of the carbon ion beam is a prerequisite for our model as the maximum HRF m depends on it. Based on cell survival data for two different cell lines (V79 and HSG) we obtained a function describing the change of m with LET. The differences among parameter sets for each cell line were small compared to other uncertainties such that we cannot see our assumption that m is independent of the cell type affected. Using an error function to model the data is a best guess and not based on biological or physical considerations. The definition of the HRF suggests that it should approach unity for high LET values. On the other hand we know that low LET particles express similar cell survival curves as photons. Our results predict a maximum HRF for particles greater than that of photons (2.98 for C–12 ions vs. 2.8 for photons). There is a variety of possible explanations for this. On one hand the maximum HRF for carbon ions was obtained for two cell lines only while the photon values were obtained from a broad variety of cell lines and experiments. On the other hand carbon ion beams with LET values below 10 keV/μm

are most likely never observed in a patient. In several simulations of carbon ion SOBPs we never observed an LET of less than 40 keV/μm within the target, approximately the same value for which carbon ions and photons have the same maximum HRF.
The high potential of dose shaping in hypoxic tumors with carbon ions is apparent when we consider the change of α and β with $p\mathrm{O}_2$ and depth. Their peak–to–entrance ratio is nearly doubled when we compare fully hypoxic to aerobic voxels. This potential cannot be fully exploited in the patient due to dose–averaging of the LET and the biological parameters in large fields but still we expect high dose and RBE gradients in the presence of inhomogeneous oxygen distributions.
The single field SOBP confirmed that the ratio of doses required for the same RBE–weighted absorbed dose in oxygen depleted and aerobic tumors varies significantly from the distal to the proximal edge of the SOBP. This is not equivalent to the HRF as the RBE is not the same for aerobic and hypoxic voxels. Lower $p\mathrm{O}_2$ values require more dose and therefore the RBE decreases. Hence, the dose has to be increased even more to obtain the required biological effect. But still the ratio is always smaller than the HRF of photons even if the difference is relatively small.
On the other hand we obtained RWD distributions with two fields for a target with an oxygen depleted region in its center that could be delivered safely. Though the physical dose required varies significantly across the target the RWD could be kept constant and the increase in physical dose outside the target is a lot smaller. The high potential in shaping doses for tumors with varying $p\mathrm{O}_2$ values is confirmed by the fact that the ratio of doses required for aerobic and oxygen depleted voxels is smaller than for the single field. This may well be due to the small size of the oxygen depleted region and the therefore higher LET. The capability of the treatment planning system to shape the dose along these unrealistically steep oxygen distributions gives confidence that in cases with realistic oxygen distributions dose shaping should be easily possible.
The most critical assumption of our model is that we can actually derive $p\mathrm{O}_2$ distributions from PET images. We are aware that there are many problems associated with this and that it will not be possible to present any reliable results is the near future. Yet the aim of this study was a feasibility test and therefore we are not expecting to get most accurate results. As long as the results are realistic and in the right order of magnitude we can get estimates on the potential and the risks of using carbon ion therapy on hypoxic tumors.
For future projects we will continue at this point. We want to evaluate current treatment plans on how they perform in the presence of hypoxia and define new treatment planning strategies that reduce the risk of treatment failure in hypoxic tumors.

6.2 Predicting the RBE of particles with the mechanistic repair–misrepair–fixation model

In this section, we develop a mechanism–based approach to predict spatially varying proton and carbon ion RBE for representative SOBP. In section 2.2.4 we used the repair-misrepair-fixation (RMF) model (Carlson *et al.* 2008) to develop formulas explicitly linking radiosensitivity parameters in the widely used LQ model to induction and biological processing of DNA double strand breaks (DSB). To minimize the number of ad hoc adjustable parameters, a published Monte Carlo Damage Simulation (MCDS) (Semenenko and Stewart 2004, 2006) is used to predict the effects of radiation quality on DSB induction. A multiscale modeling approach such as this is potentially advantageous because the RBE for clinically relevant particle distributions is guided by well-established physical and biological considerations. Here, we will briefly describe how a model developed for monoenergetic particles can be extended to particle beams including an energy spectrum. A correct averaging is crucial in order to predict the RBE correctly within the model. The models and methods are used to examine the impact of tissue radiosensitivity on RBE for monoenergetic protons and carbon ions as well as more clinically relevant proton and carbon ion SOBP. This section has been submitted for publication (Frese *et al.* 2011b).

6.2.1 Methods and Materials

Determination of LQ parameters in a pristine Bragg peak Particle beams used in clinical radiotherapy have an energy spectrum that cannot be neglected. The two main components are the initial energy spectrum of the accelerator and contributions of stochastic interactions of particles in matter that give rise to so–called straggling. Assuming that both components of the particle distribution have a Gaussian spectrum (Bortfeld 1997), the width of the combined spectrum can be obtained by quadratic addition of the individual widths. Particles of different kinetic energies, and hence different RBE, contribute to the total physical dose deposited at any given location. Within the framework of the LQ–model, the synergistic effects of radiation may be incorporated into RBE calculations by computing dose–averaged parameters α_{D} and $\sqrt{\beta_{\mathrm{D}}}$ (Zaider and Rossi 1980, Wilkens and Oelfke 2006, and section 2.2.1). We extend this approach to an energy spectrum using the same method that Wilkens and Oelfke (2003) used to calculate dose–averaged LET for a proton beam with an energy spectrum. As energy, range, and depth in tissue are directly correlated (Wilson 1946), a spectrum of energies can also be expressed as a

spectrum of ranges or depths. The latter is used here so that dose and dose–averaged radiation sensitivity parameters α_{D} and β_{D} are presented as a function of depth:

$$\alpha_{\mathrm{D}}(z) = \frac{\int_{-\infty}^{R_0} \mathrm{d}z' \, \alpha(z') \, \phi_{z'}(z) \, S(z')}{\int_{-\infty}^{R_0} \mathrm{d}z' \, \phi_{z'}(z) \, S(z')} \tag{6.9}$$

$$\sqrt{\beta_{\mathrm{D}}}(z) = \frac{\int_{-\infty}^{R_0} \mathrm{d}z' \, \sqrt{\beta(z')} \phi_{z'}(z) \, S(z')}{\int_{-\infty}^{R_0} \mathrm{d}z' \, \phi_{z'}(z) \, S(z')} \tag{6.10}$$

Here, $\phi_{z'}(z)$ is the Gaussian distribution of particles about depth z that have the same stopping power $S(z')$ as monoenergetic particles would have at depth z'. If we apply equations (6.9) and (6.10) to equations (2.26) and (2.27), respectively, we obtain

$$\alpha_{\mathrm{D}}(z) = \theta \langle \Sigma(z) \rangle_{\mathrm{D}} + \kappa \left\langle \bar{z}_{\mathrm{f}}(z) \, \Sigma(z)^2 \right\rangle_{\mathrm{D}} \tag{6.11}$$

$$\beta_{\mathrm{D}}(z) = \frac{\kappa}{2} \langle \Sigma(z) \rangle_{\mathrm{D}}^2 . \tag{6.12}$$

Here, $\langle \cdot \rangle_{\mathrm{D}}$ denotes a dose–averaged value.

Low–LET reference radiosensitivity parameters As indicated by equation (2.32), RBE depends on radiation quality through the $\bar{z}_{\mathrm{f}}$ and Σ parameters, absorbed dose, and $(\alpha/\beta)_{\mathrm{x}}$. Because dose, $\bar{z}_{\mathrm{f}}$ and Σ are estimated using physical models or an independently tested Monte Carlo simulation, our approach predicts that RBE varies among tumor–types and tissues solely because of differences in $(\alpha/\beta)_{\mathrm{x}}$. For this reason, multiple sets of low–LET radiosensitivity parameters (table 6.2) were employed. For comparison with measured trends in radiosensitivity (Furusawa *et al.* 2000), we used the respective low–LET reference parameters for each cell line. The reference DSB yield $\Sigma_{200\,\mathrm{kVp}} = 8.68\ \mathrm{Gy}^{-1}\ \mathrm{Gbp}^{-1}$ for 200 kVp X–rays was simulated in MCDS with a secondary electron spectrum obtained from MCNP†. The frequency–mean specific energy $\bar{z}_{\mathrm{f},200\,\mathrm{kVp}}$ was calculated for $S_{200\,\mathrm{kVp}} = 1.53\ \mathrm{keV}/\mu\mathrm{m}$. For all other calculations, we used three additional reference data sets representing chordoma (Krämer and Scholz 2000), prostate (Carlson *et al.* 2004), and head and neck tumors (Girinsky *et al.* 1993, Stuschke and Thames 1999), which cover a large range of $(\alpha/\beta)_{\mathrm{x}}$ observed *in vivo*. To calculate RMF model parameters θ and κ for the

†Simulations provided by personal communication from Mr. Joo Han Park from Purdue University, West Lafayette, Indiana, USA.

Table 6.2: *Low–LET reference parameters derived from published in vitro and in vivo data. θ and κ are calculated based on these reference parameter values using equations (2.26) and (2.27), respectively. T1, HSG, and V79 data reported by Furusawa et al. (2000), chordoma data by Krämer and Scholz (2000), prostate data by Carlson et al. (2008), and head & neck data by Girinsky et al. (1993) and Stuschke and Thames (1999).*

Cell or tissue type	α_x (Gy^{-1})	β_x (Gy^{-2})	$(\alpha/\beta)_x$ (Gy)	θ (Gbp)	κ (Gbp^2)	θ/κ (Gbp^{-1})	Ref. rad.
T1	0.0305	0.0585	0.52	0.0033	$1.6 \cdot 10^{-3}$	2.15	200 kVp
HSG	0.313	0.0615	5.1	0.0359	$1.6 \cdot 10^{-3}$	21.98	200 kVp
V79	0.184	0.020	9.2	0.0211	$5.3 \cdot 10^{-4}$	39.82	200 kVp
Chordoma	0.1	0.050	2	0.0121	$1.5 \cdot 10^{-3}$	8.25	Co-60
Prostate	0.15	0.048	3.1	0.0181	$1.4 \cdot 10^{-3}$	12.79	Co-60
Head & Neck	0.25	0.025	10	0.0302	$7.3 \cdot 10^{-4}$	41.33	Co-60

clinical conditions, we assumed that all reference radiosensitivity parameters were obtained with Co–60 irradiation. Including a secondary electron spectrum (Hsiao and Stewart 2008), we simulated the reference DSB yield $\Sigma_x = 8.27$ Gy^{-1} Gbp^{-1} with a reference stopping power of $S_x = 0.36$ keV/μm. To represent the nucleus of a cell, we employed a diameter of 5 μm to calculate $\bar{z}_f$ using equation (2.21).

6.2.2 Results

Predicting trends in intrinsic radiosensitivity with particle LET Figure 6.8 shows predicted radiosensitivity parameters for V79, HSG, and T1 cells, for three different ion species (helium–3, carbon–12, and neon–20) over a wide range of LET values. Reference radiosensitivity parameters (table 6.2) were measured using 200 kVp X–rays (Furusawa *et al.* 2000). Model predictions were calculated using equations (2.26) and (2.27). DSB yields were obtained with the MCDS model and the physical properties of the monoenergetic particles were calculated with analytical functions. The predictions are contrasted with measured data points published by Furusawa *et al.* (2000). The model predicts the same trends as the measured data but tends to underestimate α and overestimate β for lower LET values. The measured parameters reach their respective maximum between 100 keV/μm and 250 keV/μm depending on the ion species while the RMF model predicts increasing parameters beyond this point as both Σ and $\bar{z}_f$ increase with LET. For LET values exceeding $\sim$ 150 keV/μm, the model overpredicts α and β.

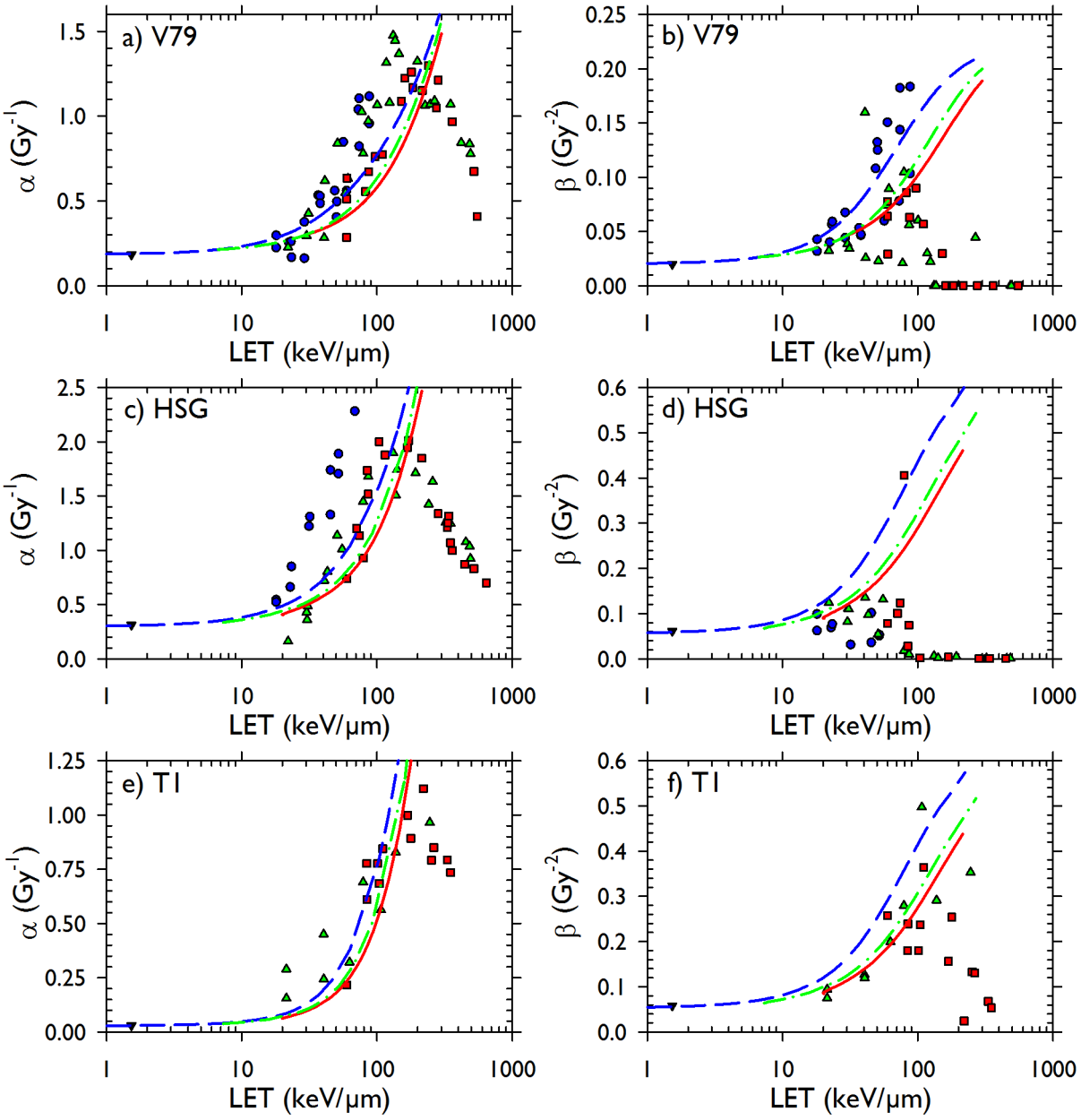

Figure 6.8: *Predictions of α and β as a function of particle LET for He–3 (dashed line), C–12 (dash-dotted line), and Ne–20 (solid line) ions based on a single reference point (triangle) for X–rays. Symbols show measured values of He–3 (circles), C–12 (upward triangle), and Ne–20 (square) derived from cell survival data for V79, HSG, and T1 cells.*

Physical and radiobiological properties of a pristine Bragg peak Modern particle therapy facilities use narrow scanned pencil beams. Figure 6.9 shows α, β, and the DSB yield of a proton and a carbon ion pencil beam with a range of 15 cm in water assuming the radiosensitivity of chordoma tissue. All calculations include depth straggling and an additional depth spectrum created by a 3 mm ripple filter (Weber and Kraft 1999). DSB yields are dose–averaged. α_{D} and β_{D} were calculated using equations (6.11) and (6.12), respectively, and are determined primarily by the DSB yield. This is consistent with the results in figure 6.9. All three curves show a similar shape with a plateau in the entrance channel of the beam. For protons, parameters in the entrance channel equal the reference parameters ($\alpha_{\mathrm{x}} = 0.1$ Gy^{-1}, $\beta_{\mathrm{x}} = 0.05$ Gy^{-2}). For carbon ions, they are increased by ~ 50 %. All values rise sharply as the depth approaches the Bragg peak. The significance of the maximum values must be carefully considered as they are associated with very low doses. Values that coincide with the maximum dose are likely of greater clinical relevance. At the maximum dose, we observe values of $\alpha_{\mathrm{D}} = 0.16$ Gy^{-1} for protons and $\alpha_{\mathrm{D}} = 2.31$ Gy^{-1} for carbon ions, i.e., an increase by a factor of 1.5 and 15, respectively. Similarly, β_{D} increases to values of 0.08 Gy^{-2} and 0.38 Gy^{-2} for protons and carbon ions, respectively.

Physical and radiobiological properties of SOBPs Figure 6.10 shows physical and radiobiological properties of a proton and a carbon SOBP consisting of 17 pencil beams with residual ranges spaced 3 mm apart. The fluence of the pencil beams is optimized such that a constant absorbed dose of 1 Gy is deposited from the proximal edge of the SOBP at 10 cm water equivalent depth to its distal edge at 15 cm. Dose–averaged values of α_{D}, β_{D}, the DSB yield, and LET are calculated from the contributions of the individual pencil beams. Apart from the absorbed dose, all quantities are nearly constant for depths < 10 cm and exhibit the same trends in the SOBP and past the distal edge. At the proximal edge where the first Bragg peak is located, each measure rises to a second plateau and then rises slowly across the width of the SOBP. Approaching the distal edge of the SOBP all quantities rise steeply as they are dominated by the Bragg peak with the greatest range. Dominated by the rise in DSB yield, α_{D} and β_{D} increase by ~ 10 % for protons and ~ 100 % for carbon ions. Across the SOBP, α_{D} increases by another 50 % for protons and > 500 % for carbon ions. The increase in β_{D} is smaller as it depends only on the DSB yield and not particle LET. The relative rise of the latter is considerably steeper at the proximal edge of the SOBP.

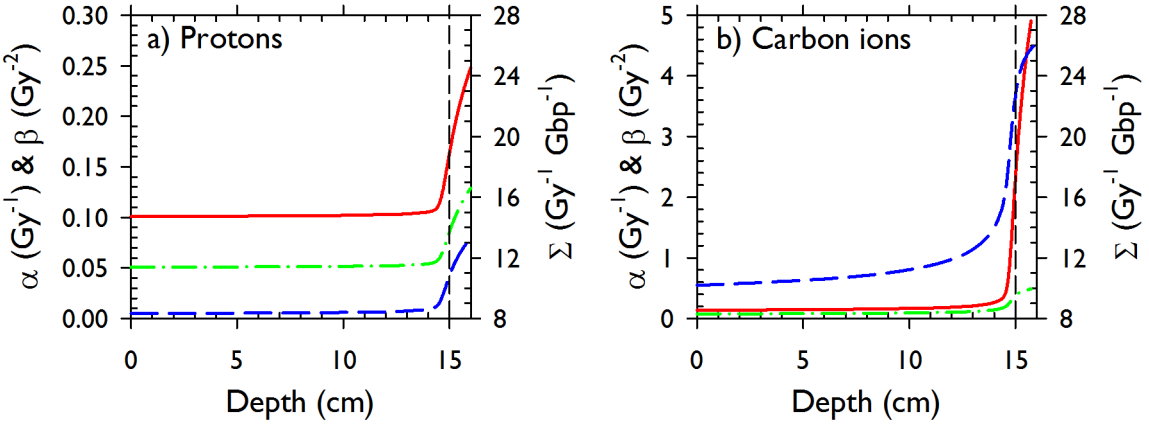

Figure 6.9: *α (solid red), β (dash–dotted green), and the DSB yield Σ (dashed blue) of a pristine proton and a pristine C–12 Bragg peak in chordoma tissue. The range of both Bragg peaks (dashed black) in water is 15 cm.*

Influence of $(\alpha/\beta)_x$ on RBE According to equation (2.32), the tissue dependence of RBE is only reflected in the $(\alpha/\beta)_x$value of the reference parameter set. This dependence is shown in figure 6.11 where the RWD of three tissues with different $(\alpha/\beta)_x$ values (table 6.2) are compared for an SOBP with a constant absorbed dose of 1 Gy. RWD is shown to increase with a decrease in $(\alpha/\beta)_x$. Differences in RBE estimates are as large as 25 % for carbon ions and smaller than 5 % for protons.

Low doses have a high effect on the RBE Figure 6.12 shows predicted RBE values in SOBPs optimized for constant absorbed doses ranging from 0.1 to 10 Gy. RBE estimates are nearly independent of absorbed doses > 2.5 Gy. The carbon ion RBE for lower doses depends up to 50 % on the absorbed dose. For protons, this influence is on the order of 5 %. For particles with higher $(\alpha/\beta)_x$, the impact of dose on RBE estimates is smaller (data not shown). No significant dose dependence is observed outside of the SOBP. Table 6.3 shows RBE values for cell killing for protons and carbon ions for a range of tissue radiosensitivities and physical doses. The average RBE of protons is ~ 1.1 and is nearly independent of dose and $(\alpha/\beta)_x$ while the average carbon ion RBE ranges from $2.0 - 4.5$ for $(\alpha/\beta)_x = 2$ Gy and from $1.9 - 2.5$ for $(\alpha/\beta)_x = 10$ Gy.

Optimizing physical dose to achieve constant biological effect In figures 6.10 to 6.12, a constant physical dose is deposited across the volume covered by the SOBP. Ideally, the true clinical objective in radiotherapy is to deliver a constant biological effect across the tumor volume. Employing the method developed by Wilkens and Oelfke (2006),

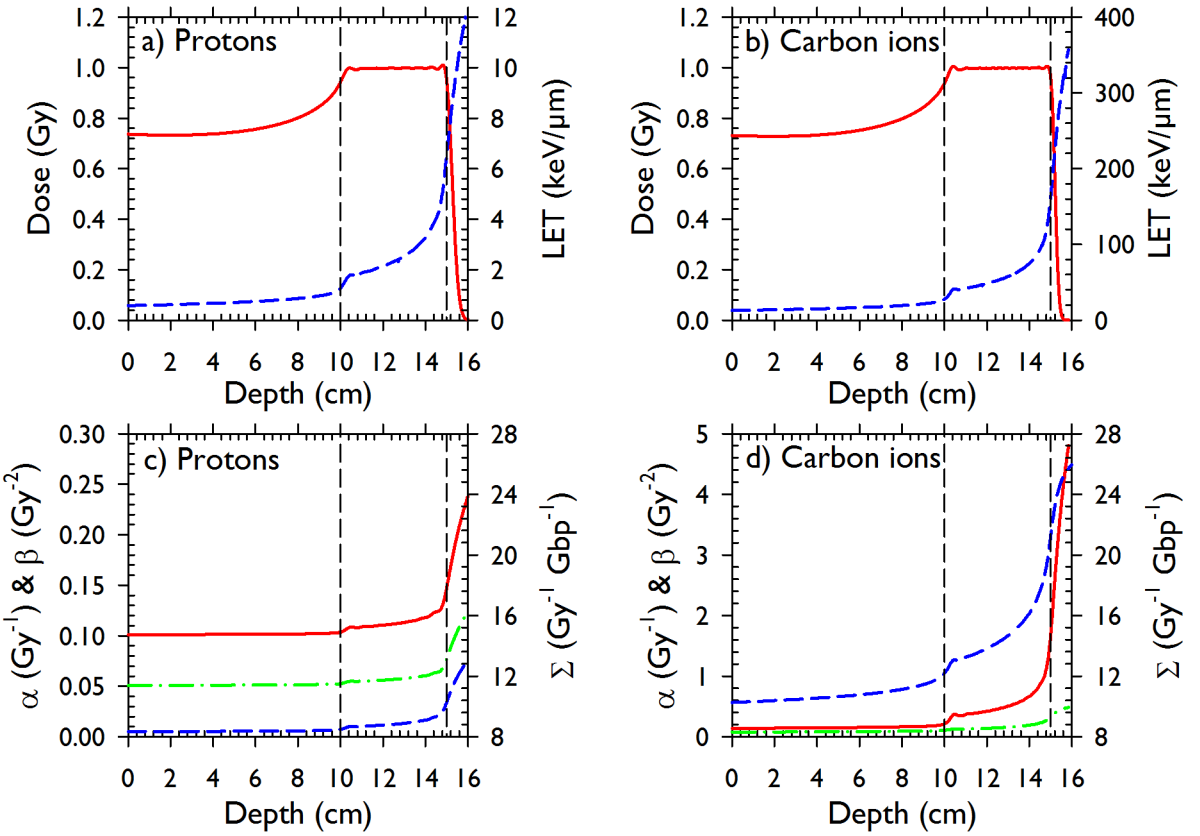

Figure 6.10: *Top row shows the dose (solid red) and LET_d (dashed blue) of a proton and a carbon ion SOBP. α (solid red), β (dash–dotted green), and the DSB yield Σ (dashed blue) of the respective SOBP are displayed in the bottom row. Dashed black lines indicate the extend of the Bragg peak.*

we optimized the RWD for protons and carbon ions for a constant RWD of 3 Gy (RBE). Figure 6.13 shows a relatively flat RWD in the SOBP and the underlying physical doses for both protons and carbon ions. In order to keep the RWD constant across the SOBP, the physical dose must decrease from the proximal to the distal edge. Here, the increase of the RBE with LET reduces the required dose which in turn increases the RBE. Though this effect is more pronounced for carbon ions due to lower doses and higher LET it can also be observed for protons. Comparing the RBE–weighted doses of protons and carbon ions, we found that the entrance to plateau ratio is approximately 2 to 3 for protons and 1 to 3 for carbon ions.

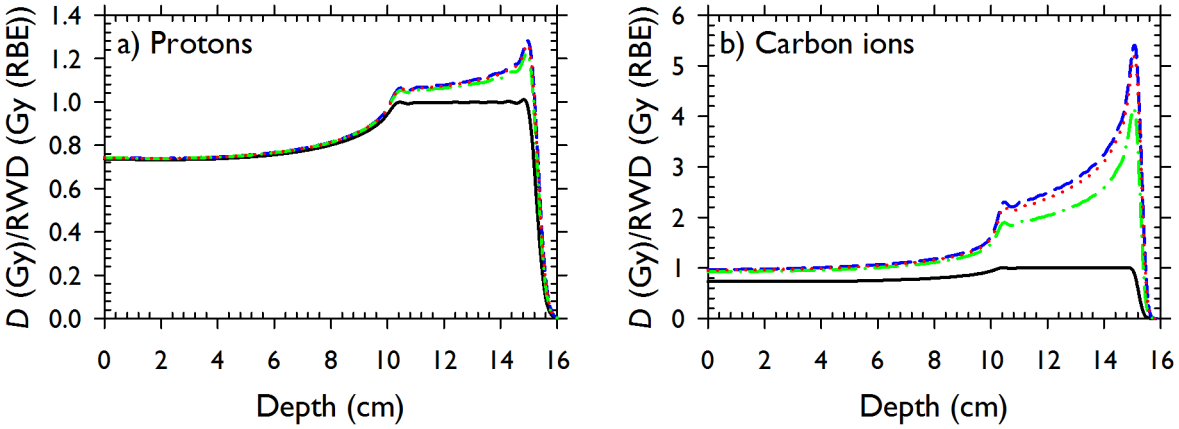

Figure 6.11: *RWD of a proton and a carbon ion SOBP calculated with different biological parameters representing chordoma (dashed blue,* $(\alpha/\beta)_x$= 2 Gy*), prostate (dotted red,* $(\alpha/\beta)_x$= 3 Gy*), and head & neck cancer (dash–dotted green,* $(\alpha/\beta)_x$= 10 Gy*) from the same absorbed dose distribution (solid black).*

6.2.3 Discussion

Predicting radiobiological parameters In its current form, the RMF model tends to overpredict for LET values above $\sim$ 150 keV/μm (figure 6.8). This discrepancy can be attributed to both potential limitations of the RMF model and neglected nuclear fragments. The limitations of the RMF model have been discussed elsewhere (Carlson *et al.* 2008) and model improvements are currently being investigated. The potential overprediction of radiosensitivity for $LET >\sim$ 150 keV/μm does not affect the proton calculations as the LET of therapeutic protons is well below this limit (figure 6.10a). This limitation will introduce uncertainty in the prediction of carbon ion RBE as LET values exceed 150 keV/μm at the position of the Bragg peak (figure 5.4). The proposed approach is therefore expected to overpredict the carbon ion RBE at the distal edge of the SOBP.

The effects of nuclear fragments are neglected in this work and will be investigated in a future study. It is not known how the measurements of the data presented in figure 6.8 were performed but one must consider that any passive means of degrading the beam energy will introduce a spectrum of lighter secondary particles. Most of these fragments will have a lower charge squared to mass ratio than the primary ions and therefore a lower LET and longer range. A real beam with a secondary particle spectrum will therefore produce a reduced biological effect for the same dose compared to the single particle beam assumed here.

Trends in β have been discussed elsewhere (Carlson *et al.* 2008, Carabe-Fernandez *et al.* 2010). We studied the influence of β by replacing it with a constant value equal to the

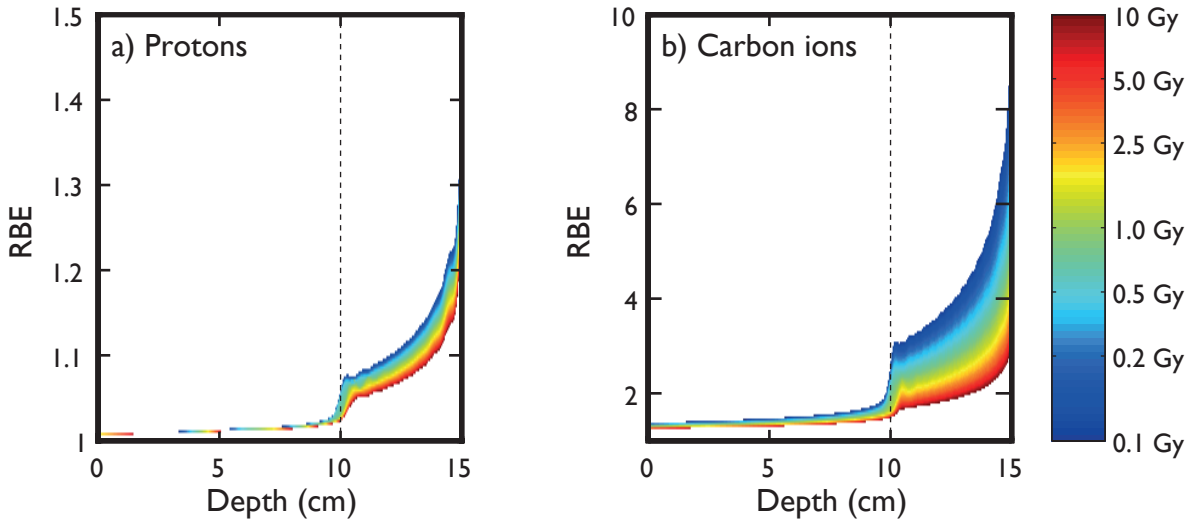

Figure 6.12: *RBE values for chordoma tissue in proton and carbon ion SOBPs ranging from 10 cm (dashed black) to 15 cm for physical doses ranging from* $0.1 - 10$ Gy*.*

reference parameter (data not shown). In chordoma, we observed differences in the RBE of $1-10$ % for protons and $10-20$ % in carbon ions across the SOBP. This is in agreement with recently published findings that the correct choice of β is critical for predicting outcome in proton therapy (Carabe-Fernandez *et al.* 2010).

Good agreement of the proposed approach with measured data can also be found in the observed proton RBE values. The average proton RBE of 1.1 reported for a wide range of tissues and doses (table 6.3, figures 6.11 and 6.12), compares well to the accumulated published data (Paganetti *et al.* 2002). For carbon ions, a greater change in RBE across the SOBP is predicted than obtained using the local effect model (LEM) in clinically implemented settings (Krämer and Scholz 2000, Scholz and Kraft 1996). The LEM model used at the HIT facility in Heidelberg for patient treatment predicts an RBE range of $3 - 3.5$ across a SOBP (Wilkens and Oelfke 2008) which is a significantly smaller range than the $1.8 - 5.4$ reported here. Similar trends in α across a SOBP are found in the recent application of the microdosimetric kinetic model (MKM) for carbon ion treatment planning (Inaniwa *et al.* 2010). The MKM predicts a decrease in α beyond the distal edge of the SOBP, which may be due to more sophisticated modeling of proximity or over–kill effects as well as limitations of using an approximate analytical formula to estimate the frequency–mean specific energy.

Table 6.3: *RBE values for cell killing for protons and carbon ions for a range of tissue radiosensitivities and physical doses. Estimates are shown for the proximal edge (z = 10 cm), distal edge (z = 15 cm), and target average for a clinical SOBP of* 5 cm.

Protons						
Dose	RBE ($(\alpha/\beta)_x$ = 2 Gy)			RBE ($(\alpha/\beta)_x$ = 10 Gy)		
(Gy)	Proximal	Distal	Avg.	Proximal	Distal	Avg.
0.1	1.06	1.44	1.13	1.04	1.28	1.09
0.5	1.06	1.38	1.12	1.04	1.28	1.09
1	1.03	1.34	1.11	1.03	1.27	1.09
2	1.03	1.30	1.10	1.03	1.27	1.09
5	1.02	1.27	1.09	1.02	1.26	1.08
10	1.02	1.26	1.08	1.02	1.25	1.08

Carbon ions						
Dose	RBE ($(\alpha/\beta)_x$ = 2 Gy)			RBE ($(\alpha/\beta)_x$ = 10 Gy)		
(Gy)	Proximal	Distal	Avg.	Proximal	Distal	Avg.
0.1	2.69	10.85	4.48	1.81	5.11	2.49
0.5	2.26	6.74	3.32	1.77	4.59	2.39
1	1.83	5.38	2.82	1.62	4.21	2.29
2	1.60	4.35	2.43	1.53	3.79	2.17
5	1.52	3.44	2.10	1.50	3.28	2.02
10	1.49	3.04	1.96	1.48	2.99	1.93

Radiosensitivity of different tissues Our modeling approach predicts that the RBE depends only on the value of $(\alpha/\beta)_x$. Tissues were purposely chosen to cover a large range of biologically–plausible $(\alpha/\beta)_x$ values. A large dependence on tissue type was not observed for protons, while carbon ion peak RBEs varied by more than 20 % for different tissues. This implies that the largest uncertainties in clinical application will arise for tumors with high $(\alpha/\beta)_x$ values surrounded by healthy tissues with low $(\alpha/\beta)_x$ values. Positional errors in patient setup could also result in larger than expected cell death in healthy tissues as a result of an unexpected increased RBE values. Our results contradict the reasoning of Jäkel *et al.* (2003) that it is safest to use brain tissue with $(\alpha/\beta)_x$ = 2 Gy (van der Kogel 1986) as a lower limit assumption for the RBE in brain tumors. As an $(\alpha/\beta)_x$ value of 2 Gy is at the lower limit of the expected range it returns the most we can expect as RBE i.e. one risks to significantly overestimate the RBE in the target if the $(\alpha/\beta)_x$ value is actually higher.

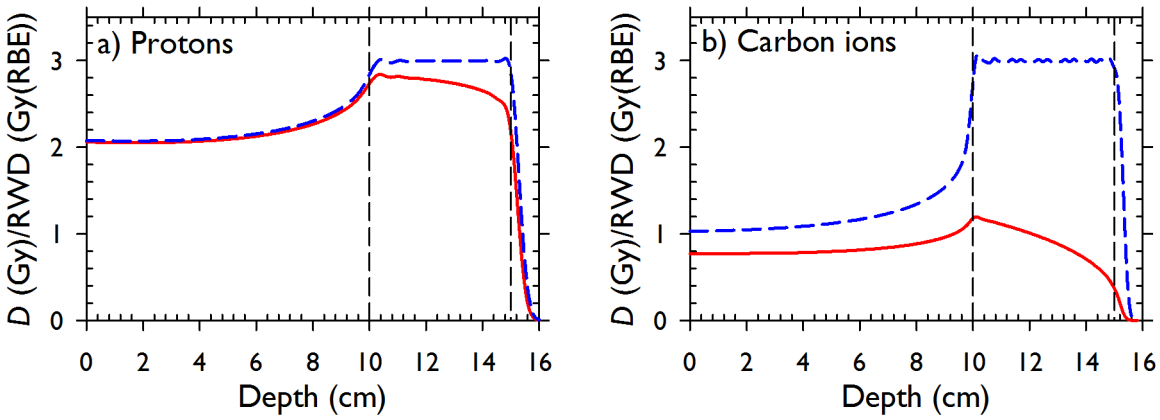

Figure 6.13: *RWD optimized SOBP of protons and carbon ions in chordoma tissue. RWD in dashed blue, absorbed dose in solid red. The extend of the SOBP is indicated by the dashed black line.*

The influence of dose on RBE predictions We observed a considerable dose effect for carbon ions for doses < 2.5 Gy. Most treatments with conventional fractionation schemes employ doses in the range of $0.1 - 1$ Gy (figure 6.12). The dose dependence is on the same order of magnitude as the change of RBE with radiation quality. Wilkens and Oelfke (2008) reported the RBE outside an SOBP peak may be higher than within due to this dose effect. In contrast to their findings, we predict a small dose effect in the normal tissue outside a SOBP (figure 6.12).

Optimization of RWD There is no debate regarding the necessity for the optimization of physical dose to obtain a constant RWD in carbon ion therapy. The results of this study strongly suggest that this approach should also be considered in proton radiotherapy. Our simulations show that RWD can change by up to 30 % across a 5 cm SOBP. RBE values can consistently deviate by more than 10 % from the assumed nominal value of 1.1 in some parts of the SOBP regardless of the tissue and absorbed dose. We also show that the proton RWD is relatively insensitive to tissue radiosensitivity. The potential errors in predicting RBE introduced by assuming the wrong tissue radiosensitivity are likely smaller than the errors introduced by assuming a constant RBE of 1.1.

6.2.4 Conclusions

The proposed approach allows for the quantitative evaluation of the effect of particle LET on DSB induction and cell death in proton and carbon ion radiotherapy. The results of this study indicate the potential for biological hot and cold spots within the SOBP in both

proton and carbon ion radiotherapy. The development of biologically motivated models of RBE results in an enhanced understanding of the biophysical mechanisms underlying cell killing in X–ray and particle therapy, as well as the determination of RBE estimates that can be practically used in charged particle radiotherapy to optimize physical dose for a uniform biological effect. The approach proposed in this paper allows for a robust inclusion of oxygen effects by correcting the DSB yields for oxygen concentration in the MCDS algorithm. Future work is under way to investigate the impact of tumor hypoxia on the relative effectiveness of proton, carbon ion, and X–rays.

Chapter 7

Summary and Conclusions

Before we draw some final conclusions, the main aspects of this thesis shall be briefly summarized. This thesis is divided into two parts. In the first part technical aspects and potential clinical applications of an existing biological effect optimization were studied. Some limitations of radiobiological models were tackled in the second part by introducing an analytical LET model for fragments of heavy ion beams to improve beam quality measures, including oxygen effects into treatment planning, and predicting particle RBE with the recently developed mechanistic RMF model.

Technical aspects of the biological optimization were investigated in chapter 3. It was found that the quadratic objective function employed to minimize the biological effect is only convex for one or two doseburst on a limited domain. For N doseburst we were not able to confirm this result but a non positive definite Hessian of the objective function is a strong indication that the domain has to be kept restricted.
KonRad has the built–in capability to combine multiple radiation modalities in a single treatment plan. Optimization of the dose or effect distribution is in theory independent of the number of radiation modalities. In practice, the highly degenerated D_{ij} matrix reduces the convergence speed or even makes convergence impossible. Two methods were proposed to initialize the optimizer. A simple precalculation of the doseburst weights that ensures that the average actual and prescribed dose/effect are the same has proven to be most efficient.

Clinical application and potential modifications of an existing biological optimization are studied in chapter 4. In the first section 4.1 we compared a variable proton RBE approach to the clinically used generic RBE of 1.1. Dose distributions optimized with a constant RBE were recalculated using a variable proton RBE model (Wilkens and Oelfke

2004). We found significant differences in the RWD distributions depending mostly on the LET distribution and less on the employed radiobiological parameters. We also showed that treatment plans optimized with either a constant or a variable RBE model do not exhibit any significant differences in the RWD distributions calculated with the respective approach.
Section 4.2 demonstrates the simultaneous optimization of carbon ion and photon irradiation. We optimized treatment plans consisting of multiple photon beams and two carbon ion beams. The latter are only used to irradiate a boost volume. It turned out that a simultaneous boost is preferential to a sequential boost in plan quality. A local mixing of radiation modalities ensures steeper dose gradients and simultaneous optimization reduces the integral dose.
The worst case optimization (Pflugfelder *et al.* 2008) was extended from physical to biological optimization in section 4.3. After demonstrating general feasibility we compared worst case optimized treatment plans without any safety margins to plans created with classical safety margins. Each plan was recalculated 98 times assuming range, setup, or both errors of varying magnitude. It was evident that margins in contrast to worst case optimization are an insufficient tool in 3D IMPT to create plans robust against range or setup uncertainties.

An analytical model to calculate the LET of fragments is derived in chapter 5. Analytical models for proton dose (Bortfeld 1997) and LET (Wilkens and Oelfke 2003) were extended to heavier ions. By making several assumptions about the fluence and energy distribution of fragments we could derive equations describing the track– and dose–averaged LET, the fluence, and the dose of each fragment isotope that is a remnant of the primary particles. Depth dose curves calculated with the model agree well with Monte Carlo simulations for primary carbon ions and all its fragments but hydrogen. In contrast to our assumptions secondary protons that are accelerated in nucleon–nucleon interactions have to be considered. It is well known that fragments cannot be neglected due to their dose behind the Bragg peak. Our calculations show that from radiobiological considerations the fragment LET is so high that it cannot be neglected both in front and behind a carbon ion Bragg peak.

Advancing radiobiological models in two different ways is the aim of chapter 6. In section 6.1 a method is introduced to incorporate the radiosensitizing effect of oxygen into treatment planning for carbon ions. We assumed that the influence of the pO_2 on cell survival is a function of the LET. From PET images we inferred the pO_2 in each voxel

and selected the biological input parameters for the optimization now as a function of water equivalent voxel depth, initial beam energy, and pO_2. It is possible to generate dose distributions across tumors with oxygen depleted regions that correspond to a homogeneous RWD even across steep partial oxygen pressure gradients. Unfortunately, we lack access to PET data from which oxygen maps could be derived such that we could test the model in real treatment plans.

Section 6.2 describes how the mechanistic RMF model (Carlson *et al.* 2008) was adapted to predict radiosensitivity parameters and eventually the RBE of realistic proton and carbon ion beams. The RMF predicts LQ parameters α and β as a function of particles given the DSB yield, the LET, and LQ parameters of a reference radiation whose LET and DSB yield are known. In the RMF RBE is only a function of $(\alpha/\beta)_x$ value not the respective individual contributions. RBE is high for lower $(\alpha/\beta)_x$ values i.e. using a low $(\alpha/\beta)_x$ value in target tissues might overestimate the real RBE which is clinically relevant. Our calculations predict a more than 10 % deviation of the RBE of a proton SOBP from the clinical used RBE of 1.1. For protons we could also confirm our previous result that the RBE depends mostly on physical parameters and not on the tissue.

From the specific conclusions that we have made in each section and summarized above the following four general conclusions can be drawn: (1) A well conditioned and well formulated optimization is a key to safe treatment plans of superior quality. (2) The potentials of proton therapy should be exploited by using variable RBE models. (3) RBE may be the wrong concept to quantify radiation damage by particles. (4) Dose painting with particles is feasible.

(1) Employ sophisticated optimization strategies! Optimization is the key concept to improve particle therapy in a timely manner. 3D IMPT treatment plans consisting of thousands of individual dosebursts represent a highly degenerated inverse problem. It is most important to formulate the problem accurately, use a good optimization method, and initialize this method correctly. Many of the daily challenges like range and setup uncertainties, consideration of doses from other radiation modalities, let alone the variable radiation biology are too complex to be included inherently by the treatment planner. It seems to be evident that the regular (biological) optimization algorithms generate treatment plans that cannot be made robust against range and setup uncertainties by simply adding margins to target volumes. Worst case optimization creates more robust plans with less integral dose. Carbon ions and photons may never be applied within one fraction in the clinics. Nevertheless, our investigations have shown that correct initialization and simultaneous optimization are key features that can drastically improve plan quality. And

if we know the local radiosensitivity (an implicit assumption we make all the time, not only when we consider hypoxia) only an optimization routine will be able to exploit all the potential benefits.

(2) Investigate the radiobiological potential of protons! Treatment planning for protons should employ variable RBE models. From our investigations comparing different radiosensitivity parameters for the same volume we observed only little differences. Large differences among constant and variable RBE are always correlated with high LET values. Today the local LET distribution is completely neglected in proton therapy treatment planning. As a starting point one could design treatment plans of sufficient quality when calculated with either constant or variable RBE.

(3) Get rid of RBE! RBE is a tempting concept. It promises to convert a particle dose whose biological effect depends on so many parameters into an equivalent low–LET photon dose that we are used to. The product of RBE and dose seems to be something physical and measurable like absorbed photon dose though it is not. The corresponding photon dose is completely unphysical. Each voxel's dose by itself could be delivered but the distribution as a whole cannot be created with photons. Additionally, RBE does not account for fractionation effects. This is frequently neglected especially when comparing simultaneous and sequential boost schemes. RBE may also be a misleading concept. The clinical implementation of the local effect model predicts the lowest RBE values in the target region and the highest outside. But this does not allow to judge the quality of the plan. Low RBE values are not equivalent to a low biological effect. Nevertheless, if the RBE decreases from entrance to target region the absorbed dose has to increase at a higher proportion to make the distribution beneficial i.e. physics has to outweigh biology. And last but not least the term "relative biological effectiveness" by itself is questionable. Though radiation biology is a relatively unexplored field it is well known that the initial radiation damage depends purely on physical interactions and not on the cell while the biological repair processes are cell and not radiation specific. Hence, the term "relative physical effectiveness" might be more appropriate. It would be a good start to think in terms of the biological effect instead of RBE and RBE–weighted dose.

(4) Pursue active dose painting with particles! At first we should acknowledge that in particle therapy dose painting is performed in every single treatment plan. By prescribing an RBE–weighted dose the underlying physical dose distribution is not defined. It is chosen by the optimizer and depends solely on the biological model. The dose varies

from one voxel to another in a fashion that is uncontrolled by the treatment planner. To do so we trust radiobiological models that are afflicted with large errors i.e. we are doing dose painting just not by numbers. Instead of employing the information of functional images we trust the visual conception of a physician. Nevertheless, the treatments have a high rate of success which means that either the models are better than we think or the therapeutic ratio is larger than expected. Assuming that the latter is correct means that there may be a range of doses that can be used without increasing the risk for the patient. This dose range could be explored by locally varying the dose based on functional images. Dose painting by numbers would detach the dose prescription from a single person's action and instead offer the chance to systematically evaluate treatment outcome.

All the arguments we have made above have a tendency to reduce human interaction into the treatment planning process. Eventually, the treatment planner should define the goals and let the treatment planning system choose the best options.

Appendix

A Low and high dose limits of the RBE in the RMF model

For a low LET reference radiation with LQ parameters α_x and β_x the RBE in the RMF model is given by (equation (2.32))

$$RBE_\mathrm{RMF} = \frac{1}{2D}\left[\sqrt{\left[\left(\frac{\alpha}{\beta}\right)_\mathrm{x} + 2D\frac{\Sigma}{\Sigma_\mathrm{x}}\right]^2 + \frac{8D}{\Sigma_\mathrm{x}^2}\left(\bar{z}_\mathrm{f}\Sigma^2 - \bar{z}_\mathrm{f,x}\Sigma_\mathrm{x}\Sigma\right)} - \left(\frac{\alpha}{\beta}\right)_\mathrm{x}\right] \tag{A.1}$$

where Σ_x, Σ and $\bar{z}_\mathrm{f,x}$, $\bar{z}_\mathrm{f}$ are the DSB yield and the frequncy–mean specific energy of the reference radiation and the test radiation, respectively. For very high doses ($D \gg \alpha/\beta$) and very low doses ($D \ll \alpha/\beta$) the RBE has to be proportional to $\sqrt{\beta/\beta_\mathrm{x}}$ and α/α_x, respectively.
The high dose limit $D \to \infty$ the RBE_RMF is proportional to

$$\lim_{D\to\infty} RBE_\mathrm{RMF} \propto \frac{1}{2D}\left[\left(\frac{\alpha}{\beta}\right)_\mathrm{x} + 2D\frac{\Sigma}{\Sigma_\mathrm{x}} - \left(\frac{\alpha}{\beta}\right)_\mathrm{x}\right] \tag{A.2}$$

$$= \frac{\Sigma}{\Sigma_\mathrm{x}} \tag{A.3}$$

$$= \frac{1}{\sqrt{\beta_\mathrm{x}}}\frac{\Sigma}{\Sigma_\mathrm{x}}\sqrt{\beta_\mathrm{x}} \tag{A.4}$$

$$= \sqrt{\beta/\beta_\mathrm{x}} \tag{A.5}$$

Here, we used that in the RMF model β scales with the squared ratio of Σ and Σ_x (cf. equation (2.31)). The low dose limit $D \to 0$ cannot be inferred directly from equation (A.1) as both the numerator and the denominator are going towards 0. Hence, we can make use of L'Hôpital's rule (Königsberger 2001, and many other basic calculus textbooks). It states

that if $\lim_{x\to c} f(x) = \lim_{x\to c} g(x) = 0$ or $\pm\infty$ and the derivatives of f and g exist then

$$\lim_{x\to c} \frac{f(x)}{g(x)} = \lim_{x\to c} \frac{f'(x)}{g'(x)}. \tag{A.6}$$

Here, we identify

$$f(D) = \sqrt{\left[\left(\frac{\alpha}{\beta}\right)_{\mathrm{x}} + 2D\frac{\Sigma}{\Sigma_{\mathrm{x}}}\right]^2 + \frac{8D}{\Sigma_{\mathrm{x}}^2}\left(\bar{z}_{\mathrm{f}}\Sigma^2 - \bar{z}_{\mathrm{f,x}}\Sigma_{\mathrm{x}}\Sigma\right)} - \left(\frac{\alpha}{\beta}\right)_{\mathrm{x}} \tag{A.7}$$

$$g(D) = 2D. \tag{A.8}$$

The derivatives of f and g with respect to D are

$$f'(D) = \left(\left[\left(\frac{\alpha}{\beta}\right)_{\mathrm{x}} + 2D\frac{\Sigma}{\Sigma_{\mathrm{x}}}\right]^2 + \frac{8D}{\Sigma_{\mathrm{x}}^2}\left(\bar{z}_{\mathrm{f}}\Sigma^2 - \bar{z}_{\mathrm{f,x}}\Sigma_{\mathrm{x}}\Sigma\right)\right)^{-1/2} \cdot \frac{1}{2}\left(4\frac{\Sigma}{\Sigma_{\mathrm{x}}}\left[\left(\frac{\alpha}{\beta}\right)_{\mathrm{x}} + 2D\frac{\Sigma}{\Sigma_{\mathrm{x}}}\right] + \frac{8}{\Sigma_{\mathrm{x}}^2}\left(\bar{z}_{\mathrm{f}}\Sigma^2 - \bar{z}_{\mathrm{f,x}}\Sigma_{\mathrm{x}}\Sigma\right)\right) \tag{A.9}$$

and

$$g'(D) = 2. \tag{A.10}$$

For the limit of $D \to 0$

$$\lim_{D\to 0} \frac{f'(D)}{g'(D)} = \left(\frac{\alpha}{\beta}\right)_{\mathrm{x}}^{-1}\left(\frac{\Sigma}{\Sigma_{\mathrm{x}}}\left(\frac{\alpha}{\beta}\right)_{\mathrm{x}} + \frac{2}{\Sigma_{\mathrm{x}}^2}\left(\bar{z}_{\mathrm{f}}\Sigma^2 - \bar{z}_{\mathrm{f,x}}\Sigma_{\mathrm{x}}\Sigma\right)\right) \tag{A.11}$$

$$= \frac{\Sigma}{\Sigma_{\mathrm{x}}} + \frac{\beta_{\mathrm{x}}}{\alpha_{\mathrm{x}}}\frac{2}{\Sigma_{\mathrm{x}}^2}\left(\bar{z}_{\mathrm{f}}\Sigma^2 - \bar{z}_{\mathrm{f,x}}\Sigma_{\mathrm{x}}\Sigma\right) \tag{A.12}$$

$$= \frac{\frac{\Sigma}{\Sigma_{\mathrm{x}}}\left(\alpha_{\mathrm{x}} + \frac{2}{\Sigma_{\mathrm{x}}}\left(\bar{z}_{\mathrm{f}}\Sigma - \bar{z}_{\mathrm{f,x}}\Sigma_{\mathrm{x}}\right)\right)}{\alpha_{\mathrm{x}}} \tag{A.13}$$

$$= \frac{\alpha}{\alpha_{\mathrm{x}}} \tag{A.14}$$

For the last step we used equation (2.26) that defines the scaling of α with changing radiation quality.

B Range straggling width for ions

The straggling width for heavy ions can be determined in the same way as the straggling width for protons (Bortfeld 1997). Following the method by Bethe and Ashkin (1953) the width σ_{E} of the energy spectrum of a heavy ion beam due to nuclear interactions is approximated by Bohr's classical formula

$$\frac{\mathrm{d}}{\mathrm{d}z}\left(\sigma_{\mathrm{E}}^2\right) \approx \frac{1}{4\pi\epsilon_0^2} e^2 NZ Z_{\mathrm{hi}}^2 \tag{B.1}$$

where NZ is the electron density, e the charge of the electron, ϵ_0 the vacuum permittivity and Z_{hi} the charge of the ion. This width can be transformed into a depth spectrum width σ by

$$\sigma^2 = \int_0^{R_{\mathrm{hi},0}} \mathrm{d}z \, \frac{\mathrm{d}}{\mathrm{d}z}\left(\sigma_{\mathrm{E}}^2\right) \left(\frac{\mathrm{d}E}{\mathrm{d}z}\right)^{-2} \tag{B.2}$$

where $-\mathrm{d}E/\mathrm{d}z$ is the stopping power of the ion with residual range $R_{\mathrm{hi},0}$. The stopping power can be obtained by solving equation (2.6) for E and taking its negative derivative with respective to z

$$-\frac{\mathrm{d}E}{\mathrm{d}z} = \frac{1}{p} \alpha_{\mathrm{hi}}^{-1/p} \left(R_{\mathrm{hi},0} - z\right)^{1/p-1} . \tag{B.3}$$

The solution for the integral in equation (B.2) is given by

$$\sigma^2 = \frac{1}{Z_{\mathrm{hi}}^{4/p-2} A_{\mathrm{hi}}^{2-2/p}} \cdot \frac{e^4 NZ}{4\pi\epsilon_0^2} \cdot \frac{p^2 \alpha_p^{2/p}}{3-2/p} {R_{\mathrm{hi},0}}^{3-2/p}. \tag{B.4}$$

The same equation can be used to obtain the straggling width of fragments.

C The solution of the stopping power integral for fragments

Next we will demonstrate how to solve integrals of the type

$$I\left(z\right) = \int_{z'_{\mathrm{low}}}^{z'_{\mathrm{max}}} \mathrm{d}z' \int_{-\infty}^{R_{\mathrm{f},z'}+z'} \mathrm{d}\bar{z} \; q\left(\bar{z}, z'\right)^x \exp\left(-\frac{\left(z-\bar{z}\right)^2}{2\sigma_{\mathrm{f,max}}^2}\right) \tag{C.5}$$

where we identify $q = \lambda_{\mathrm{f}}^{\mathrm{hi}}\left(R_{\mathrm{hi},0} - z\right) - \left(\bar{z} - z'\right)$. Performing variable transformtion we yield

$$I\left(z\right) = \int_{z'_{\mathrm{low}}}^{z'_{\mathrm{max}}} \mathrm{d}z' \int_0^{\infty} \mathrm{d}q\; q^{-\nu-1} \exp\left(-\frac{\left(q-s\right)^2}{2\sigma_{\mathrm{f,max}}^2}\right) \tag{C.6}$$

using $s = \lambda_{\mathrm{f}}^{\mathrm{hi}} R_{\mathrm{hi},0} - z - z'\left(\lambda_{\mathrm{f}}^{\mathrm{hi}} - 1\right)$ and $\nu = -x - 1$. We evaluate the inner integral using the parabolic cylinder function $D_\nu\left(x\right)$ and the Gamma function $\Gamma\left(x\right)$ (Wilkens 2004)

$$I\left(z\right) = \sigma_{\mathrm{f,max}}^{-\nu}\Gamma\left(-\nu\right) \int_{z'_{\mathrm{low}}}^{z'_{\mathrm{max}}} \mathrm{d}z'\; \exp\left(-s^2/4\sigma_{\mathrm{f,max}}^2\right) D_\nu\left(-\frac{s}{\sigma_{\mathrm{f,max}}}\right) \tag{C.7}$$

To solve this integral we perform another variable transformation using $y = -s/\sigma_{\mathrm{f,max}}$. The three different integration limits are

$$y\left(z' = 0\right) = \left[z - \lambda_{\mathrm{f}}^{\mathrm{hi}} R_{\mathrm{hi},0}\right]/\sigma_{\mathrm{f,max}} = \chi \tag{C.8}$$

$$y\left(z' = z\right) = \left[\lambda_{\mathrm{f}}^{\mathrm{hi}}\left(z - R_{\mathrm{hi},0}\right)\right]/\sigma_{\mathrm{f,max}} = \xi \tag{C.9}$$

$$y\left(z' = \left(\lambda_{\mathrm{f}}^{\mathrm{hi}} R_{\mathrm{hi},0} - z\right)/\left(\lambda_{\mathrm{f}}^{\mathrm{hi}} - 1\right)\right) = 0 \tag{C.10}$$

According to Mathematica equation (C.7) can be evaluated analytically. The result is given by

$$\begin{aligned} I\left(y\right) = t \Bigg[& \frac{y}{\Gamma\left(\frac{1}{2}\left(1-\nu\right)\right)}\; {}_1F_1\left(\frac{\nu+1}{2}; \frac{3}{2}; -\frac{y^2}{2}\right) + \\ & \frac{\sqrt{2}}{\Gamma\left(1-\frac{\nu}{2}\right)}\left({}_1F_1\left(\frac{\nu}{2}; \frac{1}{2}; -\frac{y^2}{2}\right) - 1\right)\Bigg]_{y_{\mathrm{low}}}^{y_{\mathrm{max}}}. \end{aligned} \tag{C.11}$$

Here, ${}_1F_1\left(a; b; c\right)$ is the confluent hypergeometric function of the first kind and

$$t = \sqrt{\pi} 2^{\nu/2} \sigma^{1-\nu} \Gamma\left(-\nu\right)\left(\lambda_{\mathrm{f}}^{\mathrm{hi}} - 1\right)^{-1}. \tag{C.12}$$

The above equation can be simplified using the identities

$$ {}_1F_1\left(a;\frac{1}{2};-\frac{x^2}{2}\right)-\frac{2\sqrt{-x}}{\Gamma\left(\frac{1}{2}-a\right)}\Gamma\left(1-a\right)\ {}_1F_1\left(a+\frac{1}{2};\frac{3}{2};x\right)= \\ \pi^{-1/2}2^{1-2a}\mathrm{e}^{x}\Gamma\left(1-a\right)H_{2a-1}\left(\sqrt{-x}\right) \tag{C.13} $$

and

$$ H_d\left(v\right)=2^{d/2}\mathrm{e}^{v^2/2}D_d\left(\sqrt{2}v\right) \tag{C.14} $$

where $H_d\left(v\right)$ is the Hermite function. The simplifiaction yields

$$ I\left(y\right)=\Gamma\left(-\nu\right)\frac{\sigma^{1-\nu}}{1-\lambda_{\mathrm{f}}^{\mathrm{hi}}}\left[\mathrm{e}^{-y^2/4}D_{\nu-1}\left(y\right)\right]_{y_{\min}}^{y_{\max}}. \tag{C.15} $$

The solution of the integral with the integration limits for the respective case is

$$ I\left(z\right)=\frac{\sigma_{\mathrm{f,max}}^{1-\nu}\Gamma\left(-\nu\right)}{1-\lambda_{\mathrm{f}}^{\mathrm{hi}}}\begin{cases}\mathrm{e}^{-\xi^2/4}D_{\nu-1}\left(\xi\right)-\mathrm{e}^{-\chi^2/4}D_{\nu-1}\left(\chi\right) & \text{i) and iii)}\\ \frac{\sqrt{\pi}2^{\nu/2}}{\Gamma\left(\frac{1-\nu}{2}\right)}-\mathrm{e}^{-\chi^2/4}D_{\nu-1}\left(\chi\right) & \text{ii)}\\ \mathrm{e}^{-\xi^2/4}D_{\nu-1}\left(\xi\right)-\frac{\sqrt{\pi}2^{\nu/2}}{\Gamma\left(\frac{1-\nu}{2}\right)} & \text{iv).}\end{cases} \tag{C.16} $$

Here, we used the identity $D_\nu\left(0\right)=\sqrt{\pi}2^{\nu/2}\ \Gamma\left(\frac{1-\nu}{2}\right)^{-1}$.

Bibliography

Alber M., Paulsen F., Eschmann S.M. and Machulla H.J. 2003 On biologically conformal boost dose optimization. *Physics in Medicine and Biology* **48**(2) N31–N35.

Alper T. and Howard-Flanders P. 1956 Role of Oxygen in Modifying the Radiosensitivity of E. Coli B. *Nature* **178**(4540) 978–979.

Ando K. and Kase Y. 2009 Biological characteristics of carbon-ion therapy. *International Journal of Radiation Biology* **85**(9) 715–728.

Barendsen G.W., Koot C.J., Kersen G.R.V., Bewley D.K., Field S.B. and Parnell C.J. 1966 The effect of oxygen on impairment of the proliferative capacity of human cells in culture by ionizing radiations of different LET. *International Journal of Radiation Biology and Related Studies in Physics, Chemistry, and Medicine* **10**(4) 317–27.

Benitsch T. 2005 *Monte-Carlo-Simulation der Dosisverteilung eines therapeuti-schen Kohlenstoff-Ionenstrahls mithilfe von GEANT4.* Diploma thesis, University of Heidelberg.

Bentzen S.M. 2005 Theragnostic imaging for radiation oncology: dose-painting by numbers. *The Lancet Oncology* **6**(2) 112–117.

Bethe H. 1930 Zur Theorie des Durchgangs schneller Korpuskularstrahlen durch Materie. *Annalen der Physik* **397** 325–400.

Bethe H. and Ashkin J. 1953 Passage of radiations through matter. In: Segre E. (editor), *Experimental Nuclear Physics*, volume 1. New York: Wiley.

Bortfeld T. 1997 An analytical approximation of the Bragg curve for therapeutic proton beams. *Medical Physics* **24**(12) 2024–2033.

— 2006 IMRT: a review and preview. *Physics in Medicine and Biology* **51**(13) R363–R379.

Bortfeld T. and Schlegel W. 1996 An analytical approximation of depth-dose distributions for therapeutic proton beams. *Physics in Medicine and Biology* **41**(8) 1331–1339.

Boyd S.P. and Vandenberghe L. 2004 *Convex Optimization.* Cambridge, UK: Cambridge University Press.

Brahme A., Källman P. and Lind B.K. 1989 Optimization of proton and heavy ion therapy using an adaptive inversion algorithm. *Radiotherapy and Oncology* **15**(2) 189–197.

Butts J.J. and Katz R. 1967 Theory of RBE for heavy ion bombardment of dry enzymes and viruses. *Radiation Research* **30**(4) 855–71.

Carabe-Fernandez A., Dale R.G., Hopewell J.W., Jones B. and Paganetti H. 2010 Fractionation effects in particle radiotherapy: implications for hypo-fractionation regimes. *Physics in Medicine and Biology* **55**(19) 5685–5700.

Carlson D.J. 2006 *Mechanisms of Intrinsic Radiation Sensitivity: The effects of DNA damage repair, oxygen, and radiation quality.* Ph.D. thesis, Purdue University, West Lafayette, Indiana.

Carlson D.J., Keall P.J., Jr. B.W.L., Chen Z.J. and Brown J.M. 2011 Hypofractionation Results in Reduced Tumor Cell Kill Compared to Conventional Fractionation for Tumors With Regions of Hypoxia. *International Journal of Radiation Oncology*Biology*Physics* **79**(4) 1188–1195.

Carlson D.J., Stewart R.D., Li X.A., Jennings K., Wang J.Z. and Guerrero M. 2004 Comparison of in vitro and in vivo ratios for prostate cancer. *Physics in Medicine and Biology* **49**(19) 4477–4491.

Carlson D.J., Stewart R.D. and Semenenko V.A. 2006 Effects of oxygen on intrinsic radiation sensitivity: A test of the relationship between aerobic and hypoxic linear-quadratic (LQ) model parameters. *Medical Physics* **33**(9) 3105–3115.

Carlson D.J., Stewart R.D., Semenenko V.A. and Sandison G.A. 2008 Combined Use of Monte Carlo DNA Damage Simulations and Deterministic Repair Models to Examine Putative Mechanisms of Cell Killing. *Radiation Research* **169**(4) 447–459.

Chang J., Wen B., Kazanzides P., Zanzonico P., Finn R.D., Fichtinger G. and Ling C.C. 2009 A robotic system for 18F-FMISO PET-guided intratumoral pO2 measurements. *Medical Physics* **36**(11) 5301–5309.

Chen G.T., Singh R.P., Castro J.R., Lyman J.T. and Quivey J.M. 1979 Treatment planning for heavy ion radiotherapy. *International Journal of Radiation Oncology*Biology*Physics* **5**(10) 1809–1819.

Combs S.E., Ellerbrock M., Haberer T., Habermehl D., Hoess A., Jäkel O., Jensen A., Klemm S., Münter M., Naumann J., Nikoghosyan A., Oertel S., Parodi K., Rieken S. and Debus J. 2010 Heidelberg Ion Therapy Center (HIT): Initial clinical experience in the first 80 patients. *Acta Oncologica* **49**(7) 1132–1140.

Cronqvist A. 1995 *Quantification of the Response of Hetergeneous Tumours and Organized Normal Tissues to Fractionated Radiotherapy.* Doctoral dissertation, Stockholm University, Stockholm.

Curtis S.B. 1986 Lethal and potentially lethal lesions induced by radiation – a unified repair model. *Radiation Research* **106**(2) 252–270.

Eisbruch A., Haken R.K.T., Kim H.M., Marsh L.H. and Ship J.A. 1999 Dose, volume, and function relationships in parotid salivary glands following conformal and intensity-modulated irradiation of head and neck cancer. *International Journal of Radiation Oncology*Biology*Physics* **45**(3) 577–587.

Elsässer T. and Scholz M. 2007 Cluster effects within the local effect model. *Radiation Research* **167**(3) 319–329.

Elsässer T., Weyrather W.K., Friedrich T., Durante M., Iancu G., Krämer M., Kragl G., Brons S., Winter M., Weber K. and Scholz M. 2010 Quantification of the relative biological effectiveness for ion beam radiotherapy: direct experimental comparison of proton and carbon ion beams and a novel approach for treatment planning. *International Journal of Radiation Oncology*Biology*Physics* **78**(4) 1177–1183.

Flynn R.T., Bowen S.R., Bentzen S.M., Mackie T.R. and Jeraj R. 2008 Intensity-modulated x-ray (IMXT) versus proton (IMPT) therapy for theragnostic hypoxia-based dose painting. *Physics in Medicine and Biology* **53**(15) 4153–4167.

Fredriksson A., Forsgren A. and rdemark B.H. 2011 Minimax optimization for handling range and setup uncertainties in proton therapy. *Medical Physics* **38**(3) 1672.

Frese M.C. 2007 *Investigations on Fast Biological Treatment Planning for Heavy Ion Therapy: Aspects of Employed Models and Algorithms*. Diploma thesis, University of Heidelberg, Heidelberg.

Frese M.C., Wilkens J.J., Huber P.E., Jensen A.D., Oelfke U. and Taheri-Kadkhoda Z. 2011a Application of Constant vs. Variable Relative Biological Effectiveness in Treatment Planning of Intensity-Modulated Proton Therapy. *International Journal of Radiation Oncology*Biology*Physics* **79**(1) 80–88.

Frese M.C., Yu V.K., Stewart R.D. and Carlson D.J. 2011b A mechanism-based approach to predict the relative biological effectiveness (RBE) of protons and carbon ions in radiation therapy. *submitted to IJROBP* .

Furusawa Y., Fukutsu K., Aoki M., Itsukaichi H., Eguchi-Kasai K., Ohara H., Yatagai F., Kanai T. and Ando K. 2000 Inactivation of Aerobic and Hypoxic Cells from Three Different Cell Lines by Accelerated (3)He-, (12)C- and (20)Ne-Ion Beams. *Radiation Research* **154**(5) 485–496.

Girinsky T., Lubin R., Pignon J., Chavaudra N., Gazeau J., Dubray B., Cosset J., Socie G. and Fertil B. 1993 Predictive value of in vitro radiosensitivity parameters in head and neck cancers and cervical carcinomas: Preliminary correlations with local control and overall survival. *International Journal of Radiation Oncology*Biology*Physics* **25**(1) 3–7.

Gottschalk B., Koehler A., Schneider R., Sisterson J. and Wagner M. 1993 Multiple Coulomb scattering of 160 MeV protons. *Nuclear Instruments and Methods in Physics Research Section B: Beam Interactions with Materials and Atoms* **74**(4) 467–490.

Grassberger C., Trofimov A., Lomax A. and Paganetti H. 2010 Variations in Linear Energy Transfer Within Clinical Proton Therapy Fields and the Potential for Biological Treatment Planning. *International Journal of Radiation Oncology, Biology, Physics* .

Grosu A., Souvatzoglou M., Röper B., Dobritz M., Wiedenmann N., Jacob V., Wester H., Reischl G., Machulla H., Schwaiger M., Molls M. and Piert M. 2007 Hypoxia imaging with FAZA-PET and theoretical considerations with regard to dose painting for individualization of radiotherapy in patients with head and neck cancer. *International Journal of Radiation Oncology*Biology*Physics* **69**(2) 541–551.

Gunzert-Marx K., Iwase H., Schardt D. and Simon R.S. 2008 Secondary beam fragments produced by 200 MeV/u 12C ions in water and their dose contributions in carbon ion radiotherapy. *New Journal of Physics* **10**(7) 075003.

Haberer T., Becher W., Schardt D. and Kraft G. 1993 Magnetic scanning system for heavy ion therapy. *Nuclear Instruments and Methods in Physics Research Section A: Accelerators, Spectrometers, Detectors and Associated Equipment* **330**(1-2) 296–305.

Highland V.L. 1975 Some practical remarks on multiple scattering. *Nuclear Instruments and Methods* **129**(2) 497–499.

Honoré H.B., Bentzen S.M., ller K.M. and Grau C. 2002 Sensori-neural hearing loss after radiotherapy for nasopharyngeal carcinoma: individualized risk estimation. *Radiotherapy and Oncology* **65**(1) 9–16.

Hsiao Y. and Stewart R.D. 2008 Monte Carlo simulation of DNA damage induction by x-rays and selected radioisotopes. *Physics in Medicine and Biology* **53**(1) 233–244.

ICRU 1983 *Microdosimetry (ICRU Report 36).* Bethesda, MD.: International Commission on Radiation Units and Measurements (ICRU).

— 1993 *Stopping Powers and Ranges for Protons and Alpha Particles (ICRU Report 49).* Bethesda, MD.: International Commission on Radiation Units and Measurements (ICRU).

— 2007 *Prescribing, Recording, and Reporting Proton-Beam Therapy (ICRU Report78).* Bethesda, MD.: International Commission on Radiation Units and Measurements (ICRU).

Inaniwa T., Furukawa T., Kase Y., Matsufuji N., Toshito T., Matsumoto Y., Furusawa Y. and Noda K. 2010 Treatment planning for a scanned carbon beam with a modified microdosimetric kinetic model. *Physics in Medicine and Biology* **55**(22) 6721–6737.

Jäkel O. 2006 Ranges of ions in metals for use in particle treatment planning. *Physics in Medicine and Biology* **51**(9) N173–177.

Jäkel O., Schule–Ertner D., Karger C.P., Nikoghosyan A. and Debus J. 2003 Heavy ion therpay: status and perspectives. *Technology in Cancer Research & Treatment* **2**(5) 377–87.

Johns H.E. and Cunningham J.R. 1983 *Physics of Radiology, Fourth Edition.* Charles C. Thomas Publisher, 4 sub edition.

Kellerer A.M. and Rossi H.H. 1978 A generalized formulation of dual radiation action. *Radiation Research* **75** 471–88.

Königsberger K. 2001 *Analysis 1.* Berlin: Springer.

Kraft G. 1987 Radiobiological effects of very heavy ions: inactivation, induction of chromosome aberrations and strand breaks. *Nucl. Sci. Appl.* **3** Pages: 1–28.

Krämer M., Jäkel O., Haberer T., Kraft G., Schardt D. and Weber U. 2000 Treatment planning for heavy-ion radiotherapy: physical beam model and dose optimization. *Physics in Medicine and Biology* **45**(11) 3299–3317.

Krämer M. and Scholz M. 2000 Treatment planning for heavy-ion radiotherapy: calculation and optimization of biologically effective dose. *Physics in Medicine and Biology* **45**(11) 3319–3330.

— 2006 Rapid calculation of biological effects in ion radiotherapy. *Physics in Medicine and Biology* **51**(8) 1959–1970.

Lof J., Lind B.K. and Brahme A. 1995 Optimal radiation beam profiles considering the stochastic process of patient positioning in fractionated radiation therapy. *Inverse Problems* **11**(6) 1189–1209.

Lomax A. 1999 Intensity modulation methods for proton radiotherapy. *Physics in Medicine and Biology* **44**(1) 185–205.

Lomax A., Pedroni E., Schaffner B., Scheib S., Schneider U. and Tourovsky A. 1996 3D treatment planning for conformal proton therapy by spot scanning. *Quantitative Imaging in Oncology* 67—71.

Lomax A.J. 2008 Intensity modulated proton therapy and its sensitivity to treatment uncertainties: the potential effects of calculational uncertainties. *Physics in Medicine and Biology* **53**(4) 1027–1042.

Lühr A., Hansen D.C., Jäkel O., Sobolevsky N. and Bassler N. 2011 Analytical expressions for water-to-air stopping-power ratios relevant for accurate dosimetry in particle therapy. *Physics in Medicine and Biology* **56**(8) 2515–2533.

Malinen E., Sovik A., Hristov D., Bruland O.S. and Olsen D.R. 2006 Adapting radiotherapy to hypoxic tumours. *Physics in Medicine and Biology* **51**(19) 4903–4921.

Matsufuji N., Komori M., Sasaki H., Akiu K., Ogawa M., Fukumura A., Urakabe E., Inaniwa T., Nishio T., Kohno T. and Kanai T. 2005 Spatial fragment distribution from a therapeutic pencil-like carbon beam in water. *Physics in Medicine and Biology* **50**(14) 3393–3403.

Nihei K., Ogino T., Ishikura S., Kawashima M., Nishimura H., Arahira S. and Onozawa M. 2005 Phase II Feasibility Study of High-Dose Radiotherapy for Prostate Cancer Using Proton Boost Therapy: First Clinical Trial of Proton Beam Therapy for Prostate Cancer in Japan. *Japanese Journal of Clinical Oncology* **35**(12) 745 –752.

Nill S. 2002 Development and application of a multimodality inverse treatment planning system (in English). *Medical Physics* **29**(2) 258.

Nill S., Bortfeld T. and Oelfke U. 2004 Inverse planning of intensity modulated proton therapy. *Zeitschrift Für Medizinische Physik* **14**(1) 35–40.

Oelfke U. and Bortfeld T. 2001 Inverse planning for photon and proton beams. *Medical Dosimetry* **26**(2) 113–124.

Opfer G. 2001 *Numerische Mathematik für Anfänger.: Eine Einführung für Mathematiker, Ingenieure und Informatiker.* Vieweg.

Paganetti H. and Goitein M. 2001 Biophysical modelling of proton radiation effects based on amorphous track models. *International Journal of Radiation Biology* **77**(9) 911–928.

Paganetti H., Niemierko A., Ancukiewicz M., Gerweck L.E., Goitein M., Loeffler J.S. and Suit H.D. 2002 Relative biological effectiveness (RBE) values for proton beam therapy. *International Journal of Radiation Oncology*Biology*Physics* **53**(2) 407–421.

Petit S.F., Dekker A.L.A.J., Seigneuric R., Murrer L., van Riel N.A.W., Nordsmark M., Overgaard J., Lambin P. and Wouters B.G. 2009 Intra-voxel heterogeneity influences the dose prescription for dose-painting with radiotherapy: a modelling study. *Physics in Medicine and Biology* **54**(7) 2179–2196.

Pflugfelder D., Wilkens J.J. and Oelfke U. 2008 Worst case optimization: a method to account for uncertainties in the optimization of intensity modulated proton therapy. *Physics in Medicine and Biology* **53**(6) 1689–1700.

Rasch C., Steenbakkers R. and van Herk M. 2005 Target Definition in Prostate, Head, and Neck. *Seminars in Radiation Oncology* **15**(3) 136–145.

Rickhey M., Koelbl O., Eilles C. and Bogner L. 2008 A Biologically Adapted Dose-Escalation Approach, Demonstrated for 18F-FET-PET in Brain Tumors. *Strahlentherapie und Onkologie* **184**(10) 536–542.

Robertson J.B., Williams J.R., Schmidt R.A., Little J.B., Flynn D.F. and Suit H.D. 1975 Radiobiological studies of a high-energy modulated proton beam utilizing cultured mammalian cells. *Cancer* **35**(6) 1664–1677.

Roesink J.M., Moerland M.A., Battermann J.J., Hordijk G.J. and Terhaard C.H.J. 2001 Quantitative dose-volume response analysis of changes in parotid gland function after radiotheraphy in the head-and-neck region. *International Journal of Radiation Oncology*Biology*Physics* **51**(4) 938–946.

Rothkamm K. and Löbrich M. 2003 Evidence for a lack of DNA double-strand break repair in human cells exposed to very low x-ray doses. *Proceedings of the National Academy of Sciences of the United States of America* **100**(9) 5057–5062.

Sachs R.K., Hahnfeld P. and Brenner D.J. 1997 The link between low-LET dose-response relations and the underlying kinetics of damage production/repair/misrepair. *International Journal of Radiation Biology* **72**(4) 351–374.

Sato T., Kase Y., Watanabe R., Niita K. and Sihver L. 2009 Biological dose estimation for charged-particle therapy using an improved PHITS code coupled with a microdosimetric kinetic model. *Radiation Research* **171**(1) 107–117.

Schaffner B. and Pedroni E. 1998 The precision of proton range calculations in proton radiotherapy treatment planning: experimental verification of the relation between CT-HU and proton stopping power. *Physics in Medicine and Biology* **43**(6) 1579–1592.

Schardt D., Schall I., Geissel H., Irnich H., Kraft G., Magel A., Mohar M.F., Munzenberg G., Nickel F., Scheidenberger C., Schwab W. and Sihver L. 1996 Nuclear fragmentation of high-energy heavy-ion beams in water. *Advances in Space Research* **17**(2) 87–94.

Scholz M., Kellerer A.M., Kraft–Weyrather W. and Kraft G. 1997 Computation of cell survival in heavy ion beams for therapy. *Radiation and Environmental Biophysics* **36** 59–66.

Scholz M. and Kraft G. 1996 Track structure and the calculation of biological effect of heavy charged particles. *Advances in Space Research* **18**(1/2) 5–14.

Schultheiss T.E. 2008 The Radiation Dose-Response of the Human Spinal Cord. *International Journal of Radiation Oncology*Biology*Physics* **71**(5) 1455–1459.

Schulz-Ertner D., Nikoghosyan A., Thilmann C., Haberer T., Jäkel O., Karger C., Kraft G., Wannenmacher M. and Debus J. 2004 Results of carbon ion radiotherapy in 152 patients. *International Journal of Radiation Oncology*Biology*Physics* **58**(2) 631–640.

Semenenko V.A. and Stewart R.D. 2004 A Fast Monte Carlo Algorithm to Simulate the Spectrum of DNA Damages Formed by Ionizing Radiation. *Radiation Research* **161**(4) 451–457.

— 2006 Fast Monte Carlo simulation of DNA damage formed by electrons and light ions. *Physics in Medicine and Biology* **51**(7) 1693–1706.

Slater J.D., Yonemoto L.T., Mantik D.W., Bush D.A., Preston W., Grove R.I., Miller D.W. and Slater J.M. 2005 Proton radiation for treatment of cancer of the oropharynx: Early experience at Loma Linda University Medical Center using a concomitant boost technique. *International Journal of Radiation Oncology*Biology*Physics* **62**(2) 494–500.

Stuschke M. and Thames H.D. 1999 Fractionation sensitivities and dose-control relations of head and neck carcinomas: analysis of the randomized hyperfractionation trials. *Radiotherapy and Oncology* **51**(2) 113–121.

Thorwarth D., Eschmann S., Paulsen F. and Alber M. 2007 Hypoxia Dose Painting by Numbers: A Planning Study. *International Journal of Radiation Oncology*Biology*Physics* **68**(1) 291–300.

Thorwarth D., Eschmann S.M., Paulsen F. and Alber M. 2005 A kinetic model for dynamic [18F]-Fmiso PET data to analyse tumour hypoxia. *Physics in Medicine and Biology* **50**(10) 2209–2224.

Tobias C.A. 1985 The repair-misrepair model in radiobiology: comparison to other models. *Radiation Research. Supplement* **8** S77–95.

Unkelbach J., Chan T.C.Y. and Bortfeld T. 2007 Accounting for range uncertainties in the optimization of intensity modulated proton therapy. *Physics in Medicine and Biology* **52**(10) 2755–2773.

van der Kogel A.J. 1986 Radiation-induced damage in the central nervous system: an interpretation of target cell responses. *The British Journal of Cancer. Supplement* **7** 207–217.

van Herk M., Remeijer P., Rasch C. and Lebesque J.V. 2000 The probability of correct target dosage: dose-population histograms for deriving treatment margins in radiotherapy. *International Journal of Radiation Oncology*Biology*Physics* **47**(4) 1121–1135.

Weber U. and Kraft G. 1999 Design and Construction of a ripple filter for a smoothed depth dose distribution in conformal particle therapy. *Phys. Med. Biol.* **44** 2765–75.

Weyrather W.K., Ritter S., Scholz M. and Kraft G. 1999 RBE for carbon track-segment irradiation in cell lines of differing repair capacity. *International Journal of Radiation Biology* **75**(11) 1357–1364.

Wilkens J.J. 2004 *Evaluation of Radiobiological Effects in Intensity Modulated Proton Therapy: New Strategies for Inverse Treatment Planning*. Ph.D. thesis, University of Heidelberg.

Wilkens J.J. and Oelfke U. 2003 Analytical linear energy transfer calculations for proton therapy. *Medical Physics* **30**(5) 806–815.

— 2004 A phenomenological model for the relative biological effectiveness in therapeutic proton beams. *Physics in Medicine and Biology* **49**(13) 2811–2825.

— 2006 Fast multifield optimization of the biological effect in ion therapy. *Physics in Medicine and Biology* **51**(12) 3127–3140.

— 2008 Direct Comparison of Biologically Optimized Spread-out Bragg Peaks for Protons and Carbon Ions. *International Journal of Radiation Oncology*Biology*Physics* **70**(1) 262–266.

Wilson R.R. 1946 Radiological use of fast protons. *Radiology* **47** 487–491.

Withers H., Peters L. and Taylor J. 1995 Dose-response relationship for radiation therapy of subclinical disease. *International Journal of Radiation Oncology*Biology*Physics* **31**(2) 353–359.

Wouters B.G. and Brown J.M. 1997 Cells at intermediate oxygen levels can be more important than the "hypoxic fraction" in determining tumor response to fractionated radiotherapy. *Radiation Research* **147**(5) 541–550.

Zaider M. and Rossi H.H. 1980 The synergistic effects of different radiations. *Radiation Research* **83** 732–9.

List of Figures

List of Tables

Acknowledgements

I would like to express my gratitude to all those who supported me during the course of this thesis. Especially, I would like to thank Prof. Dr. Uwe Oelfke for providing an exceptional work environment and many new ideas, and also for encouraging me to pursue all the different aspects of this work.
Furthermore, I would like to thank Prof. Dr. Wolfgang Schlegel for accepting me into the Department of Medical Physics at the German Cancer Research Center (DKFZ) and providing all the necessary resources. I would also like to thank him for acting as a second referee of this thesis.
I am very grateful to David J. Carlson, Ph.D., not only for inviting me to spend four months at Yale University and providing financial support throughout that time but especially for giving me an additional perspective on radiation biology, providing a most friendly work environment, and many fruitful discussions. I am indebted to Robert D. Stewart, Ph.D., for many new insights into the microdosimetric considerations of radiation biology.
I would like to thank Paul J. Keall, Ph.D., for hosting me in an outstanding environment at the Stanford Cancer Center and his constant support and ideas during my stay. My stay at Stanford University in Palo Alto was generously funded by the German Academic Exchange Service (DAAD).
In addition I would like to thank all my various colleagues in particular Mark Bangert, Thomas König, Martin Fast, and Victor K. Yu for making work enjoyable. A special thanks goes to Dr. Simeon Nill for his help with *KonRad*.
I would also like to thank my parents and the rest of my family for providing me with everything I needed to pursue my thesis. And last but not least I would like to thank Dr. Hilka Eckardt for proofreading this thesis and constantly supporting me over the last years.

In accordance with the relevant regulations* parts of this thesis have already been published:

Frese M.C., Wilkens J.J., Huber P.E., Jensen A.D., Oelfke U. and Taheri-Kadkhoda Z.

*Promotionsordnung der Universität Heidelberg für die Naturwissenschaftlich-Mathematische Gesamtfakultät

2011a Application of Constant vs. Variable Relative Biological Effectivebess in Treatment Planning of Intensity–Modulated Proton Therapy. *International Journal of Radiation Oncology*Biology*Physics* **79**(1) 80–88

Frese M.C., Yu V.K., Stewart R.D., and Carlson D.J. 2011b A Mechanism Based Approach to Predict the Relative Biological Effectiveness (RBE) of Protons and Carbon Ions in Radiation Therapy. *Submitted to International Journal of Radiation Oncology*Biology*Physics*